IntechOpen

Electrical Resistivity and Conductivity

Edited by Adel El Shahat

ELECTRICAL RESISTIVITY AND CONDUCTIVITY

Edited by **Adel El Shahat**

Electrical Resistivity and Conductivity
http://dx.doi.org/10.5772/65130
Edited by Adel El Shahat

Contributors

Marios Sophocleous, Adel El-Shahat, Lucian Pîslaru-Dănescu, Laurentiu Constantin Lipan, Zhiquan Shu, Hsiu-Hung Chen, Xiaoming Zhou, Dayong Gao, Wei Shan, Zhaoguang Hu, Ying Guo, Chengcheng Zhang, Yao Liu, Héctor José Peinado-Guevara, Jaime Herrera Barrientos, Omar Delgado Rodríguez, Víctor Manuel Peinado Guevara, María Ladrón De Guevara Torres, Omar Llanes Cardenas

Notice

First published in Croatia, 2017 by INTECH d.o.o.
eBook (PDF) Published by IN TECH d.o.o.
Place and year of publication of eBook (PDF): Rijeka, 2019.
IntechOpen is the global imprint of IN TECH d.o.o.
Printed in Croatia

Legal deposit, Croatia: National and University Library in Zagreb

Additional hard and PDF copies can be obtained from orders@intechopen.com

Electrical Resistivity and Conductivity
Edited by Adel El Shahat

p. cm.

Print ISBN 978-953-51-3185-4

Online ISBN 978-953-51-3186-1

eBook (PDF) ISBN 978-953-51-4815-9

Meet the editor

Dr. Adel El-Shahat is an assistant professor at the Department of Electrical Engineering at Georgia Southern University, USA. He is the founder and director of Innovative Power Electronics and Nano-Grids Research Lab (IPENG). His research focuses on neural networks, smart grid systems, power electronics, electric machines, distributed generation, renewable energy systems, power systems, energy storage, optimization and FACTS. He got some awards and recognitions due to his work. He is an IEEE senior member and a member of many organizations (21 up to now). He is the editor-in-chief of *International Journal of Convergence Computing*, Inderscience Publishers, and a reviewer for more than 40 journals and conferences. He has 40 journal papers and 50 conference papers plus 6 books and 1 book chapter with 68 other publications.

Contents

Preface XI

Chapter 1 **Introductory Chapter: Recent Advances 1**
Adel El-Shahat

Chapter 2 **Electrical Resistivity Sensing Methods and Implications 5**
Marios Sophocleous

Chapter 3 **Resistivity Model of Frozen Soil and High-Density Resistivity Method for Exploration Discontinuous Permafrost 23**
Wei Shan, Zhaoguang Hu, Ying Guo, Chengcheng Zhang and Yao Liu

Chapter 4 **Measurement of the Electrical Resistivity for Unconventional Structures 53**
Lucian Pîslaru-Dănescu and Lipan Laurențiu Constantin

Chapter 5 **Estimation of Hydrological Parameters from Geoelectrical Measurements 83**
Héctor José Peinado Guevara, Jaime Herrera Barrientos, Omar Delgado Rodríguez, Víctor Manuel Peinado Guevara, Omar Llanes Cárdenas and María Ladrón De Guevara Torres

Chapter 6 **Assessment of Cryoprotectant Concentration by Electrical Conductivity Measurement and Its Applications in Cryopreservation 97**
Zhiquan Shu, Hsiu-Hung Chen, Xiaoming Zhou and Dayong Gao

Preface

This book addresses recent advances in electrical resistivity and conductivity modelling, measurement, estimation and sensing methods and implications. Electrical conductivity and electrical resistivity are very important properties for various materials. Water's purity, materials' sorting, chemical composition of substances, efficient metals' heat treatment examination, crystalline structures' stress state and heat damage prediction could be measured and estimated from the information of electrical conductivity. Electrical resistivity is the inverse of conductivity and acts as resistance of a material to the electrical current's stream through it, bringing about a change of electrical energy into different types of energy. The measure of resistance relies upon the kind of material. Materials with low resistivity are great transmitters of power, whereas materials with high resistivity are great separators. The number of atomic lattice structure's imperfection such as dislocations, vacancies, interstitial defects and impurity atoms causes temperature's increase and resistivity's increase as well. Motivated by the importance of electrical resistivity and conductivity, some important experts in this field grasp most recent researches in this book. The chapters are selected for this book to reflect current variable techniques, new concepts and methods related to the book's topic from different perspectives. This book introduces innovative case studies for "Electrical Resistivity Sensing Methods and Implications", "Resistivity Model of Frozen Soil and High-Density Resistivity Method for Exploration of Discontinuous Permafrost", Measurement of the Electrical Resistivity for Unconventional Structures", Estimation of Hydrological Parameters from Geoelectric Measurements" and Assessment of Cryoprotectant Concentration by Electrical Conductivity Measurement and Its Applications in Cryopreservation". These recent advances are well prepared and presented in the form of six chapters as the following:

Chapter (1): Introductory Chapter (Recent Advances)
Chapter (2): Electrical Resistivity Sensing Methods and Implications
Chapter (3): Resistivity Model of Frozen Soil and High-Density Resistivity Method for Exploration of Discontinuous Permafrost
Chapter (4): Measurement of the Electrical Resistivity for Unconventional Structures
Chapter (5): Estimation of Hydrological Parameters from Geoelectric Measurements
Chapter (6): Assessment of Cryoprotectant Concentration by Electrical Conductivity Measurement and Its Applications in Cryopreservation

Dr. Adel El-Shahat,
Senior IEEE Member
Assistant Professor, Department of Electrical Engineering
Founder and Director of Innovative Power Electronics and Nano-Grids Research Lab (IPENG)
Georgia Southern University, Statesboro, Georgia, USA

Chapter 1

Introductory Chapter: Recent Advances

Adel El-Shahat

Additional information is available at the end of the chapter

http://dx.doi.org/10.5772/intechopen.69046

This book proposes the most important researches in electrical resistivity and conductivity modeling, measurement, estimation and sensing methods, and implications. Electrical conductivity and electrical resistivity are very important properties for different materials. The goal of the book achieved via presenting new and modern case studies for sensing methods of electrical resistivity, resistivity modeling of frozen soil, measurement of the electrical resistivity for unconventional structures, estimation of hydrological parameters from geoelectric measurements, and assessment of cryoprotectant concentration by electrical conductivity measurement. It presents different methods to measure resistivity for both liquid and solid materials by explaining two, three, and four pole as well as toroidal resistivity cells. The special case of sheet material resistivity and resistance is explained in more detail, and equation for that special problem is simplified. It further provides information on common experimental errors, and a short guideline to improve the reliability and accuracy of the measurements. The way to experimentally determine the cell constant of a cell is described and the necessity for calibration is clearly explained too. Also, it provides information to overcome the standard problem of polarization, when the resistivity of solutions with high ionic content is investigated. After that, it explores the conduction characteristics of permafrost. A theoretical model and an experimental study to analyze the factors affecting the resistivity of permafrost are established and implemented. The study region was the permafrost degeneration area in the Northeast China. A permafrost profile map was drawn based on data from engineering drilling and an analysis of factors that influence permafrost resistivity. The reliability of the permafrost profile map was verified by an analysis of temperature data taken at measured points at different depths of the soil profile. Then, it introduces a device for measurement of the concrete structures' electrical volume resistivity. A quench protection active system (QPS) working in tandem with a superconducting coil structure (SCS), in order to prevent the damaging effects when the coil structures passing from the superconducting state in order to switch to normal-conduction state (quench), is presented as well. Moreover, it establishes experimental relationship between hydraulic transmissivity and hydraulic conductivity with Dar-Zarrouk parameter in porous media, transverse resistance (TR), in addition to a characterization of the water quality through the electrical resistivity. The determination

of hydraulic transmissivity and hydraulic conductivity is important for the development and management of groundwater exploitation of the study area. Finally, it illustrates an important application of the electrical conductivity measurement in cryopreservation. Cryopreservation is the way to cool the biological materials down to dormant state at low temperatures for long-term storage. This is done in order to reduce the cryo-injury to the cells during cryopreservation, cryoprotective agents (CPAs) should be added before freezing and removed after thawing prior to cell infusion due to the cytotoxicity of CPAs. The electrical conductivity measurement is used to assess the CPA concentration in cryopreservation. Measurement of electrical conductivity is validated as a safer and easier way to online and real-time monitoring of CPA concentration in cell suspensions, as well. Electrical resistivity and conductivity are proposed recently adopted different techniques and trends like: determining the magnitude of soil [1], in investigating frozen soil at Canada [2], in exploring frozen and petroleum polluted soils [3], in examining unfrozen water with ice substance with testing and algebraic equation implementation [4], in checking silty mud at various temperatures [5], in utilizing and examining the spatial appropriation of the island-shaped permafrost layer [6], in investigating the index of chemical weathering [7], in making initial experiments to make a relation in other different natural soil parameters using 79 samples of soil extracted from 10 boreholes [8], in illustrating and correlating clayey-soils' properties using 54 soil samples [9], and different techniques are adopted to estimate the content of water in soil with the aid of efficient electrical resistivity survey [10].

Finally, the rest of the book's chapters with their brief descriptions are shown in the following:

The second chapter, "Electrical Resistivity Sensing Methods and Implications," introduces basic operating principles of different methods to measure resistivity for both liquid and solid materials. It illustrates two, three, and four pole as well as toroidal resistivity cells. The van der Pauw technique is used as a step by step procedure to estimate the resistivity of a material with no arbitrary shape. The special case of sheet material resistivity and resistance is explained in more detail and equation for that special problem is simplified. It further provides information on common experimental errors and a short guideline to improve the reliability and accuracy of the measurements. The implications and challenges faced during resistivity measurements are explored and explained with ways to compensate for errors due to temperature and capacitance changes. In addition, the way to experimentally determine the cell constant of a cell is described and the necessity for calibration is clearly explained. It further provides information to overcome the standard problem of polarization when the resistivity of solutions with high ionic content is investigated.

The third chapter, "Resistivity Model of Frozen Soil and High-density Resistivity Method for Exploration," explores the conduction characteristics of permafrost. A theoretical model and an experimental study to analyze the factors affecting the resistivity of permafrost are established and implemented. The experimental study results are used to validate the rationality of the model of permafrost resistivity. To analyze differences in conductivity between underground media, a high-density resistivity (HDR) method is used, which infers the storage of underground geologic bodies with different resistivity based on the distribution of a conduction current under the electric field action. The study region was the permafrost degeneration area in the Northeast China. A permafrost profile map was drawn based on data from engineering drilling and an analysis of factors that influence permafrost resistivity. The

reliability of the permafrost profile map was verified by an analysis of temperature data taken at measured points at different depths of the soil profile.

The fourth chapter, "Measurement of the Electrical Resistivity for Unconventional Structures," presents an apparatus for measurement of the concrete structures' electrical volume resistivity to operate at 500 Hz, within range of 5–100 Ω m for probe/concrete sample's interface. Also, a quench protection active system (QPS) working in tandem with a superconducting coil structures (SCS), in order to prevent the damaging effects when the coil structures passing from the superconducting state in order to switch to normal conduction state (quench), is presented. This chapter proposes experimentation of yttrium barium copper oxide (YBCO) tape's SCS with high temperature superconductor (HTS) type at 92 K temperature value as well. Finally, it shows measurement of the electrical resistance of the sensing element (SE) as a part of the resistive type gas sensor.

The fifth chapter, "Estimation of Hydrological Parameters from Geoelectric Measurements," proposes to establish an empirical relationship between hydraulic transmissivity (T) and hydraulic conductivity (K) with Dar-Zarrouk parameter in porous media, transverse resistance (TR), in addition to a characterization of the water quality through the electrical resistivity. This parameter is estimated from surface resistivity measurements, which are more economical in relation to the pumping tests, thus T was characterized in the study area. The reasons behind that are: in the coastal aquifer of the lower part of the right bank of the river Sinaloa, there is a need for fresh water for agricultural development because around 15% of the water used in agricultural irrigation is from underground sources. This situation is exacerbated during periods of drought, which promotes drilling with the risk of finding brackish water in them, besides this, there is the risk of not meeting water demand due to low hydraulic transmissivity (T) of the aquifer, putting at risk the drilling costs implied. In this sense, the determination of T and K (hydraulic conductivity) is important for the development and management of groundwater exploitation of the study area. Generally, by means of pumping tests in wells T is obtained, with high costs, so there are few values of T. K is generally obtained by wells and laboratory test.

The sixth chapter, "Assessment of Cryoprotectant Concentration by Electrical Conductivity Measurement and its Applications in Cryopreservation," presents an important application of the electrical conductivity measurement in cryopreservation. Cryopreservation is the way to cool the biological materials down to dormant state at low temperatures (such as −80 or −196°C, the temperature of liquid nitrogen) for long-term storage and later thaw them back to the normal physiological temperatures before usage with recovered viability and functionalities of the cells and tissues. In order to reduce the cryo-injury to the cells during cryopreservation, cryoprotective agents (CPAs) should be added before freezing and removed after thawing prior to cell infusion due to the cytotoxicity of CPAs. In this chapter, the electrical conductivity measurement was applied to assess the CPA concentration in cryopreservation. The standard correlations between the CPA concentration and the electrical conductivity of the solutions (including CPA-NaCl-water ternary solutions and CPA-albumin-NaCl-water quaternary solutions) were experimentally obtained for a few mostly used CPAs, including dimethyl sulfoxide (DMSO or Me2SO), ethylene glycol (EG), and glycerol. Then, a novel "dilution-filtration" system with hollow fiber dialyzer was designed and applied to remove the CPA from the solutions effectively. Measurement of electrical conductivity was validated as a safer and easier way to online and real-time monitoring of CPA concentration in cell suspensions.

Author details

Adel El-Shahat

Address all correspondence to: aahmed@georgiasouthern.edu

Department of Electrical Engineering, Georgia Southern University, Georgia, USA

References

[1] Abu-Hassanein ZS, Benson CH, Blotz LR. Electrical resistivity of compacted clays. Journal of Geotechnical Engineering. 1996;**122** (5):397–406

[2] Angelopoulos M, Pollard WH, Couture N. Integrated geophysical approach for the detection and assessment of ground ice at Parsons Lake, Northwest Territories [MSc thesis]. Montreal, Quebec, Canada: McGill University; 2010.

[3] Delaney AJ, Peapples PR, Arcone SA. Electrical resistivity of frozen and petroleum-contaminated fine-grained soil. Cold Regions Science and Technology. 2001;**32**(2):107–119

[4] Fortier R, LeBlanc AM, Allard M, Buteau S, Calmels F. Internal structure and conditions of permafrost mounds at Umiujaq in Nunavik, Canada, inferred from field investigation and electrical resistivity tomography. Canadian Journal of Earth Science. 2008;**45**(3):367–387

[5] Hu ZG, Shan W (2011). Application of geological drilling combined with high-density resistance in island structure permafrost survey. The International conference on electronics, communications, and control, ICECC2011-proceedings: 1898–1904, IEEE Publisher.

[6] Li L. Study on the characteristics of the electrical resistivity of saline soils (Master's Thesis). Lanzhou, China: Lanzhou University; 2012.

[7] Son Y, Oh M, Lee S. Estimation of soil weathering degree using electrical resistivity. Environmental Earth Sciences. 2009;**59**:1319–1326

[8] Siddiqui FI, Osman SBABS. Simple and multiple regression models for relationship between electrical resistivity and various soil properties. Environmental Earth Sciences. 2013;**70**:259–267

[9] Das SK, Basudhar PK. Prediction of residual friction angle of clays using artificial neural network. Engineering Geology. 2008;**100**:142–145

[10] Ozcep F, Yildirim E, Tezel O, Asci M, Karabulut S. Correlation between electrical resistivity and soil-water content based artificial intelligent techniques. International Journal of Physical Science. 2010;**5**:47–56

Chapter 2

Electrical Resistivity Sensing Methods and Implications

Marios Sophocleous

Additional information is available at the end of the chapter

http://dx.doi.org/10.5772/67748

Abstract

This chapter discusses and explains the basic operating principles of various measuring methods of resistivity for materials in both liquid and solid phase. It provides explanations for two-, three-, and four-pole as well as toroidal resistivity cells. The van der Pauw technique is explored as a step-by-step procedure to estimate the resistivity of a material with no arbitrary shape. The special case of sheet material resistivity and resistance is explained in more detail, and equation for that special problem is simplified. It further provides information on common experimental errors and a short guideline to improve the reliability and accuracy of the measurements. The implications and challenges faced during resistivity measurements are explored and explained with ways to compensate for errors due to temperature and capacitance changes. In addition, the way to experimentally determine the cell constant of a cell is described and the necessity for calibration is clearly explained. It further provides information to overcome the standard problem of polarisation when the resistivity of solutions with high ionic content is investigated.

Keywords: resistivity sensors, resistivity measurement techniques, impedance, fringing, cell constant

1. Introduction

Electrical resistivity is defined as the ability of the material to resist the flow of electricity. Resistivity is calculated using Ohm's law when dealing with the material is homogeneous and isotropic. To provide a more accurate version of resistivity that can be applied for every material, the more general form of Ohm's law is used [1]:

$$E = \rho J \tag{1}$$

In this equation, E is a vector that represents the electric field generated in the material (V/m), J is also a vector that represents the current density within the material (A/m^{-2}), and ρ is a tensor which is basically the proportionality coefficient (Ωm).

Eq. (1) is Ohm's law in a more general context where E and J are vectors, and ρ is a tensor. This indicates that the current does not necessarily flow in the direction of the applied electric field. If it is assumed that the sample is homogeneous, meaning that it has the same properties everywhere, and that the material is isotropic, meaning that the material has the same properties in all directions, then ρ becomes a scalar. This is not always a valid assumption though.

In this chapter, isotropic and homogeneous materials are assumed, so ρ is considered to be a scalar. Considering the bar-shaped sample in **Figure 1**:

The electric field (E) generated in the material is calculated by dividing the potential difference (V) between the two sides, by the distance (l) over which the voltage is applied [1]:

$$E = \frac{V}{l} \tag{2}$$

The current density J is defined as the current I(A) flowing through the material, divided by the cross-sectional area A(m^2) through which the current flows [1]:

$$J = \frac{I}{A} \tag{3}$$

Area (A) in **Figure 1** is equal to the width w (m) times the height h (m). Combining the equations above, we get [1]:

$$V = \frac{I\rho l}{A} \tag{4}$$

If resistance is defined as:

$$R = \rho\frac{l}{A} \tag{5}$$

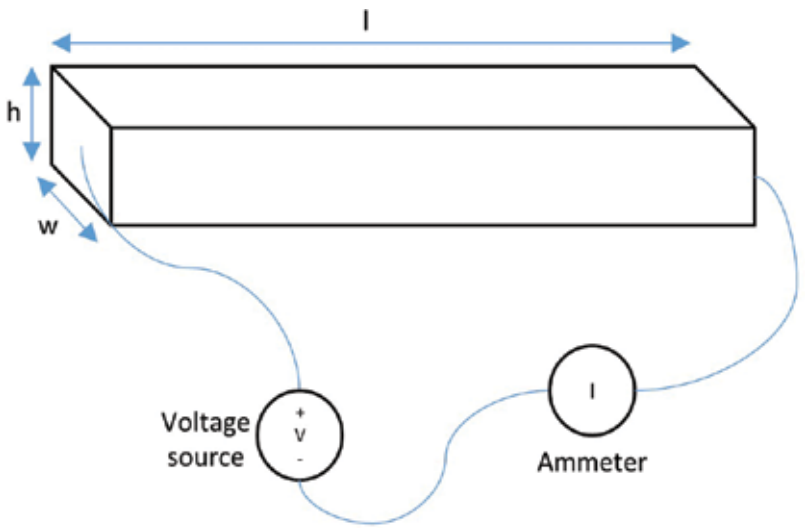

Figure 1. General two-point resistivity measuring technique [1].

Then, when Eqs. (4) and (5) are combined [1]:

$$V = IR \tag{6}$$

I is the current (A) flowing through the specific sample, V is the voltage (V) applied across this specific sample, and R is the resistance (Ω) of this specific sample.

Any changes in size and shape of the sample can cause changes in its total resistance, while those changes will not affect the resistivity of the sample since that is a property of the material alone. Conductivity (σ) is in principle the same property of the material, but it is calculated as the inverse of resistivity, and it is measured in Siemens per metre (S/m).

2. Resistivity measurement techniques

There are two main techniques to measure the resistivity of a material, either in liquid or in solid phase. The two techniques are the inductive and the contact-based methods.

2.1. Inductive or toroidal resistivity

The toroidal resistivity cell is based on the principle of inducing a current from one coil to another. The level of the induced current will be proportional to the resistivity of the medium inserted within the coils (**Figure 2**).

The main advantage of toroidal conductivity cell is that the coils do not come in contact with the solution. They are usually surrounded by a polymeric material. This allows the use of the cell in media where direct contact will damage the cell. While this is an advantage, toroidal cells lack sensitivity due to the absence of direct contact. Furthermore, toroidal cells are typically larger and the solution current induced by the toroid occupies a volume around the sensor. Hereafter, toroidal cells need more surrounding space and therefore are mounted in larger pipes [2].

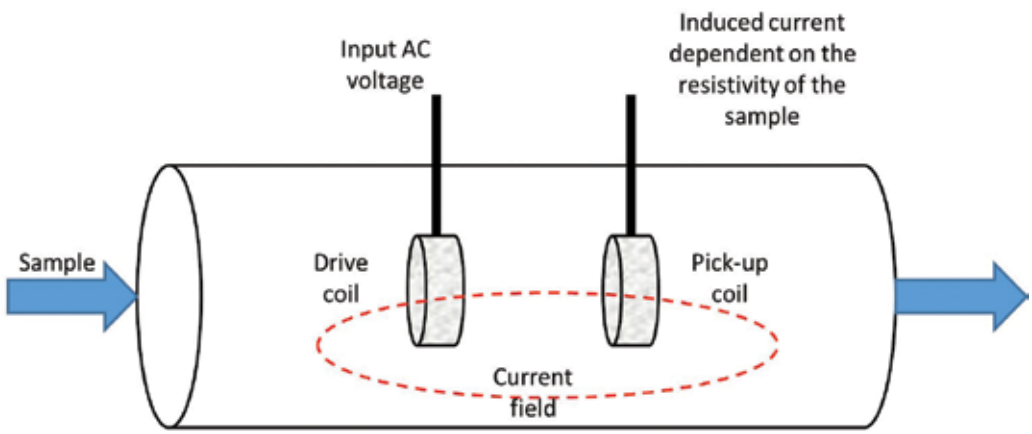

Figure 2. Toroidal resistivity cell [2].

2.2. Contacting resistivity

Contacting resistivity cells use two metals or graphite electrodes in contact with the sample, whether that is in liquid or solid phase. An AC current is applied to the electrodes by the electronic instrumentation, and the resulting AC voltage is recorded. This technique can measure down to pure water resistivity. The main downside of this cell type is that the cell is susceptible to coating and corrosion, which severely decreases the performance of the cell. In cases where the sample is a solution of high ionic content, polarisation effects will arise and result in non-linearity of measurements [2]. Further explanation on polarisation is provided later in this chapter.

2.2.1. Two-pole cells

In the standard two electrodes cell, an alternating current is applied between the two poles using a current source, while the resulting voltage is recorded (**Figure 3**).

Knowing the voltage and current across the two electrodes at low frequencies where the capacitance between the electrodes has no effect on the measurement, the resistance between the two electrodes can be calculated. Although the calculated resistance includes the resistance of the electrodes as well, in cases where the sample is a solution, its resistance is much higher than the resistance of the electrodes, and therefore, it can be neglected. Furthermore, in the attempt to measure the sample only, the impedance caused by polarisation of the electrodes and the field effects, interfere with the measurement, and both impedances are measured.

2.2.2. Three-pole cells

The three-pole cell is not as popular now as it has been replaced by the four-pole one. The purpose for adding the third pole was to direct and constrain the electric field lines. That minimises the effect of having special field fluctuations and eliminates the influences of external factors, such as the size of the beaker and the distance between the beaker walls and the poles, on the resistivity measurements. It provides more reproducible measurements when determining the cell constant and therefore more reproducible results.

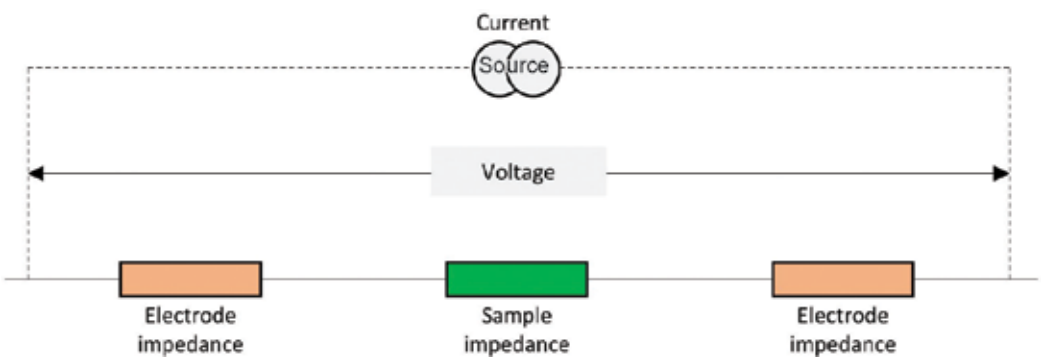

Figure 3. General electronic configuration of a two-pole resistivity cell [2].

2.2.3. Four-pole cells

In a four-pole cell (**Figure 4**), the current is applied to the outer electrodes in such a way that a constant potential difference is maintained between the inner electrodes. As this voltage measurement takes place with a negligible current, these two electrodes are not polarised, and therefore, their resistance is effectively zero. There are cases where the current applied to the outer electrodes is kept constant, and the voltage is measured between the two inner poles. In that case, the resistivity is directly proportional to the voltage measured. The four-pole method is usually used within an insulating tube. This technique minimises the beaker field effect because the electric field is constrained within the tube walls and because the volume of the material is well defined. Simultaneously, this eliminated the problem of the electric field being affected by the beaker walls. Therefore, the position of the cell in the beaker becomes irrelevant.

Ideally, electrodes placed at specific distances with a known effective surface area. The distances between the electrodes can define the cell constant based on the electric fields built up as shown in **Figure 5**:

The cell constant can be calculated using Poisson's equation:

$$\Delta V = \frac{I\rho}{2\pi}\left[\left(\frac{1}{r_1}-\frac{1}{r_2}\right)-\left(\frac{1}{r_3}-\frac{1}{r_4}\right)\right] \tag{7}$$

Some specific approaches are shown in **Figure 6** where d is the distance between the electrodes (m) and n is an integer to show that it is a multiple of d.

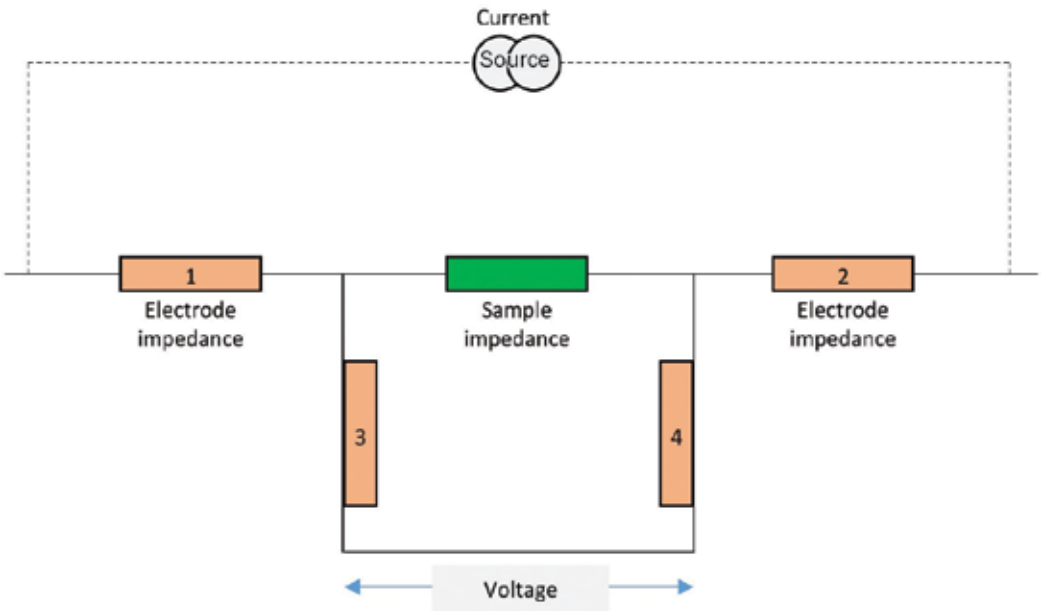

Figure 4. Four-pole resistivity cell [2].

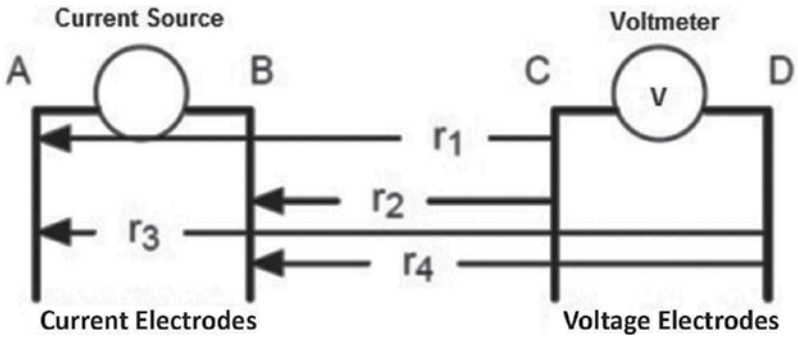

Figure 5. General electrode positioning for the four-pole resistivity cell [3].

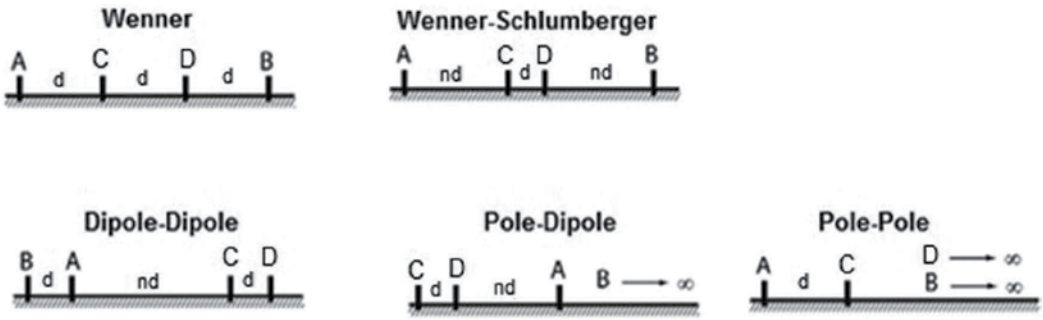

Figure 6. Typical electrode configurations for four-pole resistivity [3].

2.2.3.1. Sheet resistance measurements

There are cases where the resistance of sheets or films of various materials is of interest. In those cases, the sheet resistance is usually used to compare between different thin films of materials. The easiest way to measure sheet resistance is to make the material into a square film having equal length and width. Therefore, just like the bar sample in **Figure 1**, the resistivity can be calculated by [1]:

$$\rho \equiv \frac{Vwh}{Il} \tag{8}$$

where ρ is the sample resistivity (Wm), V is the voltage measured by the voltmeter (V), w is the width of the sample (m), h is the thickness of the sample (m), I is the current the ammeter measures flowing through the sample (A), and l is the length of the film (m).

When the width is equal to the length, then Eq. (8) becomes [1]:

$$\rho_{sq} \equiv \frac{Vh}{I} \tag{9}$$

The "sheet resistivity" is the resistivity of a square film of material and is represented by the symbol ρ_{sq}. The "sheet resistance" R_s is generally defined by [1]:

$$R_s \equiv R_{sq} = \frac{V}{I} \tag{10}$$

where V is the voltage measured by the voltmeter (V) and I is the current the ammeter measures flowing through the sample (A).

General units of sheet resistance are ohms (Ω), but in order to distinguish between resistance and sheet resistance, people most commonly use (Ω per square) or (Ω/square). In reality, sheet resistance is exactly the same as the resistance of a square film of a material. What makes sheet resistance interesting is that it is independent of the size of the square and the thickness of the sheet is not required to measure sheet resistance.

It is also a common technique to measure the resistance of films of arbitrary size and shape. This is usually done by pressing four collinear and equally spaced contacts into the film. The width and length of those contacts must be much greater than the distance between the contacts. In this case, sheet resistance can be calculated using [3]:

$$R_s = 4.532\frac{V}{I} \tag{11}$$

where V is the voltage measured across the two inner contacts (V), and I is the current applied through the two outer contacts (A).

It is understood that it will be very difficult to always fulfil these requirements for the contact size and distance between them. Under those circumstances, geometric correction factors are used to compensate in order to accurately measure the sheet resistance. These correction factors are available for the most commonly faced sample geometries [3].

2.2.3.2. Van der Pauw technique

Ideally, samples can have or can be made into convenient shapes to allow the use of the four-pole cell to measure their resistivity. There are also cases that the samples are of arbitrary shape and the sample might be damaged in the attempt to make it into the desired shape. Therefore, another technique called van der Pauw technique [1] is used. There are five conditions to be fulfilled in order to correctly use that technique:

1. Flat shape of uniform thickness.
2. No secluded holes.
3. Homogeneous and isotropic.
4. All four contacts must be located at the edges.
5. Contact area of any individual contact must be at least an order of magnitude smaller than the area of the entire sample.

When the samples are very small, the dimensional constrains for the van der Pauw method are not feasible, and therefore, some compensation is required.

The general step-by-step procedure for doing a van der Pauw measurement is as follows:

1. Define resistance $R_{ab,cd} = V_{cd}/I_{ab}$, where $V_{cd} = V_c - V_d$ and is the voltage between points c and d, while I_{ab} is the current flowing from contact a to contact b.
2. Measure the resistances of four points on the sample ($R_{21,34}$ and $R_{32,41}$). Define R_H as the higher of these two resistances and R_L as the lower of these two resistances.
3. Find ratio R_H/R_L and solve the function $f(R_H/R_L)$.
4. Calculate the resistivity ρ_x using:

$$\rho_x = \frac{\pi d(R_H + R_L)f(R_H/R_L)}{\ln 4} \tag{12}$$

   where ρ_x is the resistivity (Wm), d is the thickness of the sample (m), resistances R_H and R_L are measured in W, and ln 4 is approximately 1.3863.

   It is not necessary to measure the width or length of the sample.

5. Alter the contact points to measure $R_{43,12}$ and $R_{14,23}$. And then repeat steps 3 and 4 to calculate ρ_y using these new values for R_H and R_L. If the two resistivities ρ_x and ρ_y are not within 10% of each other, then either the contacts are bad or the sample is non-uniform. Try making using new contacts. If the two resistivities are within 10% of each other, the best estimate of the material resistivity ρ is the average:

$$\rho = \frac{(\rho_x + \rho_y)}{2} \tag{13}$$

   The function $f(R_H/R_L)$ is defined by the transcendental equation:

$$f(R_H/R_L) = \frac{-\ln 4(R_H/R_L)}{[1 + (R_H/R_L)\ln\{1 - 4^{-[(1+R_H/R_L)f]^{-1}}\}]} \tag{14}$$

2.2.4. Platinised cells

Platinised cells are most commonly used for measuring the resistivity of solutions. In solutions, the polarisation effect is of high importance due to the accumulation of ions near the surface of the electrodes. One way to minimise the polarisation effect is to decrease the current density. Current density can be decreased by increasing the electrochemical surface area of the electrodes. The most convenient and common way to do that is to cover the electrodes with platinum black. Platinised cells are very powerful because their cell constant

is linear over 2–3 decades of resistivity, while without platinum black it is only linear for approximately one decade. If platinum black is damaged or scratched, it will alter the cell constant and the properties of the cell. A minor shortcoming of platinised cells is that the cell constant tends to drift faster when compared with non-platinised cells. It is advisable to use platinum black for measurements in non-viscous samples, without suspensions and frequent calibrations.

2.2.5. Flow through cells

There are cases when the real-time resistivity of a small volume of flowing liquid is of interest. Flow through type resistivity cells are designed for those cases. These cells are customised for this kind of measurements but show several disadvantages. The most common problem with flow through cells is that they need a closed liquid system protected from air. In particular, for pure water resistivity measurements, it is very important to use a flow cell since contact with air will dissolve carbon dioxide and for carbonate ions changing the resistivity of the sample [4].

2.3. Cell-type comparisons and ranges

A short comparison between the classical two-pole resistivity cell and the more advanced four-pole resistivity cell is shown in **Table 1**:

Different conductivity cells have different properties, and the cell type must be chosen depending on the application. The measurement range over which the cell stays linear gets broader as the number of poles increases. Platinised poles also contribute to increasing the measurement span in which the cell is linear (**Figure 7**).

Advantages	Disadvantages
Two-pole cell	
1. Simple. **2.** Cheap. **3.** Good with viscous media or samples with suspension.	**1.** Field effects must be in the centre of the vessel. **2.** Only cells with no bridge between the plates. **3.** Polarisation issues in high conductivity samples. **4.** Calibration over a very small range.
Four-pole cell	
1. Linear over a wide conductivity range. **2.** Allows calibration and measurement in different ranges. **3.** Can be used for flow through or immersion type cells. **4.** Ideal for high conductivity medium can be used for low conductivity measurements if cell capacitance is compensated.	**1.** Unsuitable for micro-samples depth of immersion 3–4 cm.

Table 1. Comparison between two-pole and four-pole resistivity cells [2].

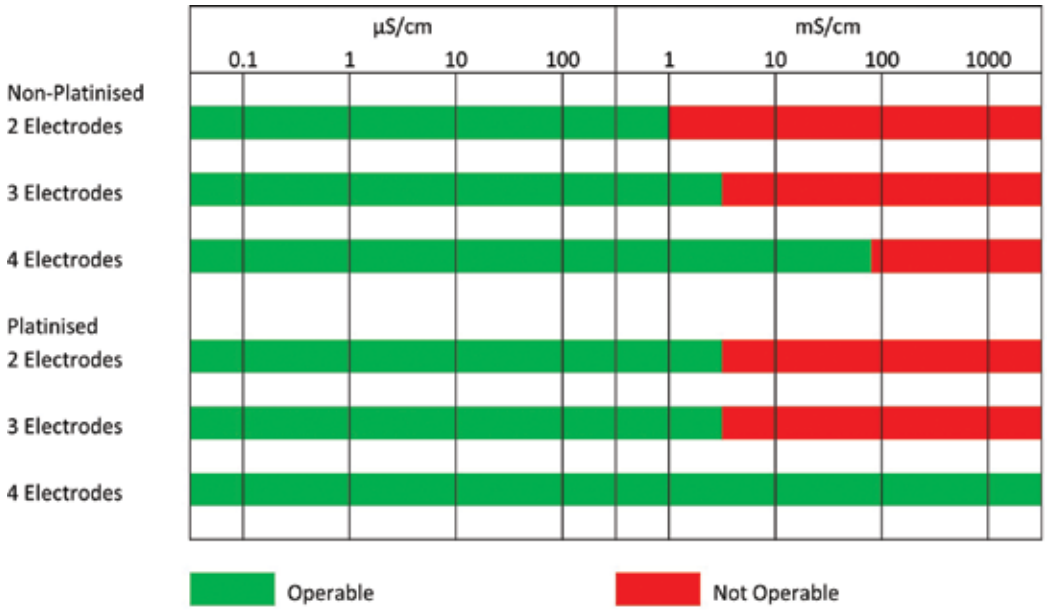

Figure 7. Operational ranges of several resistivity cell types [2].

3. Measurement implications

3.1. Calibration and cell constant calculation

Calibration of resistivity cells is important because it calculates the correct value of the cell constant in your working conditions. The cell constant is a factor that is used to convert the measured resistance to resistivity.

The cell constant is calculated by dividing the distance between the two poles by the cross-sectional area of the poles. Therefore, the cell constant is ideally, determined by the geometry of the cell. In reality, due to the fact that the cross-sectional area of the poles is not the actual electrochemical area (in case of liquids), the cell constant can only be measured experimentally using samples of known resistivities. In cases where the sample is a solution, cell constant can change due to changes on the electrodes. Those changes are caused due to contamination or due to physical-chemical alteration in case of platinised cells.

If high precision measurements are required, the cell constant needs to be calibrated often in samples of known resistivity at the same temperature as the actual measurements. Furthermore, when using the two-pole cells, the determination of the cell constant must be done at close resistivities to the resistivity of the sample since the cell constant is also resistivity dependent.

When using a two-pole cell, the choice of the cell constant value varies with the linear measurement range of the cell selected. Typically, a cell with $K = 0.1\ cm^{-1}$ is chosen for pure water measurements, while, for environmental water and industrial solutions, a cell with K of 0.4–1 cm^{-1} is used. Cells with up to $K = 10\ cm^{-1}$ are best for very low resistivity samples.

In the case of a four-pole cell, the cell constant value is generally included in the range from 0.5 to 1.5 cm^{-1} [5].

3.2. Polarisation

When attempting to measure the resistivities of solutions, more complications arise. Applying a potential difference or an electrical current to the electrodes of the cell, depending on the polarity, ions will be attracted or repelled from the electrodes. That ionic movement causes and accumulation of ions and therefore charge at the electrodes' surface which can further cause the initiation of chemical reactions (**Figure 8**). Subsequently, due to the accumulation of charge on the electrodes' surface, the actual resistance of the electrodes changes which is called polarisation. Polarisation can cause error on the measurements as it is a parasitic component to the solution resistance.

3.2.1. Preventing polarisation

There are several precautions that can be used to minimise or eliminate polarisation:

- Using an AC current will eliminate the polarisation effect since the polarity of the electrodes will constantly change, and the ions in the solution will not accumulate on one side since they will be sequentially repelled and attracted by the electrode.
- AC current frequency plays an important role on the polarisation effect. In solutions, low resistivities indicate high ionic content which means that the accumulation of ions will happen very quickly. In those cases, high frequencies are used, and for high resistivities where the ionic content is low, lower frequencies are used.
- It was explained earlier in Section 3.1 that the cross-sectional area of the cell when used in solutions is the electrochemical surface area and not the geometrical cross-sectional area.

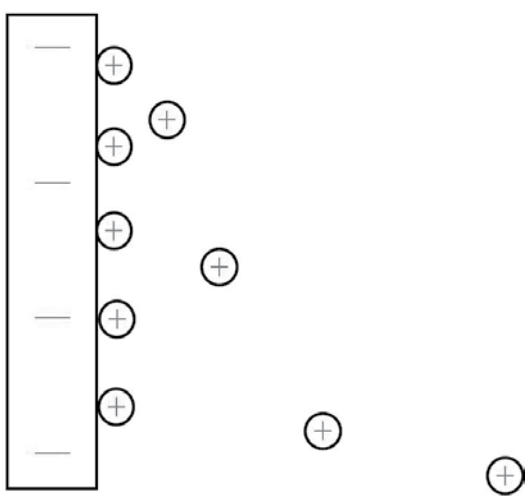

Figure 8. Polarisation effect due to ions contaminating the electrodes [1].

If that electrochemical surface area is increased, while the current is constant, it means that the current density on the electrode will decrease and subsequently the polarisation effect will also decrease. A common technique is to use platinum black to cover the electrodes' surfaces because it has a very high electrochemical surface area.

- Since the resistance of the electrodes has no effect on the measurements when using a four-pole cell, it means that polarisation will have no influence on the measurements of the four-pole cell.
- When using a two-pole cell, deposits on the electrode's surface can have a similar effect to polarisation since the electrodes' resistance changes, while in the case of the four-pole cells, contamination has no effect [6].

3.3. Geometry and frequency

Different geometries can affect error levels. The most common errors in resistivity measurements are those produced by field effects. A theoretical assumption has been made when designing resistivity cells that the electric field lines are straight lines from one pole to the other and that they are not affected by surrounding objects. In reality, although the majority of the field lines do form in straight lines, some of them form curves (**Figure 9**). These field lines can affect the measurement especially when another object or another field interferes with them.

Three and four-pole conductivity cells are designed to minimise this effect. There is still some field effect present for the four electrodes cell due to the fact that when field lines do not flow directly to the other electrode, the distance travelled by the current is different from the distance between the two electrodes. That can have a major effect on the cell constant.

In most conductivity metres, the frequency is automatically increased with decreasing resistance of the sample, to avoid polarisation errors at low resistivities [5].

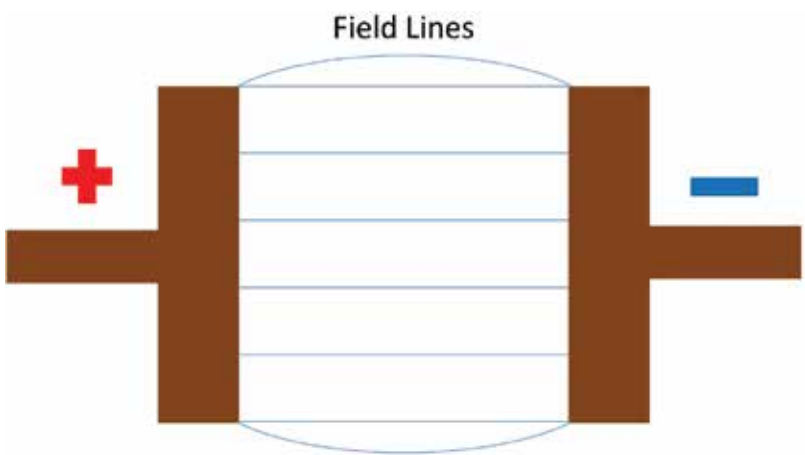

Figure 9. Field lines between the two electrodes [2].

http://dx.doi.org/10.5772/67748

3.4. Cable resistance and capacitance

Cables are made of conductors, meaning that the material has very low resistivities. The total resistance of a cable is proportional to its length. The resistance of the cable can induce an error on the readings of the cell, and therefore, it should be compensated for accurate measurements. The cable resistance becomes significant when the resistance of the sample is lower than (approximately 50 Ω) and when using the two- or three-pole techniques.

For four-pole cells, the cable resistance has no influence. A shielded cable of a given length has a given capacity. When the measured resistance is high, the cable capacitance is not negligible and must be taken into account.

Compensate the cable capacitance when:

- using a four-pole cell,
- measuring high resistivities,
- the cable capacitance of the resistivity cell is >350 pF.

3.5. Temperature effect

Resistivity measurements are temperature dependent; if the temperature increases, resistivity decreases. The concept of reference temperature was introduced to allow the comparison of resistivity results obtained at different temperature. The reference temperature is usually 20 or 25°C. Generally, resistivity metres measure the resistance of the cell and calculate the resistivity by knowing their cell constant. They also measure the temperature of the resistivity measurement, and they use a function to translate the measured resistivity to reference resistivity. Reference resistivity is the resistivity of the sample at a reference temperature. Therefore, resistivity measurements are often associated with temperature sensors for temperature correction to improve resistivity calculations.

There are three common temperature correction methods:

- Linear function
- Non-linear function for natural waters according to ISO/DIN7888
- No correction

When the measurement requires very high precision and accuracy, the measurements are taken in a temperature controlled environment to ensure temperature stability and for a more accurate determination of the cell constant at that temperature [3].

3.5.1. Linear temperature correction

When measuring resistivity of solutions with medium to low resistivity, the linear temperature correction is used. Linear temperature correction is used, for example, for saline solutions, acids, and leaching solutions. The conductivity of the solution can be calculated by [7]:

$$\kappa_{T_{ref}} = \frac{100}{100 + \theta(T - T_{ref})}\kappa_T \tag{15}$$

where $\kappa_{T_{ref}}$ is the conductivity at reference temperature, κ_T is the conductivity at the temperature of the measurement, T_{ref} is the reference temperature, T is the sample temperature, and θ is the temperature coefficient (%/°C). If resistivity is required, then the inverse of the calculated conductivity is the resistivity.

The linear correction method is useful and correct only when the reference temperature and the temperature of the measurement are close. The risk of error for this method is directly proportional to the difference between the reference temperature and the temperature of the measurement.

In order to calculate the temperature coefficient, the resistivity of a sample at temperature T_1 close to T_{ref} and another temperature T_2 is measured. Then, the temperature coefficient is calculated by using the following equation [7]:

$$\theta = \frac{(\kappa_{T2} - \kappa_{T1})100}{(T_2 - T_1)\kappa_{T1}} \tag{16}$$

T_2 must be a typical sample temperature, usually room temperature, and should be approximately 10°C different from T_1. Indicative ranges for the temperature coefficients of commonly used electrolytes are provided below [2]:

Acids: 1.0–1.6%/°C

Bases: 1.8–2.2%/°C

Salts: 2.2–3.0%/°C

Drinking water: 2.0%/°C

Ultrapure water: 5.2%/°C

3.5.2. Non-linear temperature correction

In frequent cases of natural waters, for example, ground water, surface water, drinking water, and waste water, the classical linear temperature correction function is not suitable. The reason is that the temperature dependency of the conductivity for these solutions in nonlinear and can only be defined by a 4th degree polynomial. The basic idea for this correction method is to correct the measured conductivity from the measurement temperature to 25°C to give K_{25} [7].

$$K_{25} = f_{25}(T)K_T \tag{17}$$

$f_{25}(T)$ is the temperature correction factor used for the conversion of conductivity values of natural water from T to 25°C. This function is a 4th degree polynomial equation,

is provided by ISO/DIN7888 standard, and is valid for measurements between 0 and 35.9°C [7].

4. Improving measurement reliability

In order to improve the reliability and accuracy of the measurements, the source of errors must be identified. Several common experimental errors are listed below, and a guide to overcome some of the common challenges of resistivity measurements is provided in detail.

4.1. Common experimental errors

There are many experimental dangers to avoid when making resistivity measurements. The most common sources of error arise from doing a two-point measurement on a material that has any of the contact problems discussed earlier. Therefore, it is logical to do four-point measurements whenever possible. This section describes experimental practises to avoid errors in measuring resistivity [1, 7]:

1. The biggest challenge for measuring resistivity is to obtain and maintain good electrical connections between the electrodes and the sample. There are several ways to improve the electrical contacts ranging from just wiping the sample with a suitable solvent to soldering directly on the sample or even pressing some pieces of soft metals onto the contact area. Scraping the sample's surface with a razor blade, exposing a fresh surface, and using alligator clips or silver-painting are also appropriate options. It has to be noted that even good contacts can become bad from aging. Therefore, maintaining good contacts is also very important.

2. The resistivity cell should be calibrated before measuring any material samples. Calibration procedures have been described earlier in this chapter.

3. The input impedance of the voltmeter should at least two orders of magnitude higher than the impedance of the resistivity cell. The input impedance is usually listed in the equipment specifications. Usually, customised instrumentation amplifiers are used with very high input impedance of the order of $10^{15}\Omega$ to avoid these problems.

4. The resistivity cell should be tested before measuring any material samples. It is advisable to test the resistivity cell using materials of known resistivities and validate the results from the system before taking any measurements.

5. In general, the geometry of the cell is vital. Therefore, especially in the case of the four-pole cell, the area of the voltage electrodes should be made as small as possible and also the distance between the two voltage electrodes should always be much bigger than the thickness of the sample. That will decrease the error between the geometrical cell constant and the actual cell constant by providing a better estimate of the effective volume of the sample.

6. An obvious but not trivial point is to ensure the circuit integrity. The most usual cause of meaningless results is when the circuit's integrity is violated. For correct measurements, in any kind of cell, the electrodes must be completely independent of each other and the only thing connecting them must be the sample under investigation. Even in the four-pole cells, all the electrodes should be checked for short circuits before using them for measurements. Any remarkably low resistance value measured between the electrodes should indicate short circuit.

7. The applied voltage or current can cause self-heating of the material or even the cell itself, which can change the resistivity measurements. To avoid this problem, use as low current as possible while the voltage is still readable on the metre or use a temperature sensor on the resistivity cell itself.

8. Depending on the material of the sample, Ohm's law is not always obeyed. There are non-Ohmic materials that change their resistance depending on the applied voltage or current across them. Therefore, before making accurate measurements, the linearity between voltage and current across the sample should be investigated. It is advised to apply voltages or current both above and below the measuring values and to ensure that resistivity measurements will be made within the linear region of the voltage current graph.

9. It is good practise to always test the equipment before performing any measurements. Sometimes, voltmeter leads age and their contacts with the voltmeter are damaged. In those cases, the voltmeter gives random values since it operates as an open circuit. The best way to check for open circuits on the voltmeter is to drop the current input to zero and check if the voltage also drops to zero. If it does not fall to zero and gives a random number, then that indicates open circuit.

10. A further check of the equipment is to reverse the leads on the voltmeter and measure the resistance again. The two readings are within 10% of each other; then, the readings are considered as valid. It has to be noted and understood that in this case the current is flowing between the two inner electrodes (in the case of four-pole cell) and that the voltage is measured between the two outer electrodes.

11. The resistivity of some materials can light dependent. This is particularly a problem with semiconductors. If there is a chance of this, try blocking all light from the sample during measurement.

4.2. Guidelines for improved resistivity measurements

Other than the common experimental errors and some ways to prevent them, further measurement improvements, can be achieved when following these simple rules [2, 6, 7]:

4.2.1. Frequent cell constant calibration

The cell constant is the most important component for accurate resistivity measurements. Although when measuring resistivities of solids, the cell constant is fairly stable, when

measuring resistivities of liquids, it can be vital. It is ideal to determine the cell constant of the cell right before any measurement, but a frequent cell constant calibration is advisable. In particular, in the case of platinised cells, calibration should be performed even more frequently due to the elevated risk of contamination and physical or chemical alteration of the platinum layer.

4.2.2. Controlling the temperature and maintaining homogeneity

For high accuracy and low resistivity measurements, it is required to have a stable temperature of the sample and the cell itself. If the measurements will be thermostated, then the calibration should be made at the same temperature as the measurements. Furthermore, homogeneity of the sample is critical. All of the equations used for the calculation of resistivity assume homogeneity. In particular, for solution, it is highly advised to stir the solution continuously during both the calibration and the measurement. For resistivity measurements, the resistivity reading can be expressed either at the measuring temperature or at a reference temperature using the pre-mentioned temperature correction factors.

4.2.3. Cell positioning

Some cell types can be greatly affected by the surrounding materials. In solutions, for example, the distance between the cell and the wall can be a major source of error since the electric field is bounded and altered by the beaker walls. Two-pole cells should always be placed at the centre of the beaker, and all electrodes, no matter what the cell type is, must be completely immersed in the sample.

4.2.4. High resistivity measurements

- Use flow-through cell to avoid carbon dioxide from dissolving in the solution.
- Use low cell constant, 1 cm^{-1} or lower.
- Do not use platinised cells because they are easier to clean and have a faster response.
- Ensure that the instrumentation is within its operating ranges in terms of current, voltage, and frequency.

4.2.5. Low resistivity measurements

- Avoid polarisation by using platinised and four-pole cells.
- High cell constant (1 cm^{-1}) or higher if possible.
- Resistivity is not proportional to concentration at high levels. Do not attempt to dilute the solutions to bring them down to the measuring range of the cell.
- Ensure that the instrumentation is within its operating ranges in terms of current, voltage, and frequency.

Author details

Marios Sophocleous

Address all correspondence to: sophocleous.marios@ucy.ac.cy

Holistic Electronics Research Lab, Department of Electrical & Computer Engineering, University of Cyprus, Nicosia, Cyprus

References

[1] Webster, JG., editor. Electrical Measurement, Signal Processing and Displays. Florida, USA: CRC Press LLC; 2004. 723 p.

[2] Sophocleous, M. Thick Film Underground Sensors [thesis]. Southampton, U.K.: University of Southampton; 2016. 309 p.

[3] Nabighian, M., editor. Electromagnetic Methods Vol. 1: Theory. 2nd ed. Oklahoma: Society of Exploration Geophysicists; 1988.

[4] Plambeck, J., editor. Electroanalytical Chemistry: Basic Principles and Applications. United States of America: John Wiley & Sons; 1982.

[5] Pletcher, D., editor. A First Course in Electrode Processes. 2nd ed. Cambridge: The Royal Society of Chemistry; 2009.

[6] Scholz, F., editor. Electroanalytical Methods: Guide to Experiments and Applications. 2nd ed. Berlin: Springer; 2010.

[7] Radiometer Analytical SAS, Conductivity: Theory and Practice, France, 2004-05B.

Chapter 3

Resistivity Model of Frozen Soil and High-Density Resistivity Method for Exploration Discontinuous Permafrost

Wei Shan, Zhaoguang Hu, Ying Guo,
Chengcheng Zhang and Yao Liu

Additional information is available at the end of the chapter

http://dx.doi.org/10.5772/intechopen.68197

Abstract

In permafrost-degraded areas, "islands" of permafrost can be buried in the unfrozen soil. When permafrost is arranged in this discontinuous pattern, it is more difficult to analyze from an engineering or geological perspective. The degree of resistivity of unfrozen soil is determined by the dry density, temperature, moisture content, and pore water resistivity of the soil, as well as by the mineral composition, size, and cementing state of the soil particles. Part of the water in the soil pores experiences a phase change as the soil freezes, so permafrost has different resistivity than unfrozen soil. In this chapter, we explore the conduction characteristics of permafrost. First, we established a theoretical model to analyze the factors affecting the resistivity of permafrost. Next, we used an experimental study to analyze how unfrozen water content, initial moisture content, soil temperature, and dry density influence the resistivity of frozen soil. These experimental study results served to validate the rationality of the model of permafrost resistivity. To analyze differences in conductivity between underground media, we used a high-density resistivity (HDR) method, which infers the storage of underground geologic bodies with different resistivity based on the distribution of a conduction current under the electric field action. In this chapter, the WGMD-9 super HDR measurement system produced by the Chongqing Benteng Numerical Control Technique Research Institute was used to obtain the resistivity profile. The study region was the road area from Bei'an Expressway to Heihe Expressway in the permafrost degeneration area in Northeast China. A permafrost profile map was drawn based on data from engineering drilling and an analysis of factors that influence permafrost resistivity. The reliability of the permafrost profile map was verified by an analysis of temperature data taken at measured points at different depths of the soil profile.

Keywords: electrical resistivity, electrical resistivity model, high-density resistivity method, frozen soil

1. Introduction

One of the innate attributes of a soil is the electrical resistivity. The dry density, water content, temperature, mineral composition, and structure of the soil determine the magnitude of the electrical resistivity. In a previous experimental study, the cementation factor was shown to be related to the shapes and cementation conditions of soil particles. A study by Wu et al. [1] preliminarily showed the factors that affected variation in the electrical resistivity of soils. The results showed that the electrical resistivity of the soil varied with soil type, mother rocks, soil texture, and soil salt content. Water content, the water-cement ratio, and the degree of saturation are well correlated with the electrical resistivity of a cement-soil mixture. Li et al. [2] assessed the relationship between the electrical resistivity of a saline soil and the salt content, water content, porosity, and degree of saturation. The results showed that the electrical resistivity of the saline soil decreased with increases in the water content, salt content, and the degree of saturation. Also, it increased with increasing porosity. Zha et al. [3] studied the effect of the particle composition of a soil on its electrical resistivity and showed that the electrical resistivity of the soil decreased with increases in the liquid limit or the plastic limit of the soil.

A calorimetric experiment on an undisturbed frozen soil sample was performed by Fortier et al. [4], and they also obtained the unfrozen water and ice contents in the sample. Fortier et al. [5] determined the electrical resistivity at the location near the sampling site and determined the relation between the electrical resistivity and the unfrozen water and ice contents using a linear regression analysis. A study of the electrical resistivity of frozen and petroleum-polluted soils was reported by Delaney et al. [6]. They found that the freezing conditions and petroleum pollution could both result in an increase in the electrical resistivity of the soil. Fu et al. [7] performed a study in which they monitored the electrical resistivity of silty clay obtained from the Beiluhe River on the Qinghai-Tibet Plateau during an entire uniaxial compression test that was carried out at different temperatures. They showed that the uniaxial compression strength of the frozen soil had a strong semi-logarithmic relationship with the initial electrical resistivity. The relationship between the electrical resistivity and the ice content of the frozen soil was obtained by Angelopoulos et al. [8] using the electrical resistivity method on the frozen soil from Parsons Lake in the Northwest Territories of Canada. The electrical resistivity method was also used to study the spatial distribution of the island-shaped permafrost layer along the Beian-Heihe highway. Discontinuities in the electrical resistivity at the upper and lower interfaces of the island-shaped permafrost layer were observed and permafrost layer showed significantly high resistance. Variation in the electrical resistivity of the areas without permafrost was relatively gentle with no discontinuities.

This study investigated the relationship between the electrical resistivity of a soil body and the water content, temperature, and dry density of the soil to thoroughly study the electrical conductive properties of frozen soils. We used mathematical deduction and a theoretical model for the electrical resistivity of frozen soils. Experiments were conducted on soil bodies with different water contents and dry densities at different temperatures. We also verified the reasonableness of the theoretical model for the electrical resistivity of frozen soils and provided a theoretical basis for exploring the distribution of underground shallow frozen soils with the electrical resistivity method.

In recent decades, geophysical analysis has become a common tool in studies that evaluate stratigraphic distribution. In situ geophysical techniques can directly or indirectly measure the physical parameters of rock and soil that are related to the lithological, hydrological, and geotechnical features of rocks and soils [9–11]. Compared with other ground detection technologies such as drilling, clinometry, and laboratory testing, these physical detection techniques are nondestructive and can integrate the information acquired over large soil volumes to overcome the point-scale limitations of standard geotechnical measurements. The high-density resistivity (HDR) method, an in situ geophysical technique, is increasingly being applied to geological surveys of landslides, permafrost, and so on [9, 12, 13].

By measuring the resistivity of subterranean rock and soil, the HDR method can provide relevant two-dimensional (2D) and three-dimensional (3D) images, which are used in geophysical exploration to gain solutions to shallow geologic problems [14–18]. The HDR method has already been applied in the arctic and alpine environments to identify the sliding surface of landslide and to detect the distribution of permafrost [17, 19–24]. As an effective detection method for permafrost exploration, the HDR method can determine the thickness and the upper and lower limits of permafrost, metrics that have been used in permafrost surveys since the late 1970s [10, 25–28]. However, all geophysical methods have their applicability, including regional limitations and reliability. The HDR method has not been effectively and extensively applied in analyses of permafrost in the high latitudes of Northeast China nor has geophysical exploration been applied in the permafrost areas in Lesser Khingan Mountains, China, to monitor the degradation process of permafrost.

In this chapter, the HDR measurement system was used to obtain the resistivity profile. The study region was the road area from Bei'an Expressway to Heihe Expressway in the permafrost degeneration area in Northeast China [29]. A permafrost profile map was drawn based on data from engineering drilling and an analysis of factors that influence permafrost resistivity. The reliability of the permafrost profile map was verified by an analysis of temperature data taken at measured points at different depths of the soil profile.

2. Establishing a model for the electrical resistivity of frozen soils

2.1. Models for the electrical resistivity of soils

An electrical resistivity model that is applicable to saturated non-cohesive soils and pure sandstones, assuming that the conductivity of solid particles is not considered, has been proposed [30]:

$$\rho = a\,\rho_w\, n^{-m} \tag{1}$$

where ρ is the electrical resistivity, ρ_w is the electrical resistivity of pore water, n is the porosity, a is an experimental parameter, and m is the cementation factor.

Archie [30] proposed an electrical resistivity model that related the electrical resistivity of a soil to the structure of the soil. It expanded the approaches for studying the microstructures of soils. This proposed model, however, only considered the effect of the electrical resistivity and

porosity of the pore water on the electrical resistivity of the soil. This means that the potential applications of the electrical resistivity proposed model are limited.

In later work, the electrical resistivity model proposed by Archie [30] was expanded to the following:

$$\rho = a\,\rho_w\,n^{-m}\,s_r^{\ -p} \tag{2}$$

where s_r is the degree of saturation and p is the saturation exponent.

In the expanded electrical resistivity model, the degree of saturation of the pore water is considered. The expanded model is therefore applicable to non-saturated pure sandstones and non-cohesive sand. The expanded model, however, ignores the effects of other factors on the electrical resistivity of a soil.

On the basis of experimental studies and considering the effect of the electrical double layers on the surfaces of soil particles on the electrical resistivity of the entire soil body, an electrical resistivity model that is applicable to non-saturated cohesive soils was proposed:

$$\rho = \frac{a\,\rho_w\,n^{-m}\,s_r^{\ 1-p}}{s_r + \rho_w BQ} \tag{3}$$

where B represents the electrical resistivity of the charge whose electrical property is opposite to that of the surface of the soil particle in the electrical double layer, Q is the cation exchange capacity per unit soil pore, and BQ is the electrical resistivity of the electrical double layer on the surface of the soil particle.

Wasman and Smits [31] proposed an electrical resistivity model that considered the effect of the electrical conductivity of soil particles on the electrical resistivity of the soil, which means that the electrical resistivity model proposed by Smits is applicable to non-saturated cohesive soils.

Beside pore water and soil particles, there is a third conductive propagation path for cohesive soils, that is, the series-coupled soil-water propagation path. Considering the previously mentioned three conductive propagation paths for cohesive soils, the following equation for the model for the electrical resistivity of non-saturated cohesive soils has been deduced:

$$\rho = \left[n\,s_r - F' \frac{\theta'}{1+\theta'} BQ + \frac{n\,s_r - F' \frac{\theta'}{1+\theta'}}{\rho_w} + \frac{F'(1+\theta')BQ}{1+BQ\,\rho_w\,\theta'} \right]^{-1} \tag{4}$$

where F' is the conductive structure coefficient (the ratio of the width of the series-coupled soil-water path to the side length of the entire soil body) and θ' is the volumetric water content of the parallel-coupled soil-water part.

Zha et al. [32] proposed an electrical resistivity model that considered the effect of conductive paths and organically combined the electrical resistivity of a soil with factors such as porosity, degree of saturation, electrical resistivity of the pore water, soil structure, soil particle composition, and electrical double layers on the surfaces of soil particles. This thereby rendered the model for non-saturated cohesive soils more reasonable.

Equations describing the relation between electrical resistivity of a soil sample and the unfrozen water content as well as that between electrical resistivity of a soil sample and the ice content are the following [4, 5]:

$$\frac{\rho}{\rho_{uw_0}} = e^{-w_{uw}/w_{uw_0}} \tag{5}$$

$$\frac{\rho}{\rho_{i_0}} = \left(\frac{w_i}{w_{i_0}}\right)^a \tag{6}$$

where ρ is the electrical resistivity (Ωm), ρ is the unfrozen water content (%), w_i is the ice content (%), ρ_{uw_0} = 12,820 Ωm is the reference electrical resistivity for a reference unfrozen water content w_{uw_0} of 5%, ρ_{i_0} = 1316 Ωm is the reference electrical resistivity for a reference ice content w_{i_0} of 10%, and a = 1.73 is the exponent of the power law between the electrical resistivity and the ice content.

Fortier et al. [5] proposed a model for electrical resistivity that first considers the effect of the ice content of a soil. This model is therefore applicable not only to unfrozen soils but also to frozen soils. A frozen soil, however, is a complex multiphase body. Also, there are many factors that affect a frozen soil. This model proposed by Fortier et al. [5] only considers the effect of the ice content of a soil on the electrical resistivity of the soil. In addition, the preset reference electrical resistivity value has no generality.

Angelopoulos et al. [8] analyzed frozen soil from Parsons Lake in the Northwest Territories of Canada with the electrical resistivity method and the study results showed the relationship between the electrical resistivity of the frozen soil and the ice content. In the study, the electrical resistivity method was applied in frozen soil exploration and proved to be very useful. However, the results were quite discrete and poorly correlated. Also, the electrical resistivity method only considers the effect of the ice content on the electrical resistivity of the frozen soil and is therefore limited.

2.2. Establishing a model for the electrical resistivity of frozen soils

A fraction of the pore water of a soil goes through a phase change during the freezing process. The electrical resistivity characteristics of a frozen soil are therefore different from those of an unfrozen soil. In our study, we assumed that there are three conductive paths (soil particles, ice-water mixtures, and soil-ice-water mixtures, i.e., the gas propagation path is ignored) for a frozen soil, as was also assumed in the three-element electrical conduction model and the model for the electrical resistivity of unsaturated cohesive soils. We deduced the equation for the model for the electrical resistivity of frozen soils [33]:

$$\rho = \left[A \times \frac{a\,\theta^{-b}}{w} + \rho_d\left(B \times \frac{a\,\theta^{-b}}{w} + C\right) + D\right]^{-1} \tag{7}$$

where A–D represent coefficients that are related to the structural characteristics of the frozen soil and electrical resistivity of each component of the frozen soil, w is the water content of the frozen soil, $a\,\theta^{-b}$ is the unfrozen water content of the frozen soil, θ is the absolute value of the temperature of the frozen soil, and ρ_d is the dry density of the frozen soil.

2.3. Main factors influencing the electrical resistivity of a frozen soil

Four primary factors can affect the electrical resistivity of a frozen soil:

1. Soil type. Particle size, shape, and mineral composition show large differences between the solid particles of different soil types. The mineral composition plays an important role in

the conductive path of soil particles. This results in differences in the electrical resistivity for different soil types.

2. Structural characteristics of the soil. The structural characteristics of the ice-water mixture and the shapes and orientations of soil particles are factors that determine the structural characteristics of the soil.

3. Pore water affects the electrical resistivity of a frozen soil based on the water content and the number and types of ions in the pore water. The initial water content and the unfrozen water content affect the electrical resistivity of a frozen soil. The unfrozen water content depends on the temperature and initial water content. The conductive properties of a soil body are affected by the types and number of ions in the pore water. The salt content (for soils that contain salt) determined the types and number of ions. When a soil body contains salt, soluble minerals are dissolved in the pore water and they exist in the form of ions. The migration of positive and negative ions occurs under the effect of an external electrical field. The concentrations of the ions in the pore water and the charge number that each ion carries determine the conductive properties of pore water.

4. Temperature changes the activity of ions and the unfrozen water content. The water in a soil body solidifies and forms ice when the temperature is less than 0°C. When this happens, the unfrozen water content of the soil body decreases and there is a relatively large change in the electrical resistivity of the frozen soil with the water changing from a liquid state to a solid state.

Frozen soil consists of soil particles, ice-water mixtures, and gas. We know from Eq. (7) that factors that affect the electrical resistivity of a frozen soil include the electrical resistivity and the structure coefficient, dry density, water content, content of each component, and temperature. Eq. (7) shows that when the initial water content of the same frozen sample is fixed, the electrical resistivity of the frozen soil is inversely proportional to the unfrozen water content of the soil body. The unfrozen water content varies with changes in the initial water content in frozen samples with different initial water contents. Also, the electrical resistivity of the frozen soil exhibits a complex temperature-related functional relationship with the initial water content. The electrical resistivity of a frozen soil has an exponential relationship with the temperature of the soil body. Also, it is inversely proportional to the dry density of the soil body.

3. Experimental verification of the model for the electrical resistivity of frozen soils

3.1. Electrical resistivity measurement principle

Figure 1 shows the principle diagram of the electrical circuit of the device used to measure the electrical resistivity. To reduce the disturbance of the frozen soil samples, a two-electrode electrical resistivity measurement system was used for electrical resistivity measurements. The electrical resistivity of a soil body is calculated using the following equation:

http://dx.doi.org/10.5772/intechopen.68197

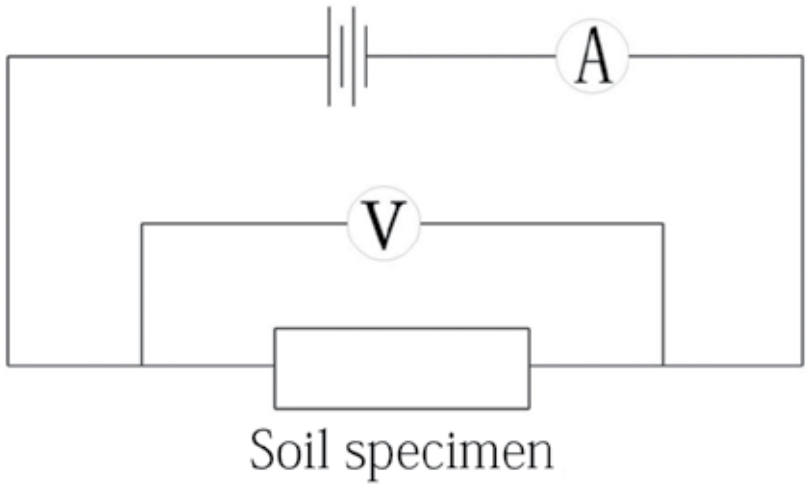

Figure 1. Schematic diagram of the electrical resistivity measurement circuit.

$$\rho = \frac{\pi U D^2}{4IL} \tag{8}$$

where ρ is the electrical resistivity (Ωm), U is the voltage between the two ends of the soil sample (V), I is the current that passes through the soil sample (A), and L is the length of the soil sample (m).

3.2. Experimental materials

The experimental soil sample was silty clay. The original soil samples were sieved, air-dried, and ground for use in the experiment. A 2-mm sieve was used and the soil particles with sizes less than 2 mm were retained and used as the experimental soil sample. The cumulative particle size distribution curve of the experimental soil sample is shown in **Figure 2**. The basic physical properties of the experimental soil sample are shown in **Table 1**. The experimental soil sample had a maximum dry density of 1.89 g·cm^{-3} and the corresponding optimum water content was 13.4%.

3.3. Experimental scheme and steps

The experimental soil was fabricated into a cylindrical specimen with a dry density of 1.52 g·cm^{-3}, an initial volumetric water content of 13.68%, and dimensions ($h \times \phi$) of 300 mm × 158 mm at 24°C to study the variations in the unfrozen water content and the electrical resistivity of the soil body with temperature during the freezing process. Also, the specimen was sealed and then placed in an insulating sleeve with an internal diameter of 160 mm. A water content sensor and a temperature sensor were embedded in the specimen (the temperature sensor had a measurement range of −40 to 50°C and a measurement accuracy of 0.01°C; the water content sensor had a measurement accuracy of 0.01). Copper electrodes with a thickness of 0.5 mm and a purity of 99.5% were placed at each end of the specimen. Subsequently, the specimen was moved outside and allowed to solidify gradually at −24 to −32°C. A LOGGER 3.0 experimental system

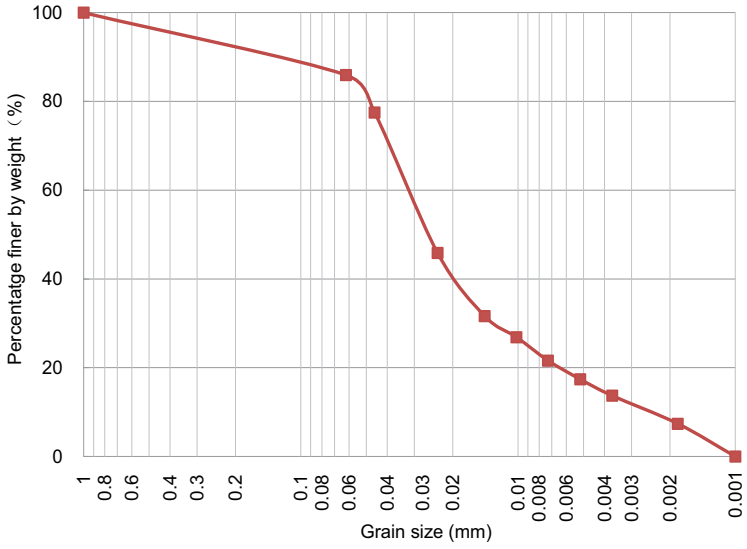

Figure 2. Particle size distribution curve of the soil sample.

Name of the soil sample	Natural water content (w/%)	Optimum water content (w_{op}/%)	Maximum dry density (ρ_d/g·cm^{-3})	Plastic limit (W_P)	Liquid limit (W_L)	Plasticity index (I_p)	Specific weight (Gs)
Silty clay	28.3	13.4	1.89	17.93	33.06	15.13	2.71

Table 1. Basic physical property indexes of the experimental soil sample.

(Beijing Huizenong Tech. Co., Limited is located in Haidian District, Beijing City, China) was employed to automatically acquire the volumetric water content and temperature of the soil body at a 5-minute interval during the freezing process. The electrical resistivity of the specimen was simultaneously measured (**Figure 3**). The variation curves of the electrical resistivity of the soil body and unfrozen water content of the soil body with temperature were obtained after calculating and processing the acquired data (**Figure 5**). The soil water content sensor-working principle was as follows: the standing wave ratio principle was used to measure the volumetric water content, that is, the variation of the dielectric constant (ε) of the soil body is measured and then transformed to the volumetric water content (θ_v) using the Topp equation [34]:

$$\theta_v = -5.3 \times 10^{-2} + 2.92 \times 10^{-2}\,\varepsilon - 5.5 \times 10^{-4}\,\varepsilon^2 + 4.3 \times 10^{-6}\,\varepsilon^3 \quad (9)$$

where θ_v is the volumetric water content and ε is the dielectric constant.

The dry density, temperature, and required soil and water masses were calculated according to the water content and dry density during the experiment to study the relationships between the electrical resistivity of the frozen soil and the initial water content. Water and soil were mixed homogeneously and sealed in a double-layer plastic bag for 12 h to allow the soil sample and water to mix homogeneously. The soil-water mixture was compacted layer by layer into specimens with dimensions ($h \times \phi$) of 80 mm × 39.1 mm according to the different dry density

http://dx.doi.org/10.5772/intechopen.68197

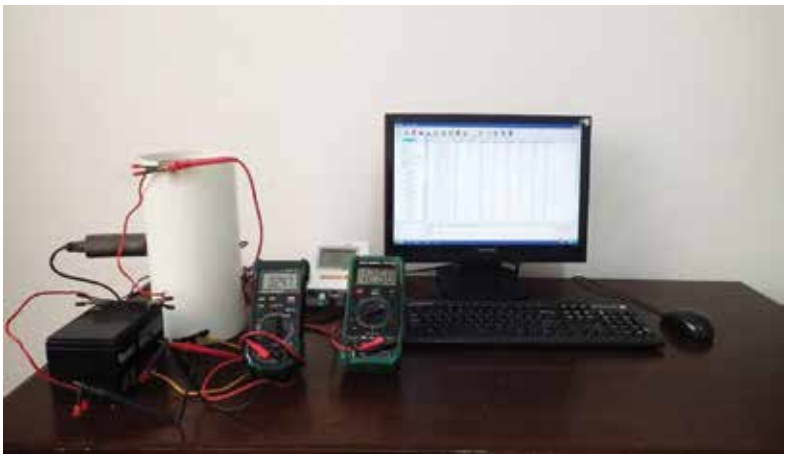

Figure 3. The LOGGER 3.0 system and the electrical resistivity measurement device.

requirements. Each soil specimen was sealed in a rubber membrane to prevent the water content of each soil specimen from changing during the freezing process. The environment of the experiment was a closed system and the experimental soil specimens were placed in a DX-200 low-temperature test chamber. The temperature of the low-temperature test chamber was set to the preset temperature during the experiment and was then maintained for 24 h. Then, the experimental soil specimens were placed in a low-temperature test chamber for 72 h. Three soil specimens were controlled in parallel under each set of conditions with consideration for the discreteness of the soil specimens. A copper electrode was placed at each end of each specimen after the freezing process was completed. Next, each specimen was placed in the device shown in **Figure 4** to measure its electrical resistivity. A DY2101 digital multi-meter was used to measure the voltage of each specimen. The measurement accuracy for the direct current voltage was ±0.5%. A MS8265 digital multi-meter was used to measure the current. The measurement

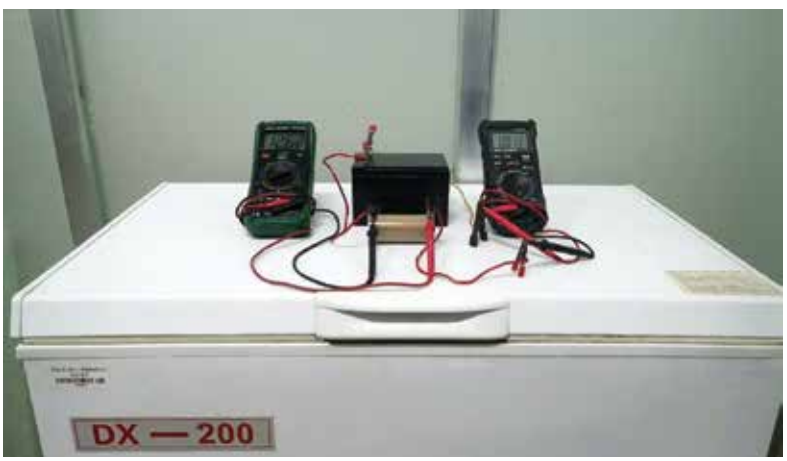

Figure 4. Photograph of the electrical resistivity measurement device.

accuracy for the current was ±0.5%. A DX-200 low-temperature test chamber that had the same temperature as the specimen was used to measure the electrical resistivity of each specimen.

Through manipulating the three factors—the water content (including the unfrozen and initial water content), the temperature, and the dry density—the values of electrical resistivity of the frozen soil for different water contents, temperatures, and dry density conditions were obtained. The curves of the relationships between the electrical resistivity of the frozen soil and different factors are plotted in **Figures 5–13**.

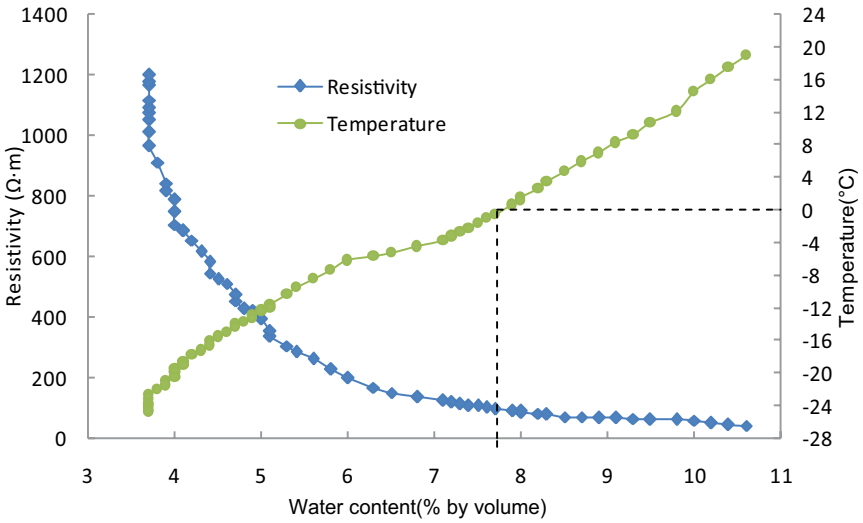

Figure 5. Variation curves of the electrical resistivity of the soil body and unfrozen water content of the soil body with temperature during the freezing process (ρ_d = 1.52 g·cm^{-3}; the initial water content was 13.68%).

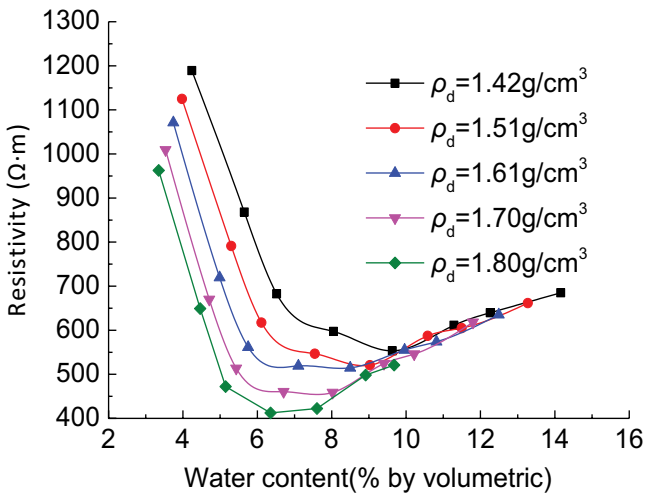

Figure 6. Curves of the relationship between the electrical resistivity of the frozen soil and water content under different dry density conditions (T = −17°C).

http://dx.doi.org/10.5772/intechopen.68197

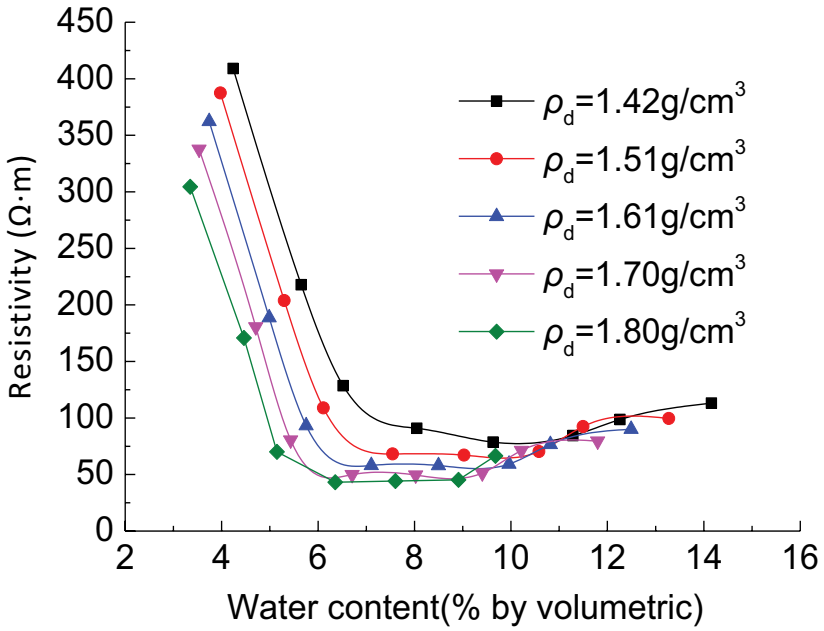

Figure 7. Curves of the relationship between the electrical resistivity of the frozen soil and water content under different dry density conditions ($T = -3°C$).

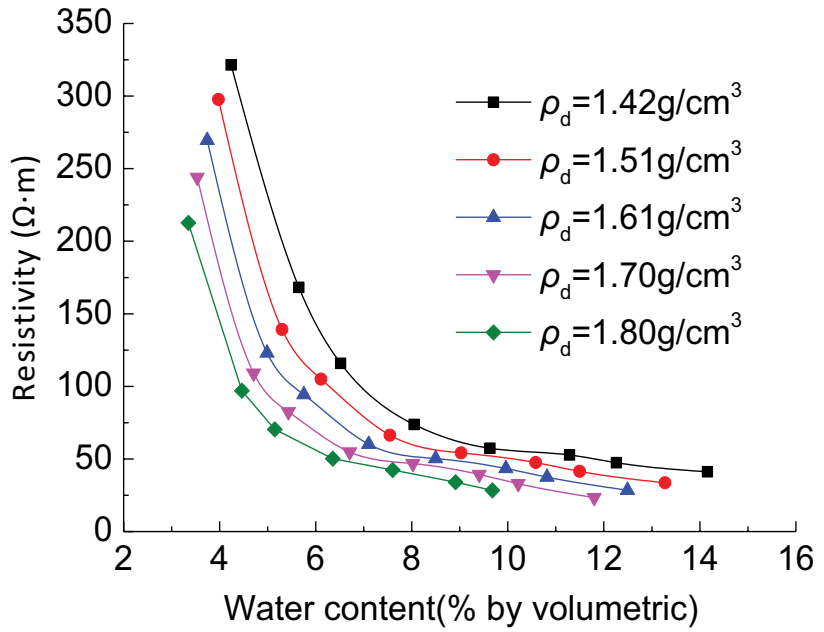

Figure 8. Curves of the relationship between the electrical resistivity of the frozen soil and water content under different dry density conditions ($T = 3°C$).

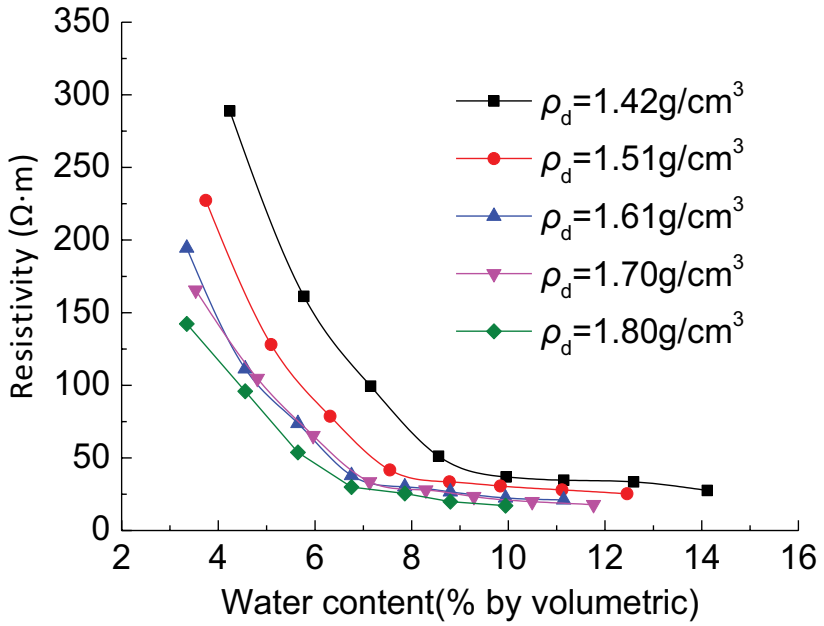

Figure 9. Curves of the relationship between the electrical resistivity of the frozen soil and water content under different dry density conditions (T = 17°C).

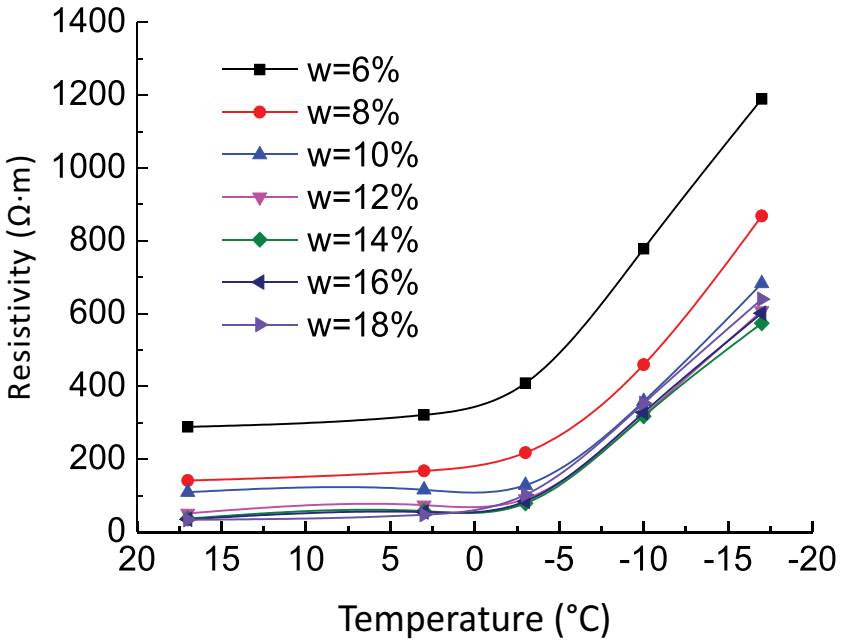

Figure 10. Curves of the relationship between the electrical resistivity and temperature under different water content conditions (ρ_d = 1.42 g·cm^{-3}).

http://dx.doi.org/10.5772/intechopen.68197

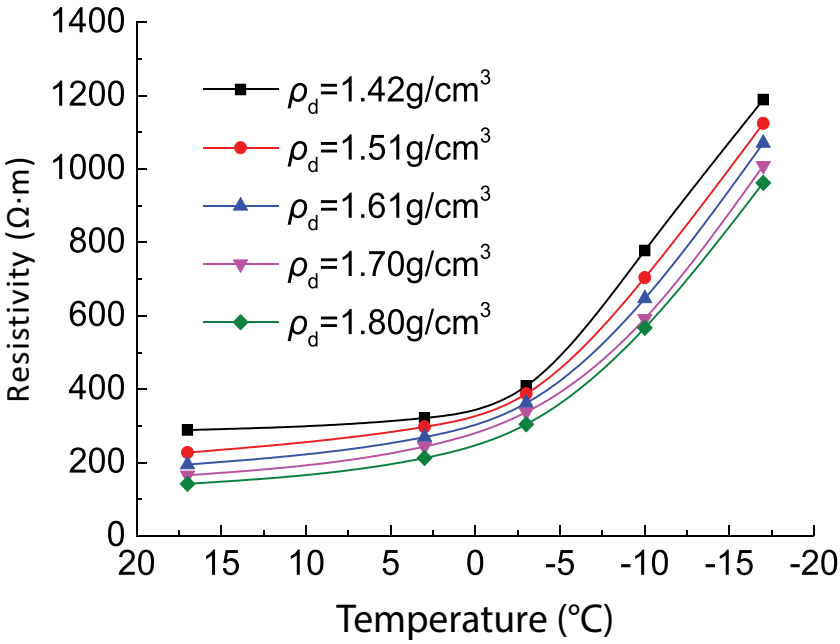

Figure 11. Curves of the relationship between the electrical resistivity and temperature under different dry density conditions (w = 6%).

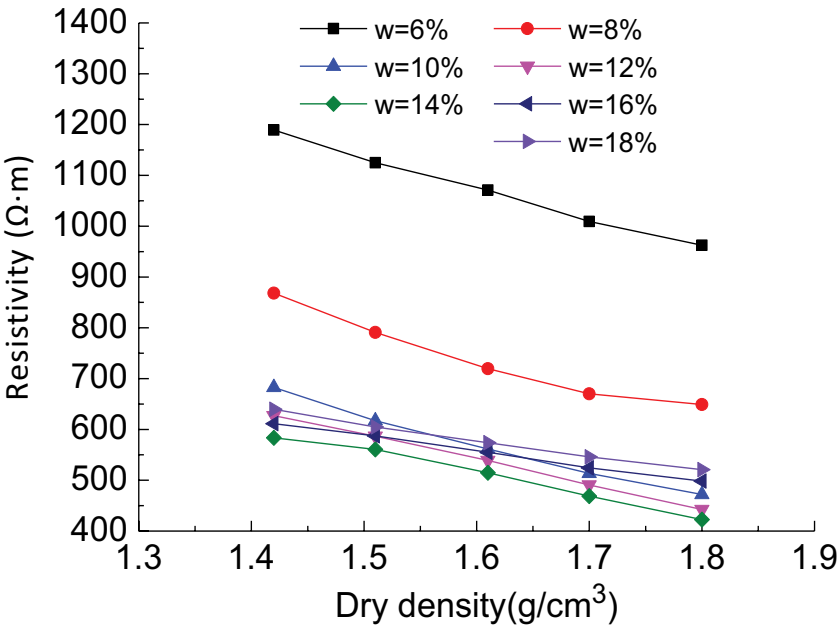

Figure 12. Curves of the relationship between the electrical resistivity and dry density of the frozen soil under different water content conditions (T = −17°C).

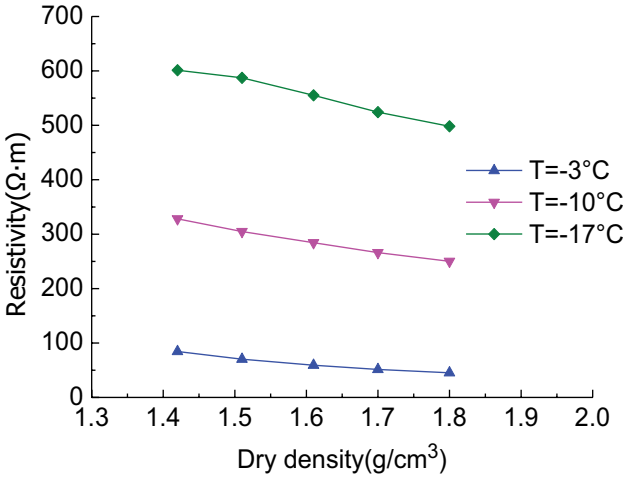

Figure 13. Curves of the relationship between the electrical resistivity and dry density of the frozen soil under different temperature conditions (w = 12%).

4. Analysis of the experimental results

4.1. Effects of the water content

The curve of the relationship between the electrical resistivity of the soil body and the water content, along with the curve of the relationship between the temperature and the water content, is shown in **Figure 5**. Dotted lines mark the volumetric water content of the soil body and the electrical resistivity of the soil body when T = 0°C.

The soil body started to solidify as the temperature was decreased when the temperature was less than 0°C. Also, some of the water in the soil body underwent a phase change. The volumetric water content approximated the unfrozen water content of the frozen soil. The curve of the relationship between the water content and the electrical resistivity of the frozen soil on the left side of the vertical dotted line approximates the relationship between the electrical resistivity of the unfrozen water content and the frozen soil. **Figure 5** shows the experimental curves indicating that the electrical resistivity of the frozen soil decreased with increases in the unfrozen water content of the frozen soil. The relationship between the electrical resistivity of the frozen soil and the unfrozen water content obtained through fitting was the following:

$$\rho = \frac{6172}{\theta_v} - 739, \quad R^2 = 0.910 \tag{10}$$

From Eq. (7), we know that in the model, the electrical resistivity of the frozen soil is inversely proportional to the unfrozen water content, which depends on the temperature; this relationship is consistent with the experiment results, thus verifying the reasonableness of the relationship between the unfrozen water content and the electrical resistivity in the proposed model for the electrical resistivity of frozen soils.

Figures 6–9 show the curves of the relationship between the electrical resistivity of each frozen soil specimen and the initial water content under different dry density conditions (the unfrozen soil [T = 3°C, T = 17°C] is used as the reference); the volumetric water contents shown in **Figures 6–9** were converted from the mass water contents. It can be observed from the experimental curves that the electrical resistivity of the frozen soil first rapidly decreased and then slowly decreased with increasing initial water content of the soil body, and the electrical resistivity of the frozen soil reached its minimum value near the optimum water content. When the initial water content was greater than the optimum water content, the effect of the dry density on the electrical resistivity of the frozen soil gradually decreased. The effect of the variation of the water content on the electrical resistivity of the frozen soil increased with decreasing temperature because of the following reasons: the effect of the variation of the water content on the electrical resistivity of the frozen soil decreased with the decreasing temperature, with increasing water content (i.e., increasing ice content of the frozen soil); the electrical resistivity of ice was greater than that of unfrozen water, thereby resulting in more rapid changes in the electrical resistivity of the frozen soil.

4.2. Effects of the temperature

The variation curves of the electrical resistivity of the frozen soil with temperature under different water content conditions (ρ_d = 1.42 g·cm^{-3}) and the variation curves of the electrical resistivity of the frozen soil with temperature under different dry density conditions (w = 6%), respectively, are shown in **Figures 10** and **11**. The unfrozen soil was used for comparison (T = 3°C, T = 17°C). The curves show that the electrical resistivity of the frozen soil increased with decreasing temperatures. We know that, in the proposed model (Eq. (7)), when there is a change in the dry density of the frozen soil or the water content of the frozen soil, the electrical resistivity of the frozen (ρ) is exponentially related to the temperature of the frozen soil (θ; the related parameters are different). This dependence is completely consistent with the experimental results. Thus, the reasonableness of the relation between the temperature and the electrical resistivity in the model for the electrical resistivity of frozen soils was verified. The decrease in temperatures resulted in a decrease in the unfrozen water content of the frozen soil, which then resulted in an increase in the electrical resistivity of the frozen soil. Since the soil sample still contained a large amount of unfrozen water at −3°C, there was no significant change in the electrical resistivity of the frozen soil when the temperature of the soil decreased from 17 to −3°C. Therefore, this resulted in a significant decrease in the electrical resistivity of the soil sample. The effect of temperature on the electrical resistivity of the frozen soil decreased with increases in the water content.

4.3. Effects of the dry density

The variation curves of the electrical resistivity of the frozen soil with the dry density under different initial water content conditions (T = −17°C) and the variation curves of the electrical resistivity of the frozen soil with the dry density under different temperatures (w = 12%) are shown in **Figures 12** and **13**, respectively. The experimental curves show that the electrical resistivity of the frozen soil decreased with increasing dry density in all cases. In the proposed model (Eq. (7)), it is known that when there is a change in the initial

water content of the frozen soil or the temperature of the frozen soil, the electrical resistivity of the frozen soil (ρ) is inversely proportional to the dry density of the frozen soil (ρ_d; the related parameters in the relationships are different). This dependence was consistent with the experimental results. This verified the reasonableness of the relationship between the dry density and the electrical resistivity of the frozen soil in the proposed model for the electrical resistivity of frozen soils. The porosity of the soil sample decreased when the dry density of the soil sample increased. The unfrozen water content of the frozen soil was the same under the same initial water content and temperature conditions. The increase in the dry density of the frozen soil resulted in a decrease in the electrical resistivity. This was due to the increase in the number of connections between soil particles. The effect of the variation of the dry density on the electrical resistivity of the frozen soil decreased with increases in the water content.

4.4. Effects of the freezing mode and salt content

During the freezing process of a soil body, water migration always occurs. The formation of various cryogenic structures, ice lenses, and different freezing temperatures and modes results in different freezing rates and ice nucleation modes of the water in a soil. There are different impacts on the electrical resistivity of the frozen with different ice nucleation modes. In the present study, however, the specimens were only frozen unidirectionally in a closed system.

The salt contents of the soil body are also primary factors that affect the electrical resistivity of the frozen soil [35]. However, the salt contents of the soil body were not considered in the present study. Further studies are necessary to investigate the relationship between the electrical resistivity of a frozen soil and the salt content of the frozen soil.

5. Application examples of resistivity

5.1. Study area

The K161 road section of Bei'an-Heihe Expressway was selected as the study area. This area intersects the northwest section of Lesser Khingan Mountains at the junction of Sunwu County and Heihe City, China's Bei'an-Heihe Expressway between 127°17′31″—127°21′24″– east longitude and 49°30′57″—49°41′50″– north latitude (**Figure 14**). The study area has a continental monsoon climate; a short spring quickly moves into a warm and rainy summer, followed by a short autumn accompanied by a rapid drop in temperature, and a long and cold winter. The annual average temperature is 0.6°C, the lowest temperature is −48.1°C, and the highest is 35.2°C. Soil in the study area begins to freeze at the end of October each year, and extends to a maximum seasonal freezing depth of between 2.26 and 2.67 m. The frozen soil on the ground surface begins to melt in April, and the melting stage lasts from April to September. In dry regions, all the frozen soils will melt by about early July, whereas in swampy regions, the thick layers of peat and humus will not melt until October. Seasonal frozen soil is well developed in the study area and "islands" of permafrost are also distributed in some gully areas.

http://dx.doi.org/10.5772/intechopen.68197

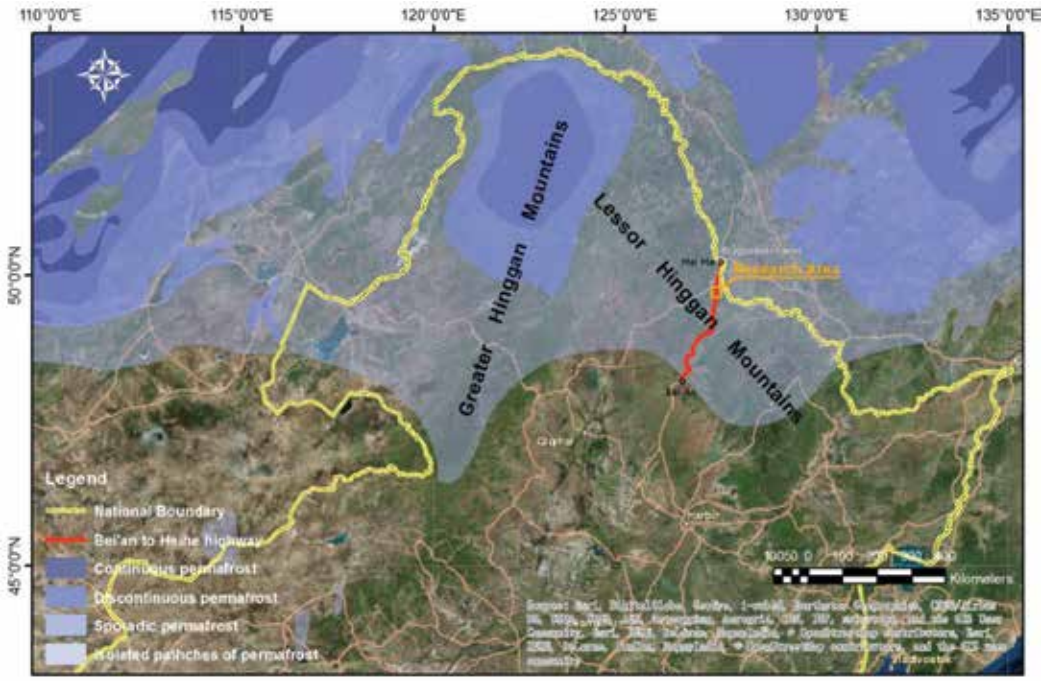

Figure 14. The permafrost distribution map at high latitudes in Northeast China and geographical location of the study area (data courtesy of the University of Zurich).

The area is located in the southern margin of China's high-latitude permafrost region, where the island permafrost is sedimentary residue of the ancient glacier and is currently in a degradation stage. The Bei'an-Heihe Expressway is an expressway widened and expanded based on the original Heihe-Bei'an Second-Class Highway, which was built in 1997 and completed and opened to traffic in 2000. As indicated by the Research Report on Engineering Geological Investigation and Evaluation of Permafrost in the Heihe-Bei'an Section of the Heihe-Dalian Highway, there are 17 road sections containing island permafrost along the Heihe-Bei'an Highway in 2000. In 2009, an engineering geological investigation of the whole area along the Heihe-Bei'an Highway showed that there were only seven road sections containing island permafrost and that permafrost in the other 10 road sections had disappeared. Compared with the investigation results in 2009, the permafrost layers in the seven road sections are now even more reduced in length and thickness, and the lower limits of permafrost are no longer as deep. The temperature of the study area has been increasing in recent decades and the ground temperature has increased as well. If the ground temperature of the study area continues to rise in the coming decades, the permafrost in this area will continue to degrade.

The tectonic structure of the study area is located in the new Wuyun-Jieya Fault Depression Belt, with the Handaqi Fold Belt on the north and the Shuhe uplifted belt on the south. The exposure strata (from old to new) include the Nenjiang Formation of Upper Cretaceous, the Sunwu Formation of Tertiary System, and the Modern River Alluvium of the Holocene

Series of Quaternary System. Permafrost is mainly distributed in the Modern River Alluvium of the Holocene Series and the Nenjiang Formation of the Upper Cretaceous. Water inputs in the study area mainly from the surface water, ground water, and underground ice.

5.2. Geological survey

The island permafrost in the study area is developed in the low-lying marshlands where there is surface water, overgrown grasses, and thickly accumulated turf and peat. The fundamental reason for the maintenance and preservation of degraded permafrost is that the amount of heat in permafrost is insufficient to melt permafrost in the short term. These marshes provide abundant material resources for evaporation in the warm season, which dissipates a large amount of heat in the atmosphere in the form of latent heat. Additionally, the dense grasses and the rich turf and peat under the soil surface are good thermal insulation materials that prevent the heat absorbed on the surface from being spread to the deep sections of the soil, preventing the temperature of permafrost from rising. In the freezing period, water in the wetland is turned into ice, increasing the thermal conductivity of the soil layer. However, during this freezing period the soil releases heat into the atmosphere. Enhanced thermal conductivity further increases the amount of heat released by the soil layer, which can also lower the temperature of the permafrost. These characteristics of wetlands directly affect the long-term preservation of island permafrost in the permafrost areas.

In this study, we investigated the engineering geological and hydrogeological conditions of the study area and measured its upper and lower limits of permafrost. In July 2009, five drill holes were arranged at the left slope toe, left shoulder, central separator, right shoulder, and right slope toe of the road (drilling locations are shown in **Figure 15**). An engineering geological section map of the study section was drawn according to the drilling results (**Figure 15**).

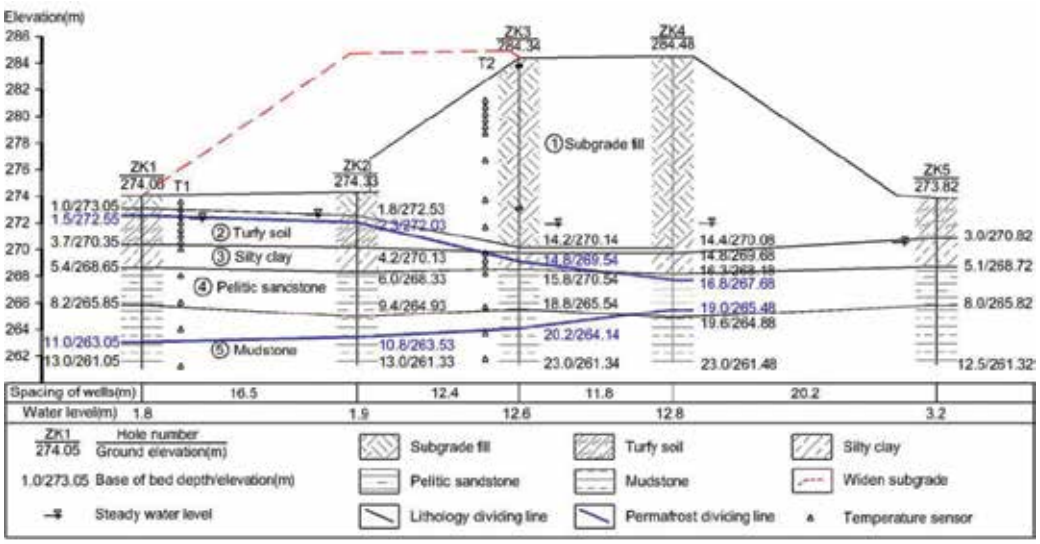

Figure 15. The geological section map.

Soils and rocks in the control area include Quaternary loose soils, Cretaceous sandstone, and mudstone. The subgrade fill is mainly yellow pebbly sandstone which is slightly dense and permeable. The turf contains incompletely decomposed grassroots, with a layered and patchy frozen soil structure that is brownish black, saturated, and soft plastic. The silty clay layer is black, wet, hard plastic, and glossy, with relatively large dry strength and toughness, and a layered and patchy frozen soil structure. The argillaceous sandstone contains partial fine sandstone lens, with weak cementation, pelitic texture, layered structure, and a micro-layer, and layered frozen soil structure that is gray-black, wet, and hard plastic. The mudstone layer is gray-black, wet, and hard plastic, with weak cementation, pelitic texture, layered structure, and a layered frozen soil structure.

The ground water was comparatively deep at a subgrade depth of 12.4–12.5 m and relatively shallow at the slope toe at a depth of 1.7 m. The upper limit of permafrost was 15.8–16.8 m and the lower limit was 19.0–20.3 m at the old subgrade and the permafrost thickness was less than 5.0 m. The upper limit of permafrost in the original ground was 1.5–2.3 m, the lower limit was 9.2–10.8 m, and the permafrost thickness was 7.7–8.5 m. Affected by the old road filling, the permafrost beneath the old subgrade had degraded significantly and there was no permafrost at the right slope toe.

To explore the temperature change of permafrost below the subgrade during construction and operation of roads, we used the SUR-3 soil temperature sensor produced by the Beijing Huizenong Technology Co., Ltd. This drilling machine has a measurement range of −40 to 120°C. The machine was used to drill holes at two test points, T1 and T2, and soil temperature sensors were embedded in these drilled holes. T1 and T2 were close to ZK1 and ZK3, respectively. **Figure 15** shows the layout of the temperature sensors.

5.3. The HDR method

The HDR method was used to conduct a geophysical exploration of the K161 road section. Three HDR measuring lines were arranged in the K161 road section: I–I′, II–II′, and III–III′ (**Figure 16**).

The instrument used in this study was the WGMD-9 super HDR measurement system produced by the Chongqing Benteng Numerical Control Technique Research Institute. With the super WDA-1 digital-DC electrical prospecting apparatus as the measurement and control host, the system realizes the centralized 2D measurement of high-density resistivity by matching the WDZJ-4 multi-channel switcher and centralized high-density cables and electrodes. The 2DRES HDR method was used to invert the field data. The inversion model was based on the smooth-constrained least-squares method. In brief, this method constantly adjusts the resistivity of the model via model corrections to reduce the difference between the calculated apparent resistivity and the measured apparent resistivity, and it describes the fitting degree between the two using the mean square error. The least-squares method based on smooth constraint is an approach that is widely used because it can be adapted to different types of data and models, data inversion is fast and less affected by noise, the method has high sensitivity to deep units, and there are only a small number of iterations.

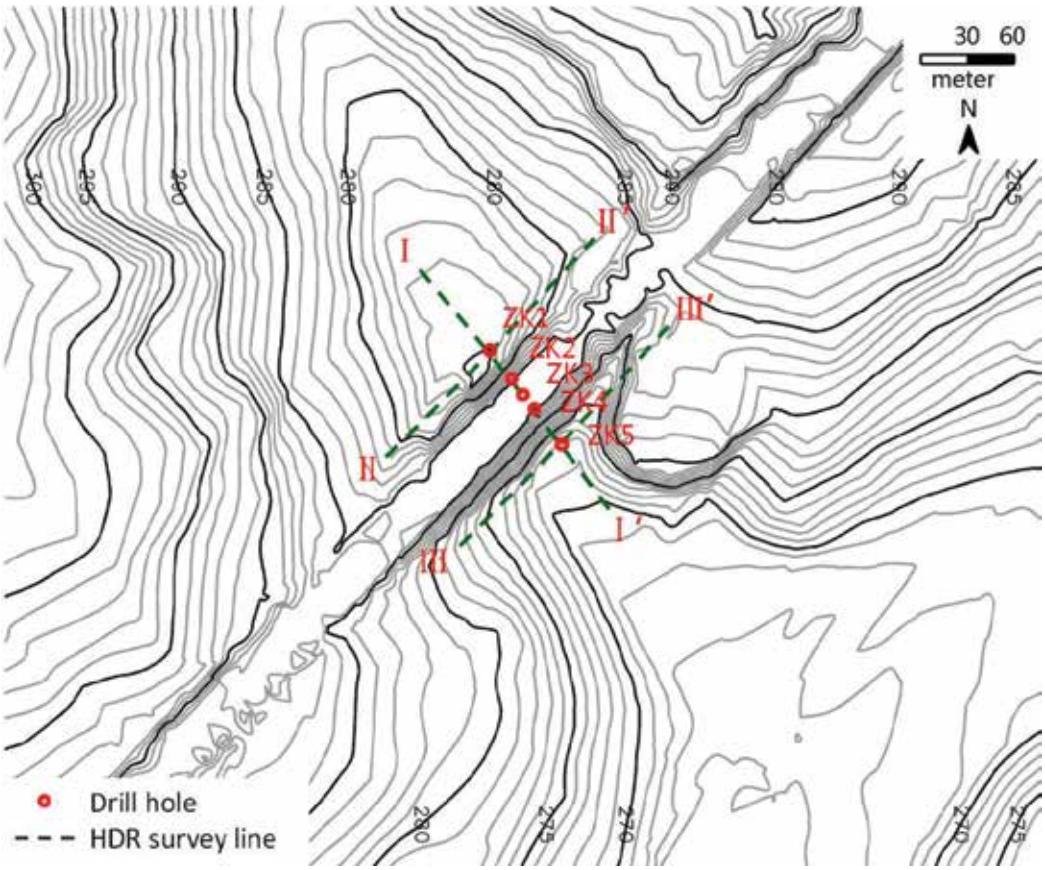

Figure 16. The arrangement plan of the HDR measuring lines in the K161 road section. HDR measuring line: (1) located on the cross section of K161+440, the I–I′ measuring line is perpendicular to the road direction; the starting point of the measuring line is 60 m away from the left slope toe of the road, and the line passes ZK1, ZK2, ZK3, ZK4, and ZK5 in succession; the end of the measuring line is located 60 m outside the right slope toe of the road. (2) Located at the left slope toe of the road, the II–II′ measuring line is parallel to the road direction, with ZK1 as the midpoint, with the starting point in the southwest and the end point in the northeast. (3) Located at the right slope toe of the road, the III–III′ measuring line is parallel to the road direction, with ZK5 as the midpoint, with starting point in the southwest and the end point in the northeast. All the three HDR measuring lines are 177 m long. The Wenner arrangement method was used to arrange the measuring lines, with the electrode spacing at 3.0 m and the limit surrounding at 30 m.

5.4. Analysis and discussion on the HDR method and ground temperature data

5.4.1. Ground temperature data

A contour map showing the variation of different ground temperatures and depths with time was drawn according to the ground temperature data of rock and soil monitored by the temperature sensor at T1 (**Figure 17** shows the variation of the upper and lower limits of the permafrost at T1 over time). In July 2009, the upper limit of the permafrost was 272.7 m, the lower limit was 263.0 m, and the thickness was 9.7 m. When ground temperature monitoring began in September 2009, the upper limit of the permafrost was 272.5 m, the lower limit was 263.2 m, the thickness was 9.3 m, and the lowest temperature of the permafrost was −1.2°C

http://dx.doi.org/10.5772/intechopen.68197

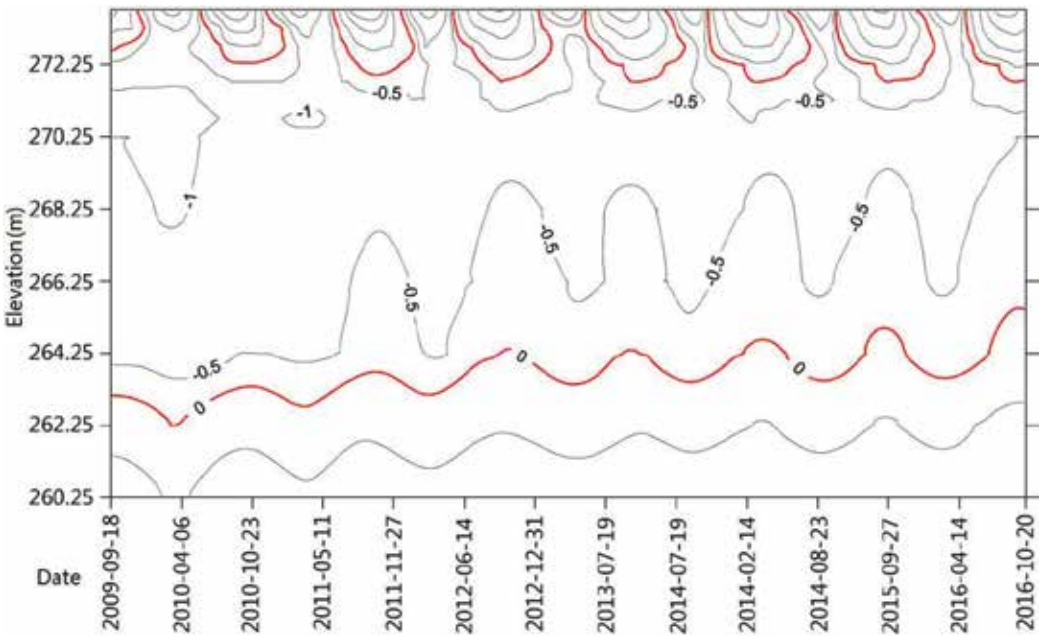

Figure 17. A contour map of ground temperature at T1 (the 0°C isothermal indicates the upper and lower limits of the permafrost).

(**Figure 17**). Seasonally frozen soil and permafrost at T1 were linked together on May 5 each year. On May 5, 2010, the lower limit of the permafrost was 262.4 m; on September 25, 2010, the upper limit of the permafrost was 272.3 m, the lower limit was 263.4 m, the thickness was 8.9 m, and the minimum temperature was −1.0°C. On May 5, 2011, the lower limit of the permafrost was 262.9 m; on September 25, 2011, the upper limit of the permafrost was 271.9 m, the lower limit was 263.8 m, the thickness was 8.1 m, and the minimum temperature was −0.9°C. On May 5, 2012, the lower limit of the permafrost was 263.1 m; on September 25, 2012, the upper limit of the permafrost was 271.7 m, the lower limit was 264.2 m, the thickness was 7.5 m, and the minimum temperature was −0.7°C. On May 5, 2013, the lower limit of the permafrost was 263.2 m; on September 25, 2013, the upper limit of the permafrost was 271.7 m, the lower limit was 264.3 m, the thickness was 7.4 m, and the minimum temperature was −0.7°C; on May 5, 2014, the lower limit of the permafrost was 263.3 m; on September 25, 2014, the upper limit of the permafrost was 271.7 m, the lower limit was 264.8 m, the thickness was 6.9 m, and the minimum temperature was −0.6°C. On May 5, 2015, the lower limit of the permafrost was 263.5 m; on September 25, 2015, the upper limit of the permafrost was 271.7 m, the lower limit was 265.4 m, the thickness was 6.3 m, and the minimum temperature was −0.6°C. On May 5, 2016, the lower limit of the permafrost was 263.8 m; on September 25, 2016, the upper limit of the permafrost was 271.7 m, the lower limit was 265.6 m, the thickness was 6.1 m, and the minimum temperature was −0.5°C.

Ground temperature data suggested that road construction affected the permafrost, since the road was near the subgrade at the left slope toe. The upper limit of the permafrost decreased significantly while the lower limit increased significantly during the road construction. Affected

by temperature and permafrost, the rock and soil strata near the upper and lower limits of the permafrost in this position froze and thawed repeatedly. The overall trend was permafrost degradation as a result of changes in climate, characterized by a rise of the permafrost temperature, a decline of the upper limit, a rise of the lower limit, and a decrease in the thickness.

Figure 18 depicts a contour map at T2 showing the variation in ground temperature and depth of the rock and soil strata and the variation of the upper and lower limits of the permafrost at T2 over time. At T2 at the start of the investigation in July 2009, the upper limit of the permafrost was 269.3 m, the lower limit was 263.3 m, and the thickness was 6.0 m. When the ground temperature monitoring was started in September 2009, the upper limit of the permafrost was 269.2 m, the lower limit was 263.7 m, the thickness was 5.5 m, and the lowest temperature of the permafrost was −0.9°C (**Figure 18**). On September 3, 2010, the upper limit of the permafrost was 268.1 m, the lower limit was 264.8 m, the thickness was 3.3 m, and the minimum temperature of the permafrost was −0.6°C. On September 25, 2016, the upper limit of the permafrost was 266.8 m, the lower limit was 265.2 m, the thickness was 1.6 m, and the minimum temperature of the permafrost was −0.4°C. The height of the subgrade fill at T2 reached 10.4 m, which caused an obvious degradation of the permafrost. During the road construction, the upper limit of the permafrost declined, the lower limit rose, and its thickness significantly decreased. Affected by temperature and permafrost, the rock and soil strata near the upper and lower limits of the permafrost in this position froze and thawed repeatedly. Overall, there was a trend of permafrost degradation as a result of changes in climate.

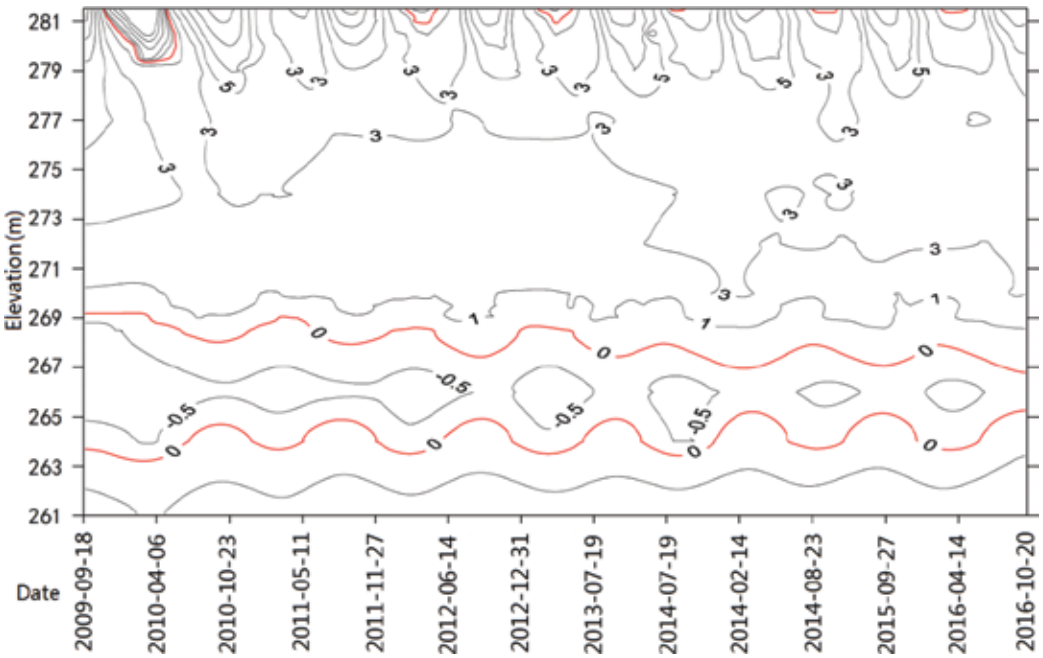

Figure 18. A contour map of ground temperature at T2 (the 0°C isothermal indicates the upper and lower limits of the permafrost).

http://dx.doi.org/10.5772/intechopen.68197

5.4.2. I–I′ measuring line

Figure 19 shows the HDR inversion image of I–I′ measuring line on September 3, 2010. As indicated by the inversion image, the resistivity stratification of the soil under the measuring line is relatively obvious. To better analyze the variation of soil resistivity with depth, the 2DRES HDR-processing software was used to extract the curve of resistivity at any point on the measuring line. **Figure 20** shows the resistivity curves of the soil at ZK1, ZK2, ZK3, ZK4, and ZK5 as depth changes. According to the resistivity characteristics of the foundation soil on site, soil with resistivity greater than 90 Ωm is probably frozen soil. On September 3, 2010, the upper limit of the frozen soil at ZK1 was 273 m, the lower limit was 263.6 m; the upper limit of the frozen soil at ZK2 was 271.6 m and the lower limit was 264.5 m; the upper limit of

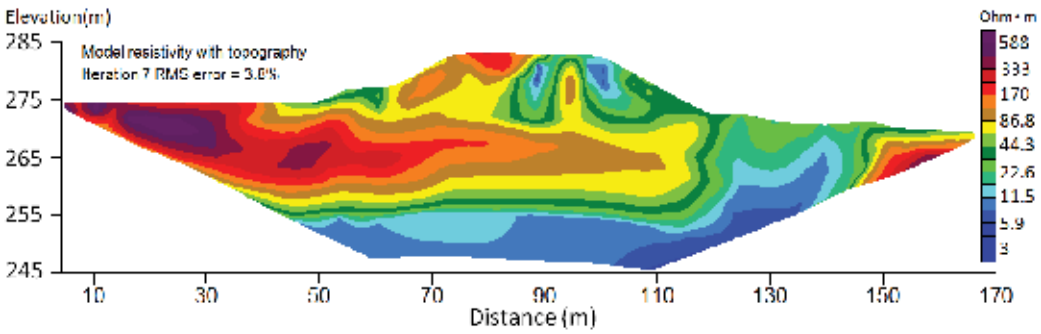

Figure 19. An HDR inversion image of the I–I′ measuring line.

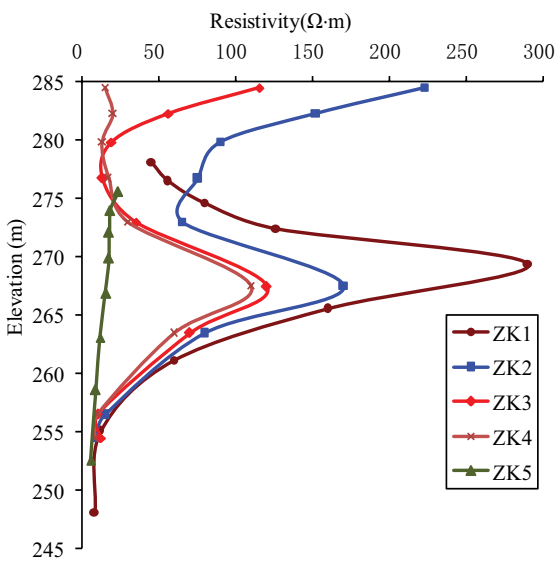

Figure 20. Resistivity curves at different positions of the I–I′ measuring line.

the frozen soil at ZK3 was 269 m and the lower limit was 264.6 m; the upper limit of the frozen soil at ZK4 was 268.3 m and the lower limit was 265.7 m; there was no permafrost at ZK3. The comparison of the temperature-monitoring data at T1 and T2 suggests that there is no difference between the upper and lower limits of permafrost at ZK1 and ZK3, and the position of permafrost inferred by the resistivity data was accurate.

5.4.3. II–II′ measuring line

To explore the variation of permafrost on the II–II′ measuring line, four HDR detection analyses were carried out on the II–II′ measuring line on May 5, 2010, May 5, 2012, May 5, 2014,

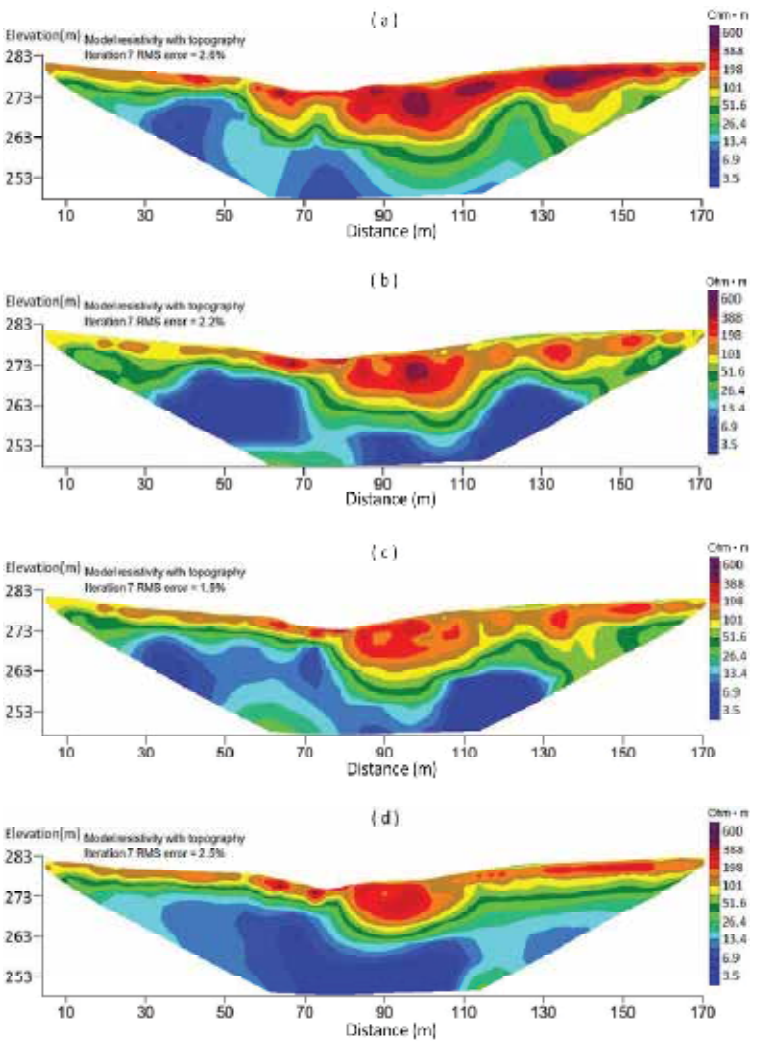

Figure 21. The HDR inversion image of the II–II′ measuring line in May. The measurement dates were May 5, 2010 (a), May 5, 2012 (b), May 5, 2014, (c) and May 5, 2016 (d).

http://dx.doi.org/10.5772/intechopen.68197

and May 5, 2016 (**Figure 21** shows the images gained by these detections). Five HDR detection analyses were carried out on the II–II′ measuring line on September 25, 2010, September 25, 2012, September 25, 2014, September 25, 2015 and September 25, 2016 (**Figure 22** shows the images gained by these detections). ZK1 is a cross section of the K161+440 Road at 90 m from the starting point on II–II′ measuring line.

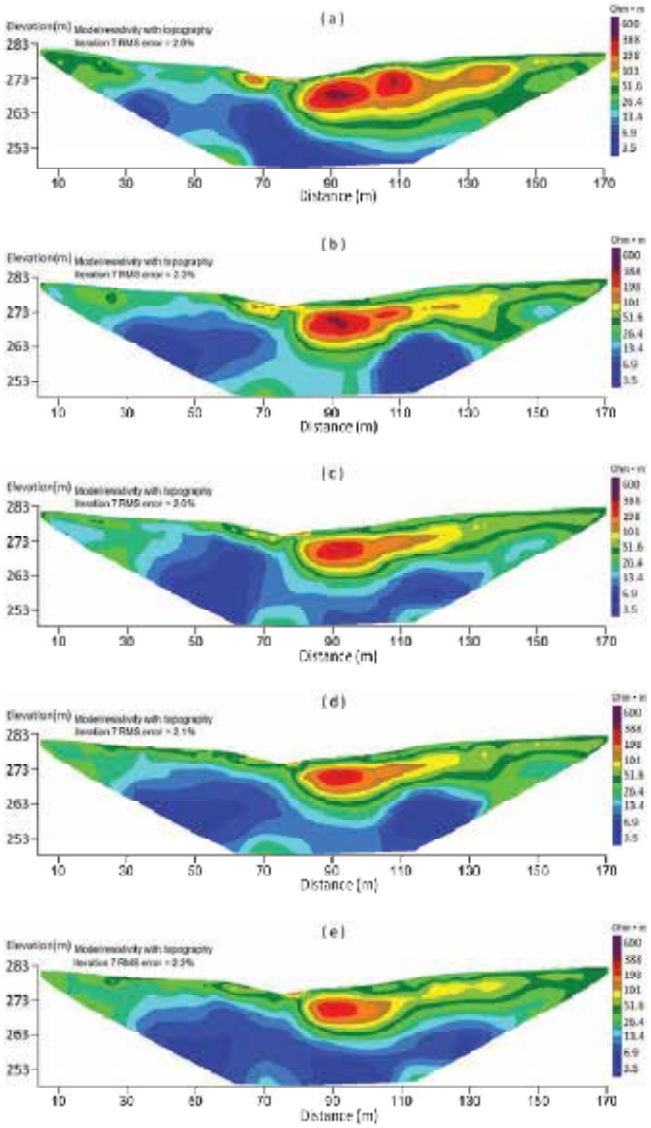

Figure 22. The HDR inversion image of the II–II′ measuring line in September. The measurement dates were September 25, 2010 (a), September 25, 2012 (b), September 25, 2014 (c), September 25, 2015 (d), and September 25, 2016 (e). The surface layer of the K161+424-K161+432 road section (74–82 m away from the starting point) is composed of concrete at the mouth of the culvert and thus this measuring line had a relatively high resistivity.

The lower limits of permafrost at ZK1 were 262.5, 263.0, 263.0, and 264.1 m, respectively, on May 5, 2010, May 5, 2012, May 5, 2014, and May 5, 2016. The upper limits of permafrost at ZK1 were 272.5, 272.0, 272.0, 272.0, and 272.0 m, respectively, on September 25, 2010, September 25, 2012, September 25, 2014, September 25, 2015, and September 25, 2016, with the lower limits being 263.4, 264.0, 264.5, 265.1, and 265.3 m, respectively.

Compared with the lower limit of permafrost obtained by the temperature data at T1, the difference between the upper and lower limits of permafrost measured by the HDR method was small, indicating that the position of permafrost detected by the HDR method on II–II′ measuring line was accurate.

As shown by the measurement results obtained on II–II′ measuring line, both the area and resistivity of the high-resistivity areas were shrinking during the period analyzed, indicating that the permafrost at the left slope toe of the road was constantly degrading. The upper limit of the permafrost was declining, the lower limit was moving up, the temperature was rising, and the total area was decreasing. As shown in **Figure 22**, on II–II′ measuring line, permafrost was found in the following road sections on the following dates: K161+414-K161+422 and K161+431-K161+494 in September 2010; K161+414-K161+422 and K161+431-K161+484 in September 2012; K161+432-K161+477 in September 2014; K161+432-K161+472 in September 2015; and K161+433-K161+460 in September 2016.

5.4.4. III–III′ measuring line

To explore the distribution of permafrost on III–III′ measuring line, HDR detection analyses were conducted on III–III′ measuring line on September 25, 2010 and September 25, 2014 (images are shown in **Figure 23**). ZK5 is a cross section of the K161+440 road at 90 m from the starting

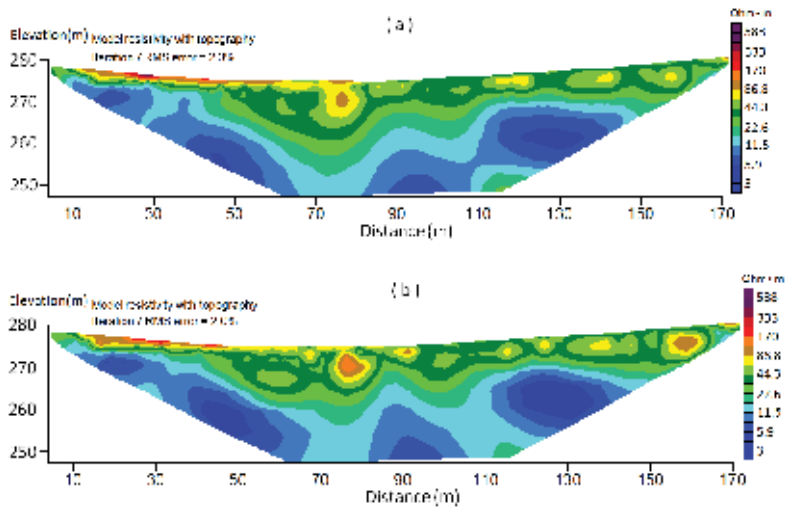

Figure 23. The HDR inversion images of the III–III′ measuring line over time. The measurement dates were September 25, 2010 (a) and September 25, 2014 (b). The surface layer of the K161+424-K161+432 road section (74–82 m away from the starting point) on the measuring line was a culvert within the depth of 0–5 m, thus this line had a relatively high resistivity.

point on III–III′ measuring line. The measurement results about the distribution of permafrost in the foundation soil beneath III–III′ measuring line agreed with the drilling results (**Figure 23**).

6. Conclusions

1. The electrical resistivity of the frozen soil was shown to be inversely proportional to the unfrozen water content of the soil body. Temperature determined the exact proportionality. The electrical resistivity of the frozen soil decreased with increases in the unfrozen water content of the soil body. The electrical resistivity of the frozen soil showed a complex temperature-related functional relationship with the initial water content. The electrical resistivity of the frozen soil rapidly decreased at first and then gradually increased with increases in the initial water content of the soil body. The electrical resistivity of the frozen soil tended to stay at the minimum value near the optimum water content. The effect of the dry density on the electrical resistivity of the frozen soil gradually decreased when the initial water content was greater than the optimum water content. The effect of the variation of the water content on the electrical resistivity of the frozen soil increased with decreases in the temperature.

2. The electrical resistivity of the frozen soil was exponentially related to the temperature of the soil body. The electrical resistivity of the frozen soil increased with decreasing temperature. The effect of the temperature of the frozen soil on the electrical resistivity of the frozen soil decreased with increasing water content. When there was a change in the dry density of the frozen soil, the effect of the temperature on the electrical resistivity of the frozen soil was effectively unchanged.

3. The electrical resistivity of the frozen soil was inversely proportional to the dry density of the soil body. The electrical resistivity of the frozen soil decreased with increasing dry density. The effect of the dry density of the frozen soil on the electrical resistivity gradually decreased with increasing water content. The effect of the dry density on the electrical resistivity of the frozen soil increased with decreasing temperature.

4. The relationships between the electrical resistivity of a frozen soil and the various influencing factors were basically consistent with the relationships described by the fitted equations obtained from the experiments, based on the model of the electrical resistivity of frozen soils. This verified the reasonableness of the model for the electrical resistivity of frozen soils. More studies are needed to investigate the related parameters in the model for the electrical resistivity of frozen soils.

5. The results of geological drilling, temperature monitoring, and HDR detection analyses suggest that a widened and expanded subgrade have had a significant influence on permafrost in the K161 road section. During the subgrade construction, the permafrost was degraded as a result of both road construction and climatic change. Permafrost temperatures rose, the upper limit of permafrost declined, the lower limit of permafrost rose, and the overall thickness of the permafrost significantly decreased.

6. The positions of permafrost estimated by the HDR method were in agreement with the results obtained from geological drilling, temperature monitoring, and the electrical

survey, indicating that HDR is a fast, economical, and reliable method for on-site exploration of permafrost. HDR can be used to quickly and accurately locate the position of underground permafrost in high-latitude permafrost regions, providing an accurate reference for linear engineering positioning and corresponding engineering measures.

Acknowledgements

Parts of this chapter are reproduced from authors' recent publication [14, 33]. This project is supported by the Natural Science Foundation of China (Grant No. 41641024).

Author details

Wei Shan*, Zhaoguang Hu, Ying Guo, Chengcheng Zhang and Yao Liu

*Address all correspondence to: shanwei456@163.com

Institute of Cold Regions Science and Engineering, Northeast Forestry University, Harbin, China

References

[1] Wu J, Li CB, Sun HZ. Preliminary observations of the variation of the electrical resistivity of a soil under in-situ conditions. Chinese Journal of Soil Science. 1985:**2**;13 (in Chinese).

[2] Li L, Zhou ZH, Zhang HY. Experimental study on the electrical resistivity of saline soils. Environmental Engineering. 2012;**30**:498–503 (in Chinese with English abstract).

[3] Zha FS, Liu SY, Du YJ, Cui KR. Effect of soil grain composition on soil electrical resistivity. Industrial Construction 2013;**43**(3):71–74 (in Chinese with English abstract).

[4] Fortier R, Allard M, Seguin MK. Effect of physical properties of frozen ground on electrical resistivity logging. Cold Regions Science and Technology. 1994;**22**(4):361–384.

[5] Fortier R, LeBlanc AM, Allard M, Buteau S, Calmels F. Internal structure and conditions of permafrost mounds at Umiujaq in Nunavik, Canada, inferred from field investigation and electrical resistivity tomography. Canadian Journal of Earth Sciences. 2008;**45**(3):367–387.

[6] Delaney AJ, Peapples PR, Arcone SA. Electrical resistivity of frozen and petroleum-contaminated fine-grained soil. Cold Regions Science and Technology. 2001;**32**(2):107–119.

[7] Fu W, Wang R, Hu MJ, Xiang YH. Study of relationship between uniaxial compressive strength and electrical resistivity of frozen soil under different temperatures. Rock and Soil Mechanics. 2009;**30**(1):73–78 (in Chinese with English abstract).

[8] Angelopoulos MC. Integrated geophysical approach for the detection and assessment of ground ice at Parsons Lake, Northwest Territories, Northwest Territories [MSc thesis]. Montreal, Quebec, Canada: McGill University; 2010.

[9] McCann DM, Forster A. Reconnaissance geophysical methods in landslide investigations. Engineering Geology. 1990;**29**:59–78.

[10] Hack R. Geophysics for slope stability. Surveys in Geophysics. 2000;**21**:423–448.

[11] Benedetto A, Benedetto F, Tosti F. GPR applications for geotechnical stability of transportation infrastructures. Nondestructive Testing and Evaluation. 2013;**27**(3):253–262.

[12] Malehmir A, Bastani M, Krawczyk CM, Gurk M, Ismail N, Polom U, Persson L. Geophysical assessment and geotechnical investigation of quick-clay landslides—a Swedish case study. Near Surface Geophysics. 2013;**11**(3):341–350.

[13] Timothy S, Bilderback EL, Quigley MC, Nobes DC, Massey CI. Coseismic landsliding during the Mw 7.1 Darfield (Canterbury) earthquake: Implications for paleoseismic studies of landslides. Geomorphology. 2014;**214**:114–127.

[14] Hu Z, Shan W. Landslide investigations in the northwest section of the lesser Khingan range in China using combined HDR and GPR methods. Bulletin of Engineering Geology and the Environment. 2016;**75**:591–603.

[15] Cardarelli E, Marrone C, Orlando L. Evaluation of tunnel stability using integrated geophysical methods. Journal of Applied Geophysics. 2003;**52**(2–3):93–102.

[16] Yamakawa Y, Kosugi K, Masaoka N, Tada Y, Mizuyama T. Use of a combined penetrometer-moisture probe together with geophysical methods to survey hydrological properties of a natural slope. Vadose Zone Journal. 2010;**9**(3):768–779.

[17] Donohue S, Gavin K, Tolooiyan A. Geophysical and geotechnical assessment of a railway embankment failure. Near Surface Geophysics. 2011;**9**(1):33–44.

[18] Sauvin G, Lecomte I, Bazin S, Hansen L, Vanneste M, LHeureux JS. On the integrated use of geophysics for quick-clay mapping: The Hvittingfoss case study, Norway. Journal of Applied Geophysics. 2014;**106**:1–13.

[19] Carpentier S, Konz M, Fischer R, Anagnostopoulos G, Meusburger K, Schoeck K. Geophysical imaging of shallow subsurface topography and its implication for shallow landslide susceptibility in the Urseren Valley, Switzerland. Journal of Applied Geophysics. 2012;**83**:46–56.

[20] Perrone A, Lapenna V, Piscitelli S. Electrical resistivity tomography technique for landslide investigation: A review. Earth-Science Reviews. 2014;**135**:65–82.

[21] Sass O, Bell R, Glade T. Comparison of GPR, 2D-resistivity and traditional techniques for the subsurface exploration of the Oschingen landslide, Swabian Alb (Germany). Geomorphology. 2008;**93**(1):89–103.

[22] Sass O. Bedrock detection and talus thickness assessment in the European Alps using geophysical methods. Journal of Applied Geophysics. 2007;**62**:254–269.

[23] Schrott L, Sass O. Application of field geophysics in geomorphology: Advances and limitations exemplified by case studies. Geomorphology. 2008;**93**:55–73.

[24] Zajc M, Pogacnik Z, Gosar A. Ground penetrating radar and structural geological mapping investigation of karst and tectonic features in flyschoid rocks as geological hazard for exploitation. International Journal of Rock Mechanics and Mining Sciences. 2014;**67**:78–87.

[25] Havenith HB, Jongmans D, Abdrakhmatov K, Trefois P, Delvaux D, Torgoev A. Geophysical investigations of seismically induced surface effects: Case study of a landslide in the Suusamyr valley, Kyrgyzstan. Surveys in Geophysics. 2000;**21**:349–369.

[26] Bichler A, Bobrowsky P, Best M, Douma M, Hunter J, Calvert T, Burns R. Three-dimensional mapping of a landslide using a multi-geophysical approach: The Quesnel Forks landslide. Landslides. 2004;**1**(1):29–40.

[27] Drahor MG, Gokturkler G, Berge MA, Kurtulmus TO. Application of electrical resistivity tomography technique for investigation of landslides: a case from Turkey. Environmental Geology. 2006;**50**(2):147–155.

[28] Rhim CH. Measurements of dielectric constants of soil to develop a landslide prediction system. Smart Structures and Systems. 2011;**7**(4):319–328.

[29] Shan W, Hu Z, Guo Y, Zhang C, Wang C, Jiang H, Liu Y, Xiao J. The impact of climate change on landslides in southeastern of high-latitude permafrost regions of china. Frontiers in Earth Science. 2015;**3**(7):1–11.

[30] Archie GE. The electrical resistivity log as an aid in determining some reservoir characteristics. Transactions of American Institute of Mining Engineers. 1942;**146**(1):54–61.

[31] Waxman MH, Smits LJM. Electrical conductivities in oil-bearing shaly sands. Society of Petroleum Engineers Journal. 1968;**8**(2):107–122.

[32] Zha FS, Liu SY, Du YJ. Study on the electrical resistivity characterization of unsaturated clay. Geotechnical Investigation & Surveying. 2006;**7**:1–4 (in Chinese with English abstract).

[33] Wei S, Yao L, Zhaoguang H, Jitao X. A model for the electrical resistivity of frozen soils and an experimental verification of the model. Cold Regions Science and Technology. 2015;**119**:75–83.

[34] Topp GC, Davis JL, Annan AP. Electromagnetic determination of soil water content: Measurements in coaxial transmission lines. Water Resources Research. 1980;**16**(3): 574–582.

[35] Li L. Study on the characteristics of the electrical resistivity of saline soils [Master's thesis]. Lanzhou, China: Lanzhou University; 2012.

Chapter 4

Measurement of the Electrical Resistivity for Unconventional Structures

Lucian Pîslaru-Dănescu and
Lipan Laurențiu Constantin

Additional information is available at the end of the chapter

http://dx.doi.org/10.5772/67854

Abstract

This study presents an apparatus for the measurement of the electrical volume resistivity of concrete structures in civil and industrial constructions in 2.5 accuracy class, which operates at 500 Hz, for measuring the in situ resistivity of concrete in the range of 5–100 Ωm that is immune to errors due to the polarization phenomena at the interface probe/concrete sample. Also, a quench protection active system (QPS), which works in tandem with a superconducting coil structures (SCSs), in order to prevent the damaging effects when the coil structures pass from the superconducting state into normal conduction state (quench), is presented. An SCS made of YBCO tape high-temperature superconductor (HTS) type, with a critical temperature of 92 K, has been experimented. In order to minimize the heat transfer influx by convection, the SCSs are confined to a cryostat, which is vacuumed at about 0.001 mbar. The working temperature of the HTS coil structures is about 77 K, ensured by liquid nitrogen as cryogenic agent. Finally, the measurement of the electrical resistance of the sensing element (SE) as part of the resistive-type gas sensor is shown. The SE is placed on a Wheatstone bridge. The electrical resistance of the SE is variable by an amount ΔR, on when all the resistances of a Wheatstone bridge are nominally equal.

Keywords: electrical resistivity, reinforced concrete structures, coil structures of superconducting, quench protection, sensing element, gas sensors

1. Measurement of the electrical resistivity of concrete structures

Measurement of the electrical volume resistivity of concrete structures in civil and industrial constructions shows a particular importance in order to establish the status thereof. In practice, often, it counts the problem of investigating the degradation of reinforced concrete that was not provided with electrodes for monitoring. The degradation of reinforced concrete structures

is a complex process concerted and synergy action due to several requests for the nature of the physical (mechanical stress, shock and vibration, weather air/diurnal temperature variations, especially around the freezing temperature of water, etc.), chemical (salinity of the soil and/or of the phreatic water is in contact with the concrete, the content of aggressive atmospheric pollutants, etc.) and microbiological (load microbiological alteration of the exploitation environment). Measurement of the electrical volume resistivity of concrete structures can be achieved by using a quadrupole consisting of the power electrodes, *E*1, *E*2, by means of which *I* [A], the current and the measurement electrodes, *E*3, *E*4, to measure a potential difference, ΔV [V], are injected (**Figures 1** and **2**). An apparent resistivity [1] ρ_{app} [Ωm] is obtained

$$\rho_{app} = \frac{k \times \Delta V}{I} \tag{1}$$

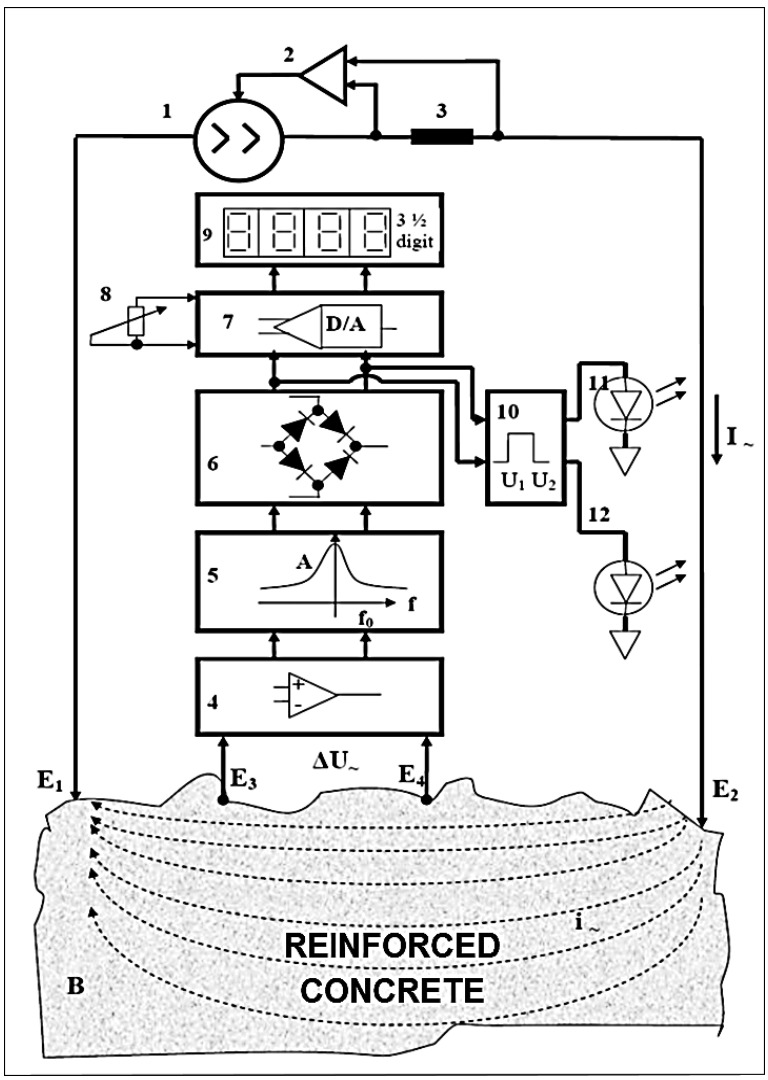

Figure 1. The block diagram of the measurement apparatus of the in situ electrical resistivity of concrete structures.

http://dx.doi.org/10.5772/67854

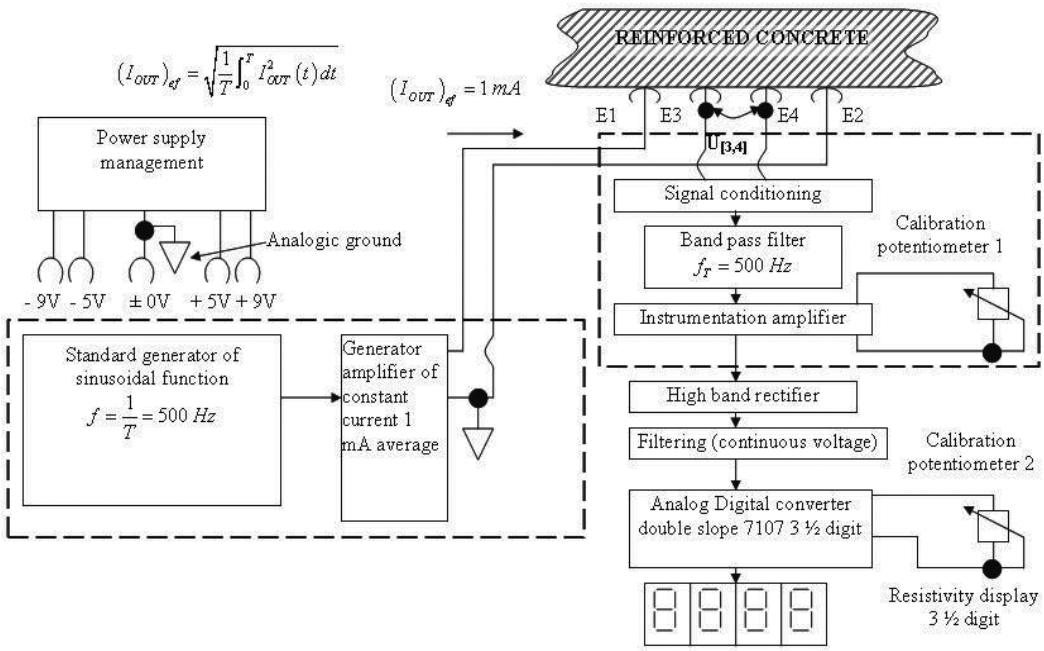

Figure 2. The functional modules of the measurement apparatus of the in situ electrical resistivity of concrete structures [7].

Here, k is a sample-specific geometrical factor and I [A] is the injected current. In this case, the RMS value of the injected current is 1 mA. Based on the technical solutions protected by patent application [2], we prototyped an apparatus for measuring the in situ resistivity of concrete structures.

Measurement apparatus of the in situ electrical resistivity of concrete structures is conceived modularly having as components the following electronic modules, as shown in **Figures 1** and **2**: constant current generator module positions 1, 2 and 3, signal conditioning module position 4, band-pass filter position 5, rectifier module position 6, measurement and display module positions 7–9, and window comparator module positions 10–12 [2–6]. The errors due to electrochemical polarization phenomena are eliminated by powering the current electrodes $E1$, $E2$ with a constant of 1-mA intensity sinusoidal current [6], of 500 ± 5 Hz. The constant current generator module is made by cascading the standard generator sine function sub-module and of constant voltage/current converter sub-module of 1 mA RMS. Accompanying the current flow through the concrete sample, a voltage drop of *approx*. ΔU proportional to the resistivity of concrete, ρ, is recorded at the central contacts of the concrete sample, $E3$ and $E4$.

The measuring probe is of special construction, so as to ensure the parallelism of the electrodes $E1$–$E4$, **Figures 1** and **2** and equal distance between them. The concept of the measuring probe allows easy manoeuvrability in the field, regardless of the orientation of the measuring plane (horizontal, vertical walls and beam-reinforced concrete) and simultaneously uniform pressing of the electrodes and even on surfaces with dislevelments up to 15 mm. In order to ensure as good as possible constant electric contact between

electrodes *E*1–*E*4 and the measured concrete structures surface, they are provided with sponge patches capped by cotton cloth discs (protective bags attached to the electrodes by snap rings). To eliminate the errors due to both AC and DC stray currents, low and high frequency, the signal ΔU at *E*3, *E*4 electrodes is passed through a 'band-pass' filter of 500 ± 10 Hz [3] (with minimum 40-dB attenuation for ±150 Hz).

One of the important electronic modules is the active fourth-order band-pass filter. The band-pass filter is made by cascading a second-order active band-pass Bessel filter with a second-order active band-pass Butterworth filter. Both filters are realized with the use of the Texas Instruments integrated active filters UAF42 [3]. Bessel and Butterworth second-order band-pass filter design was made by using software program FilterPro™ developed by Texas Instruments Company dedicated to developing applications for the integrated circuit UAF42 Texas Instruments—active filter.

With notations required by Texas Instruments, the values of the passive components are obtained from **Table 1** for the second-order Bessel band-pass filter and from **Table 2** for second-order Butterworth band-pass filter, by running the software program FilterPro™.

It can be noted, **Figures 3** and **4**, that the integrated active filter circuit UAF42 [3] contains an operational amplifier unused for filtering function. This is used to achieve signal conditioning, the amplification after filtration, respectively.

The electronic design of the second-order Bessel band-pass filter is shown in **Figure 3**, and the electronic design of the second-order Butterworth band-pass filter is shown in **Figure 4**.

Input voltage of the signal conditioning electronic block is sinusoidal, having amplitude peak to peak in the range of 10–20 mV, recorded at the central contacts of the concrete sample, *E*3 and *E*4, **Figure 2**. This voltage is amplified to the level of 500–1000 mV peak to peak, by using the fourth operational amplifier available into the integrated circuit UAF 42 Texas Instruments—active filter, **Figure 3**, used in the inverting connection. In this case, the gain, as the ratio of the output voltage at this operational amplifier (i.e. from input of the second-order Bessel filter) and the input voltage at the inverting connection of the operational amplifier, **Figure 3**, can be written as

$$A_1 = \frac{V_{OUT1}}{V_{IN1}} = -\frac{R_A}{R_B} = -\frac{100}{2} = -50 \tag{2}$$

f_0 [Hz]	R_{2A} [kΩ]	R_{F1} [kΩ]	R_{F2} [kΩ]	C_{1A}	C_{2A}	R_Q [kΩ]
500	5.49	100	100	–	–	34.8

Table 1. The values of the passive components for the second-order Bessel band-pass filter.

f_0 [Hz]	R_{2A} [kΩ]	R_{F1} [kΩ]	R_{F2} [kΩ]	C_{1A}	C_{2A}	R_Q [kΩ]
500	-	316	316	–	–	4.75

Table 2. The values of the passive components for the second-order Butterworth band-pass filter.

http://dx.doi.org/10.5772/67854

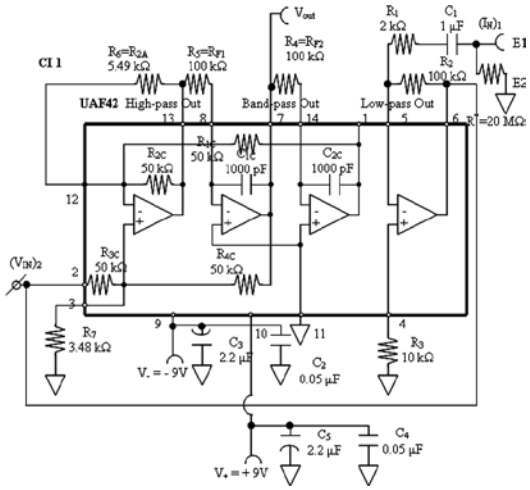

Figure 3. The second-order active band-pass Bessel filter and signal conditioning.

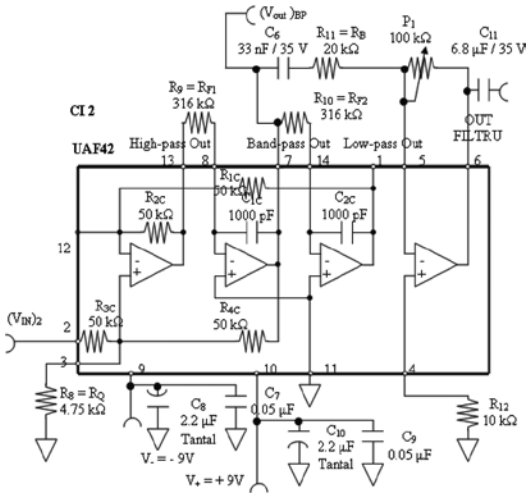

Figure 4. The second-order active band-pass Butterworth filter and instrumentation amplifier.

Input voltage from the second-order active filter Butterworth is sinusoidal, having maximum amplitude peak to peak of 1000 mV. The filter is active, so that the maximum output voltage amplitude is the same, 1000 mV peak to peak. This voltage is amplified to the level of 5000 mV peak to peak by using the fourth operational amplifier available into the integrated circuit UAF 42 Texas Instruments—active filter, **Figure 4**, used in the inverting connection. In this case, the gain, as the ratio of the output voltage at this operational amplifier and the input voltage at the inverting connection of the operational amplifier, **Figure 4**, can be written as

$$A_2 = \frac{V_{OUT2}}{V_{IN2}} = -\frac{P_1}{R_B} = -\frac{100}{20} = -5 \tag{3}$$

Experimentation of the second-order band-pass active filter Bessel was performed as follows:

- at the input of the second-order band-pass active filter Bessel, **Figure 3**, a sinusoidal voltage with a peak-to-peak amplitude of 1000 mV and a frequency range of f = 50–1000 Hz, from the arbitrary function generator FLUKE 281, was applied;
- the output of band-pass filter Bessel is connected to the LeCroy 324 digital oscilloscope channel 1, in order to measure the amplitude of the output voltage;
- by using the entire spectrum of the frequencies, in the range of f = 50–1000 Hz, for the sine wave voltage applied to the input, the characteristic of the second-order band-pass active filter Bessel, **Figure 5**, can be drawn.

Experimentation of the second-order band-pass active filter Butterworth was performed as follows:

- at the input of the second-order band-pass active filter Butterworth, **Figure 4**, a sinusoidal voltage with a peak-to-peak amplitude of 1000 mV and a frequency range of f = 50–1000 Hz, from the arbitrary function generator FLUKE 281, was applied;
- the output of band-pass filter Butterworth is connected to the LeCroy 324 digital oscilloscope channel 2, in order to measure the amplitude of the output voltage;
- by using the entire spectrum of the frequencies, in the range of f = 50–1000 Hz, for the sine wave voltage applied to the input, the characteristic of the second-order band-pass active filter Butterworth, **Figure 6**, can be drawn.

The fourth-order filter, obtained by cascading the two second-order filters, Bessel and Butterworth, was tested in the same conditions. The characteristic of the fourth-order band-pass active filter is shown in **Figure 7**.

In order to eliminate the measurement error due to the polarization phenomena between the reinforced concrete surface (conductor environment of type II) and the electrodes $E1$, $E2$

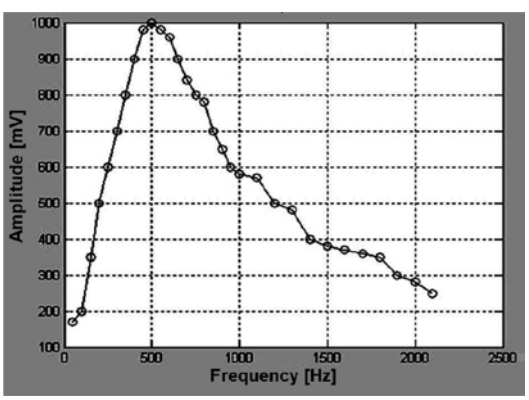

Figure 5. The characteristic of the second-order band-pass active filter Bessel (two poles), test results [7].

http://dx.doi.org/10.5772/67854

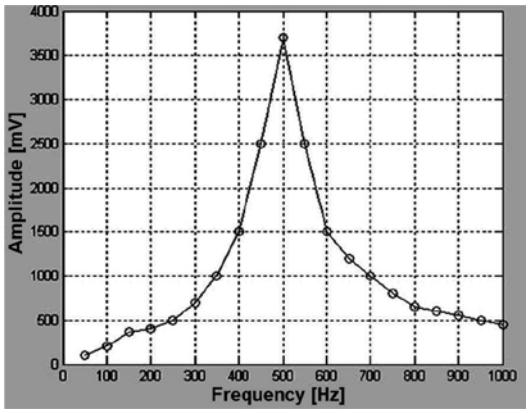

Figure 6. The characteristic of the second-order active band-pass filter Butterworth (two poles), test results [7].

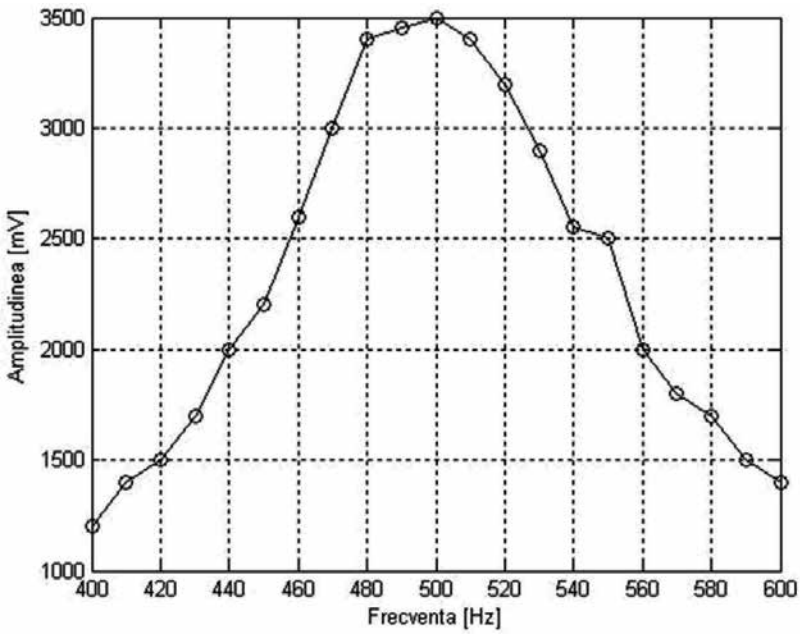

Figure 7. The characteristic of the fourth-order band-pass active filter (four poles), for the frequency of 400–600 Hz, resulted by cascading the two second-order Bessel and Butterworth filters, test results.

(conductor environment of type I), the apparatus includes the current generator module, made by cascading the standard generator sine function sub-module of 500 ± 5 Hz and of constant voltage/current converter sub-module of 1 mA RMS.

In order to eliminate the measurement error due to the potential leakage currents both in DC and in AC, of low and high frequency, and of the interference signals, respectively,

with frequencies below 350 Hz and above 1 kHz, the apparatus includes the fourth-order band-pass active filter made by cascading the two second-order band-pass active filter modules Bessel and Butterworth filters. As I pointed out, the apparatus for the measurement of the electrical volume resistivity of concrete structures in civil and industrial constructions provides the measurements of resistivity in the range of 5–100 Ωm, the 2.5 accuracy class. By using a window comparator electronic module, **Figure 1**, the apparatus allows the optical viewing of the values less than 5 Ωm and over 100 Ωm, through two leads. The apparatus shows the good functional stability, observed during experiments for a wide range of types of concrete structures. Also, the calibration can be done easily by using a potentiometer P1, **Figure 4**.

As concrete structures degrade (through decrease of the alkalinity, carbonation, increase in chloride content, etc.), the resistivity decreases substantially [8]. Today at important buildings, from design phase is provided embedding electrodes that allowing both measuring/monitoring of the concrete resistivity and determination of the potential of corrosion of the reinforcement [9–11].

Experiments were performed in two stages.

Stage 1. Calibration

Standard concrete sample (SCS) for which precisely the electrical resistivity is known, determined by the classical method [12], is measured in order to calibrate the apparatus:

(A1) it is checked using a 'TRUE RMS AC + DC' multimeter set on the mA scale and having probes connected to *E*1 and *E*2 electrodes, respectively, that RMS value of the injected current is to 1 mA;

(B1) the sponge and protective bag for probes (up to saturation) are soaked with a solution of 3–5% NaCl concentration;

(C1) the electrodes *E*1–*E*4 are applied on the SCS sample surface;

(D1) the measurement apparatus of the in situ electrical resistivity of concrete structures is calibrated, through adjusting the amplification of the instrumentation amplifier, by rotating the calibration potentiometer on the front panel, **Figures 1** and **2**, until the apparatus indicates the known resistivity value of the SCS sample.

Stage 2. Measuring the electrical resistivity of concrete structures

(A2) before performing a new measurement, the sponge and the protective bag are soaked again (to saturation) with a solution of 3–5% NaCl concentration;

(B2) the electrodes *E*1–*E*4 are applied on the concrete structure surface;

(C2) the measured value of the electrical resistivity of concrete structures is read on the digital display of 3 1/2 digits.

Figures 8 and **9** present two successive measurements of resistivity of a concrete pillar.

http://dx.doi.org/10.5772/67854

Figure 8. The measurement of a concrete pillar, first measurement.

Figure 9. The measurement of a concrete pillar, second measurement.

2. Protection to quench hazard in high-temperature superconducting coil structures

2.1. The case of a single HTS superconducting coil

The superconducting coil structures can get out of the superconducting state (can normalize), for various reasons, such as the following:

- if temperature exceeds the critical temperature;
- if the injected current growth slope is too steep, after entering the superconducting coil structures in the superconducting state and stabilizing to the temperature regime at a value of 77 K (liquid nitrogen temperature);

- if the injected current through the superconducting coil structures exceeds the critical current;
- if the superconducting coil structures are subjected to mechanical vibrations [13].

Therefore, the superconducting coil structures always work in tandem with a protection system, called quench protection, in order to prevent the damaging effects of their exit from the superconducting state, for the reasons previously described.

This study refers to the quench protection active system (QPS), which works in tandem with a superconducting coil structure. In our case, the superconducting coil structures are made from a tape of material based on YBCO, having a critical temperature of 92 K. Since cooling is made with liquid nitrogen, the working temperature of the superconducting coil structures is in the temperature range of 77 K. The superconducting coil structures are arranged in a cryostat within which a high vacuum of about 0.001 mbar is achieved, in order to minimize the heat transfer to the outside by removing the convective heat transfer. Also, the superconducting coil structures are immersed in liquid nitrogen. **Table 3** presents the electrical resistance of the superconducting coil structures versus the cryostat temperature.

At the critical temperature, the resistance of the coil temperature ensemble is 0.52 Ω (superconducting coil resistance to which the connecting wire resistance and the junction resistance are added). All the connecting wires are made of superconducting material YBCO, HTS type that has a thermal conductivity of ~1 W/mK. The connecting wires are introduced in a sheath of nonmagnetic stainless steel pipe and the terminals are made by copper. Bonding the HTS strip of copper terminals is carried out with a mixture of indium and 5% Ag (to minimize the junction resistance).

Figure 10 presents the variation of the voltage measured on the superconducting coil structures after entering into the superconducting state, depending on the injected current. The

Temperature in the cryostat *T* [K]	**The measured resistance of the superconducting coil *R* [Ω]***
119	0.58
114	0.55
104	0.52
84	0.517
77.6	0.495
77.54	0.465
77.52	0.452
77.51	0.44
77.53	0.434
77.46	0.43

*The superconducting coil structures resistance was measured in the conditions in which no current was injected in the coil.

Table 3. The electrical resistance of the superconducting coil structures versus the cryostat temperature.

http://dx.doi.org/10.5772/67854

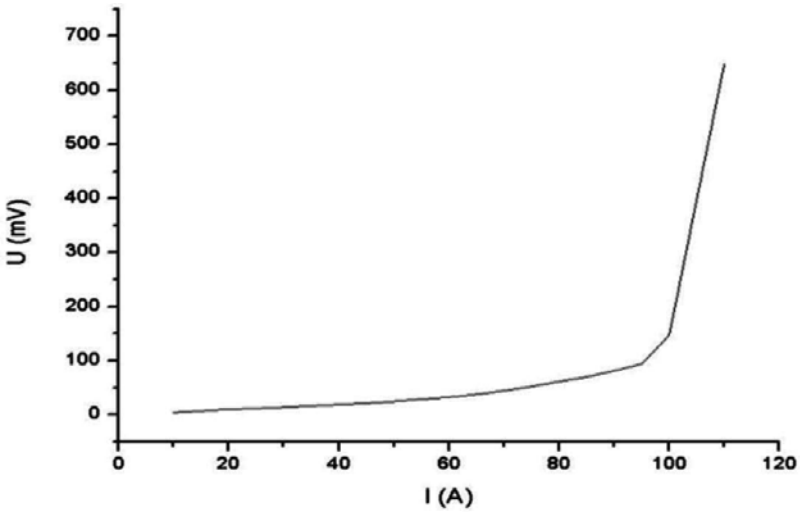

Figure 10. The voltage drop on the superconducting coil structures versus the current, at 77 K [14].

current is injected through the superconducting coil structures, with a slope of 1 A/s [14] by the programmable power supply type AMI 03300PS-430-601. Critical current value is determined from the curve $U = f(I)$, **Figure 10**, by coming down with a tangent at exponential area of the curve. The value of the critical current was determined using this procedure and it is 120 A. The intersection with current axis, **Figure 10**, will give the exact value of critical current of the superconducting coil structures at 77 K. For a current greater than or equal to the critical current, the voltage measured on the superconducting coil structures has a sudden increase. The superconducting coil structures get out of the superconducting state, and the quench protection must act accordingly in order to prevent the damaging effects.

The quench protection system (QPS) is made of two ultrafast switches made with high-power IGBT's transistors (Isolate Gate Bipolar Transistor). The key parameters of the active protection system are as follows:

- The maximum quench detection time is $t_Q = 800$ ns;
- The actual reaction time is in the interval $t_R = 2.78–3.5$ μs;
- The energy is discharged in the range of 1–10 kJ.

A quench active protection system, **Figure 11**, for HTS coil structures must solve the following problems:

1. The detection of the QUENCH.
2. Decoupling the HTS coil structures from the programmable power supply.
3. The coupling of the HTS-type superconducting coil structures on a discharge resistance R_D. In this case, the magnetic energy stored in the coil inductivity L, $W_M = Li^2/2$, is dissipated through Joule effect, $W_J = Ri^2$, by the discharge resistance R_D and the dynamic resistance of the semiconductor device that compose the command power electronic switch.

To comply with its aim, the quench protection active system, **Figures 11** and **27**, must comprise the following parts: ultrafast electronic switches, *T*1 and *T*2 (*K*1 and *K*2, respectively), an electronic circuit for quench detection and a discharge resistance, R_D.

The design of the quench protection system (QPS) is modular, and it comprises the electronic modules presented next.

A. Quench detection and signal processing electronic module. This module, named **1**. on the **Figure 11**, contains the following parts:

- An operational amplifier electronic block with galvanic isolation;
- A precision, differential amplifier electronic block with the common mode rejection factor *CMRR* = 100 dB;
- An amplifier electronic block with the gain *A* = 10 and *CMRR* = 100 dB;
- An electronic block, which performs the module mathematical function;
- An optical interface electronic block, double opto-coupler, with TTL signals recovery;
- A logic sequence programming electronic block.

B. The power electronic module. This module, named **2**. on the **Figure 11**, comprises the following electronic blocks:

- Two drivers electronic blocks IGBT T1/IGBT T2 (Block 1 Driver IGBT T1 and Block 2 Driver IGBT T2);
- An electronic block of ultrafast switches made with the power transistors IGBT T1/IGBT T2;
- A discharge resistance block, R_D.

C. Electronic module of voltage stabilized power supplies. This module, named **3**. on the **Figure 11**, comprises the following blocks:

- The ±12 V_{DC} differential power supply for powering the analogical electronic circuits and the power supply +5 V_{DC} for powering the digital electronic circuits;
- The ±15 and ±12 V_{DC} differential voltage power supply for powering the operational amplifier electronic circuit with optical isolation for the quench signal processing;
- The 2x20 V_{DC} power supply with galvanic isolation for powering the drivers that command the two IGBT power transistors, *T*1 and *T*2.

The discharge resistance R_D, **Figures 11** and **12**, was made from 99.9% pure Cu wire, solenoid shape, having four turns with section Φ = 2 mm, with the wire diameter of *D* = 50 mm, and the value of the DC resistance of R_D = 0.128 Ω. The DC measurement was performed with the Agilent 34461A multimeter.

One of the important electronic modules is the amplifier block with galvanic isolation. Design of the amplifier block with galvanic isolation, **Figure 13**, is made with the integrated circuit

http://dx.doi.org/10.5772/67854

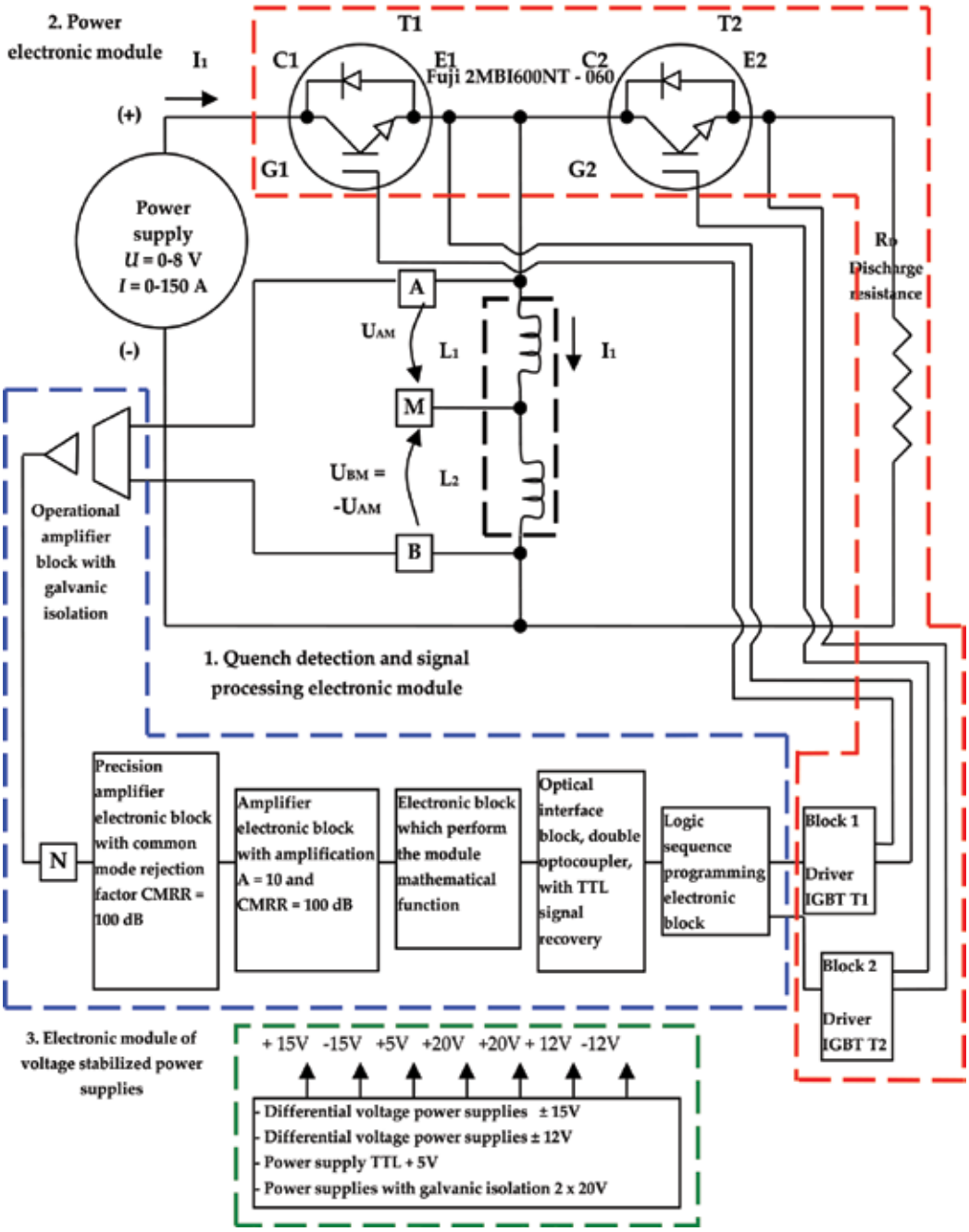

Figure 11. The block diagram of the experimental model of the QPS, which provides the HTS coil structures protection to quench, for the case of a HTS coil [14].

IC1 type ISO 124, Burr Brown manufacturing by Texas Instruments. It is noticed that the useful signal is acquired through a divider, made with four potentiometers *P*1–P4, respectively.

Figure 12. The discharge resistance $R_{D.}$

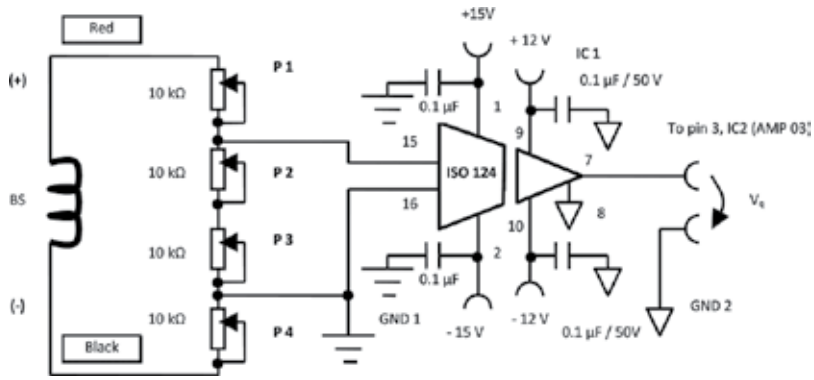

Figure 13. The electronic design of the amplifier block with galvanic isolation [14].

In this way, the dividing factor is adjustable allowing the useful signal threshold setting for which the voltage of the amplifier input is interpreted as quench voltage. Also, it can be seen the separation way of the power supply, **Figure 13**. A differential stabilized power supply of DC voltage of ±15 V_{DC}, which is powering the first part of the amplifier block with galvanic isolation type ISO 124, which acquires the useful signal and a differential stabilized power supply of DC voltage of ± 12 V_{DC}, which is completely galvanic isolation from first is powering the part of the output amplifier.

The power electronic module of the active electronic protection system QPS contains two electronic ultrafast switches made with the power transistors IGBT T1/IGBT T2 type Fuji 2MBI600NT—060, **Figures 14** and **15**, two drivers electronic blocks IGBT T1/IGBT T2, type VLA 517—01R—FUJI [15] **Figures 16** and **17**, and a discharge resistance R_D, **Figures 11** and **12**, with the role of picking the energy stored in a superconducting coil that is composed of two identical sections, serially connected, when at least one of the coils is normalized.

http://dx.doi.org/10.5772/67854

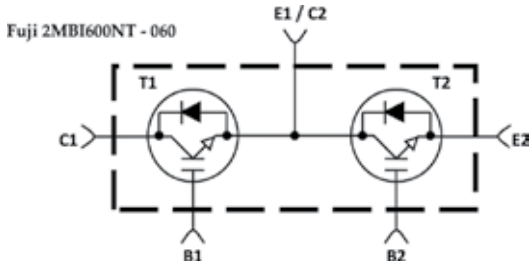

Figure 14. The ultrafast switches block made with the IGBT T1/IGBT T2 [14].

Figure 15. IGBT power transistors, T1/T2 type 2MBI 600 U2 E—060—FUJI [14].

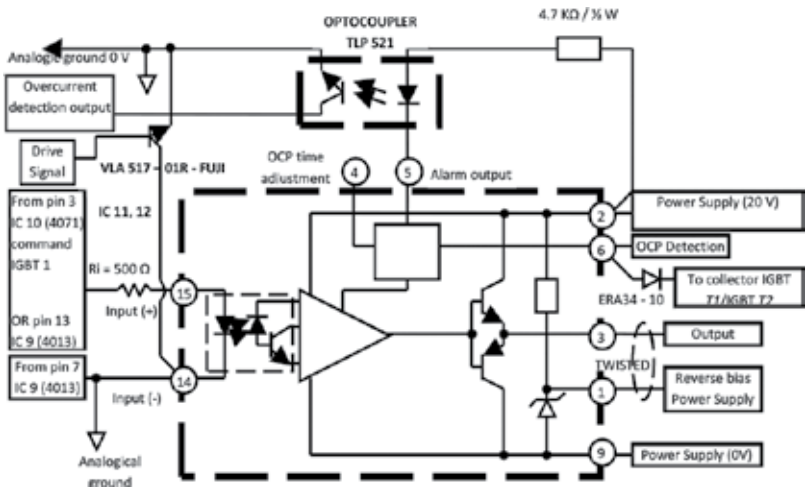

Figure 16. The IGBT T1/IGBT T2 driver block [14].

The first ultrafast switch made with the power transistors IGBT T1, **Figures 11** and **18**, allows the supply of the superconducting coil from the voltage power supply, in normal operation, as well as voltage power supply decoupling when the coil is normalized. The second switch

Figure 17. Hybrid integrated circuit, type VLA 517—01R—FUJI, driver [14].

Figure 18. The power electronic module of the active electronic QPS system, practical design.

made with the power transistors IGBT T2, **Figures 11** and **18**, enables the coupling of the superconducting coil on the discharge resistance R_D, when at least one of the coils $L1$ and $L2$ serially connected is normalized (leaves the superconducting state).

Five possible cases of conduction are distinguished for ultrafast switches made with IGBT power transistors $T1/T2$, according to the conduction state of the two identical sections of superconducting coil $L1$ and $L2$ as follows:

1. Coil inductance $L = L1 + L2$ is in the superconducting state, in which case IGBT power transistor $T1$ is in a state of conduction (ON) and IGBT power transistor $T2$ is found in the locked state (OFF), **Figure 19**;
2. Inductance coil $L1$ was normalized and both IGBT power transistors $T1$ and $T2$ are in a state of conduction (ON) for a period of $t_{M1} = 300$ ns, **Figure 20**;
3. Inductance coil $L1$ was normalized and IGBT power transistor $T1$ is in the locked state (OFF) and IGBT power transistor $T2$ is found in a state of conduction (ON), **Figure 21**;
4. Inductance coil $L2$ was normalized and both IGBT power transistors $T1$ and $T2$ are in a state of conduction (ON) for a period of $t_{M1} = 300$ ns, **Figure 22**;

http://dx.doi.org/10.5772/67854

5. Inductance coil L2 was normalized and IGBT power transistor *T*1 is in the locked state (OFF) and IGBT power transistor *T*2 is found in a state of conduction (ON), **Figure 23**.

The logic sequence programming electronic block, **Figure 11**, performs the following functions:

- Should the coils L_1 and L_2 work in their superconducting state, in which case the IGBT power transistor *T*1 will be in the conducting state (saturated), and the IGBT power transistor *T*2 is in the locked state. In this case, through the superconducting coil $L = L1 + L2$, **Figure 11** flows the current $I1 = 80A$.
- When the quench phenomenon appears, when at least one of the coils *L*1 or *L*2 is normalized, $V_{COMMAND}$ transits from '0' logic to '1' logic. $V_{COMMAND}$ triggers the voltage U_{M1} over a period t_{M1} and both the IGBT transistors *T*1 and *T*2 are conducting, for a period of $t_{M1} = 300$ ns. In the following sequence, **Figures 24–26**, the IGBT power transistor *T*1 will be in the locked state, and the IGBT power transistor *T*2 will be in the conducting state. Note that the U_{Q1} is the command voltage applied onto IGBT *T*1 and the U_{Q2} is the command voltage applied onto IGBT T2. In this way, the superconducting coil $L = L1 + L2$ will be in parallel with the discharge resistance R_D. The magnetic energy accumulated in the superconducting coil $L = L1 + L2$ is dissipated through the protection resistor, discharge resistance R_D. The energy is discharged in the range of 1–10 kJ.

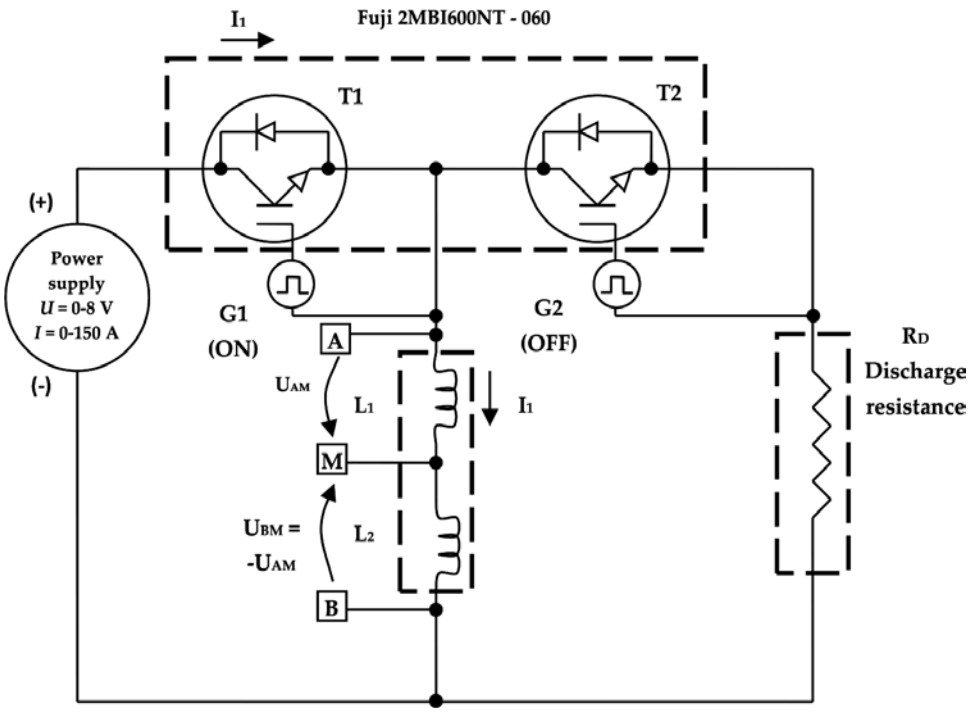

Figure 19. Coil inductance $L = L1 + L2$ is in the superconducting state, in which case IGBT power transistor *T*1 is in a state of conduction (ON) and IGBT power transistor *T*2 is found in the locked state (OFF).

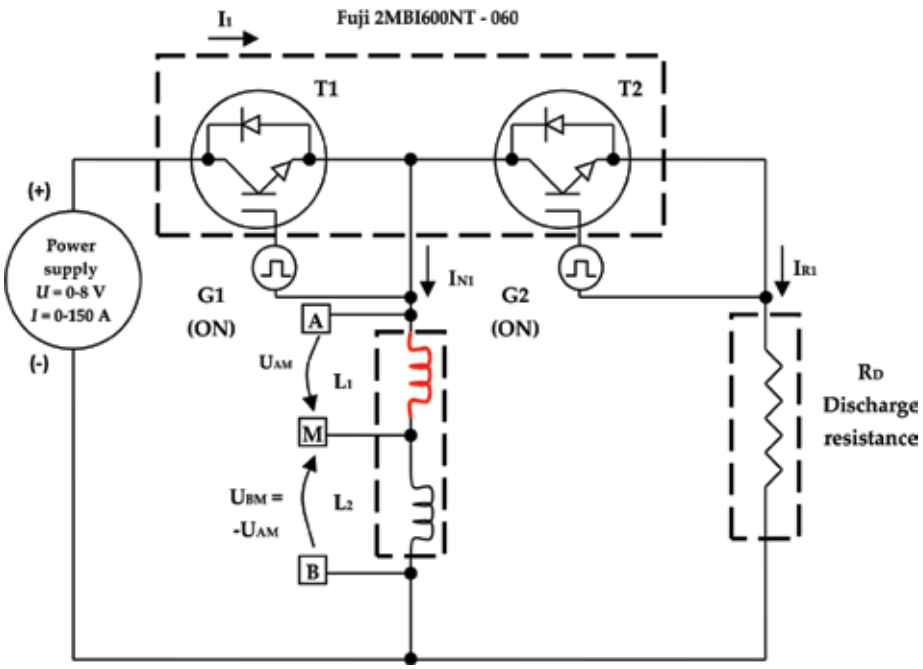

Figure 20. Inductance coil *L*1 was normalized and both IGBT power transistors *T*1 and *T*2 are in a state of conduction (ON) for a period of t_{M1} = 300 ns.

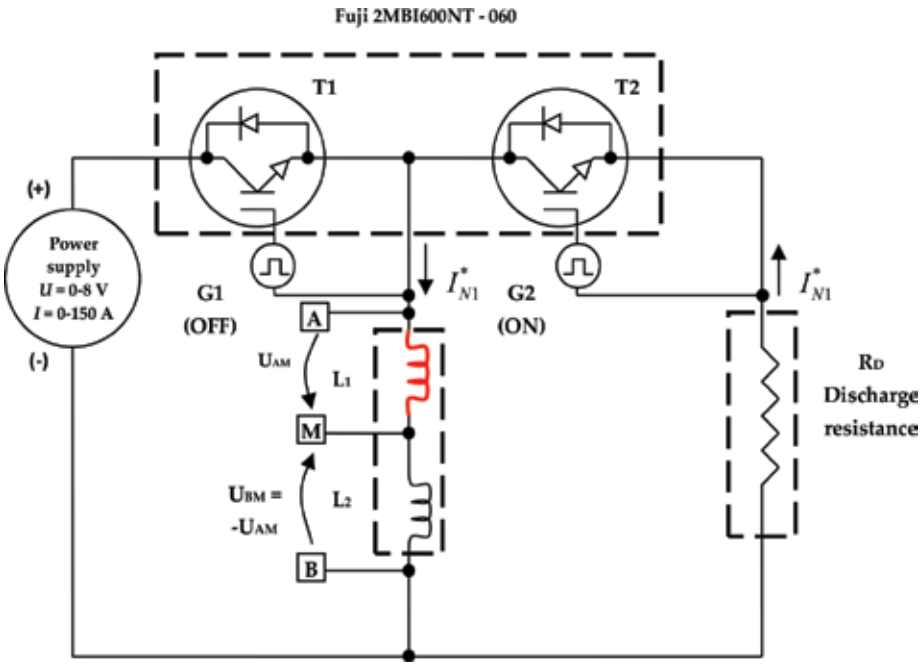

Figure 21. Inductance coil *L*1 was normalized and IGBT power transistor *T*1 is in the locked state (OFF) and IGBT power transistor *T*2 is found in a state of conduction (ON).

http://dx.doi.org/10.5772/67854

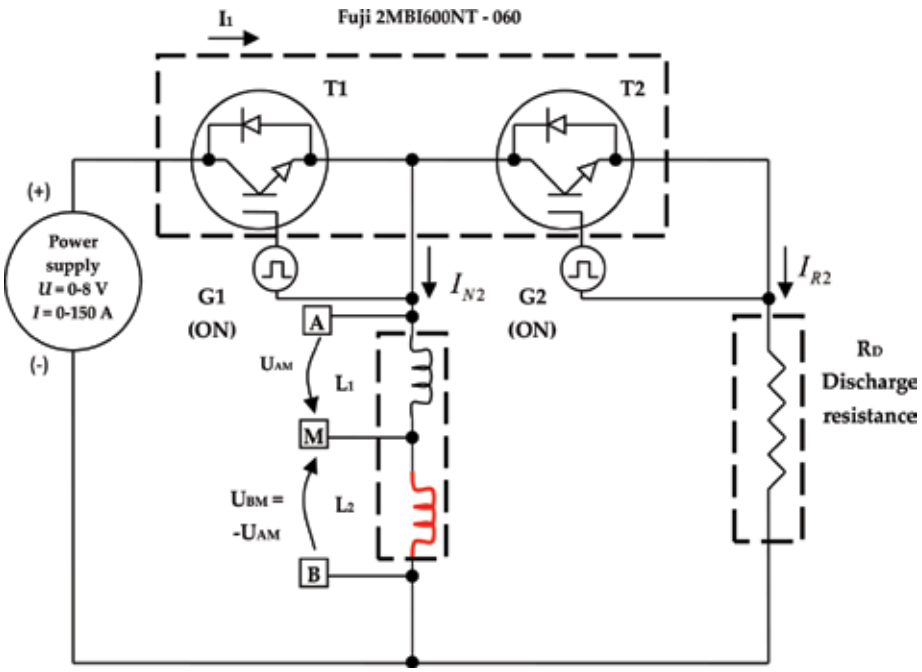

Figure 22. Inductance coil *L*2 was normalized and both IGBT power transistors *T*1 and *T*2 are in a state of conduction (ON) for a period of t_{M1} = 300 ns.

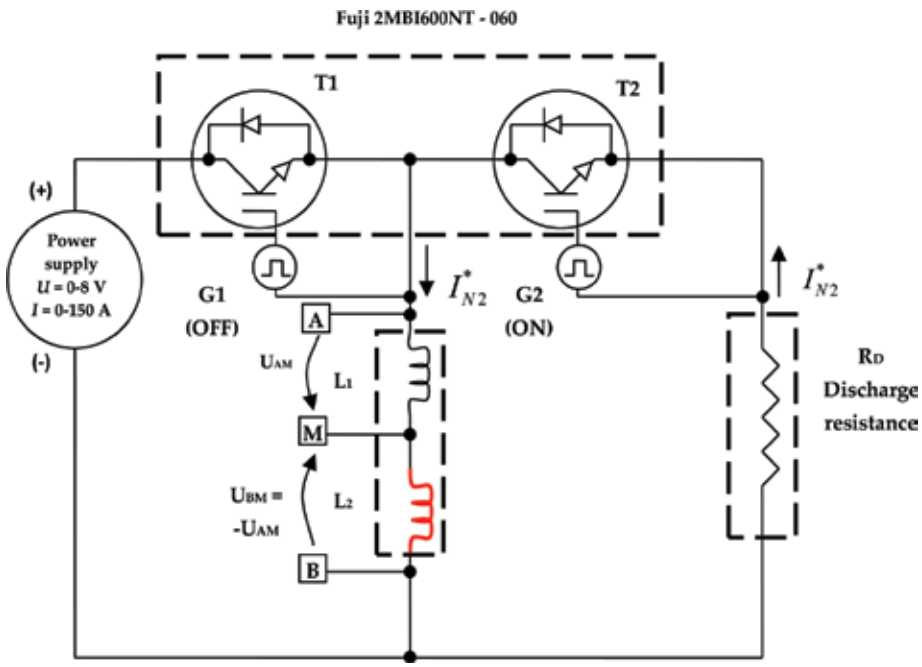

Figure 23. Inductance coil *L*2 was normalized and IGBT power transistor *T*1 is in the locked state (OFF) and IGBT power transistor *T*2 is found in a state of conduction (ON).

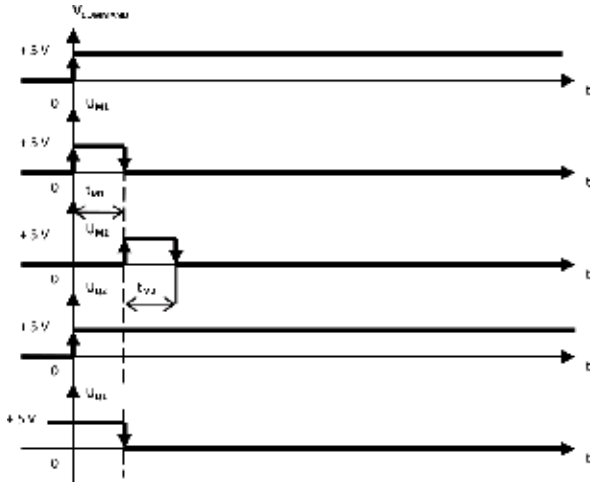

Figure 24. The time command diagram of ultrafast switches IGBT T1/IGBT T2, when the quench phenomenon appears [14].

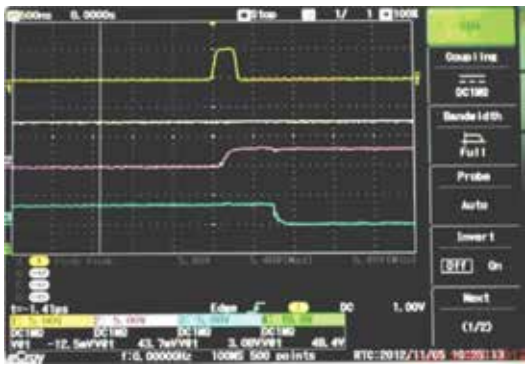

Figure 25. Simultaneous recording of signals U_{M1} (overhead), U_{Q2} (in the middle) and U_{Q1} (on the bottom), for a time base set at 500 ns [14].

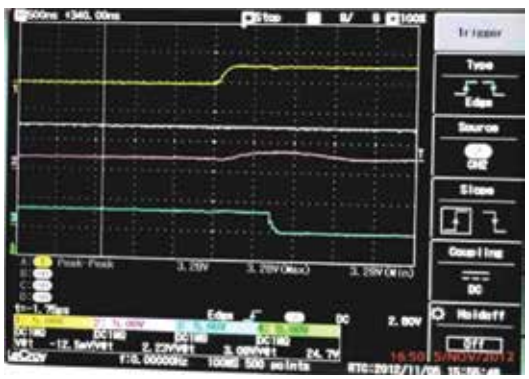

Figure 26. Simultaneous recording of signals $V_{COMMAND}$ (overhead), U_{Q2} (in the middle) and U_{Q1} (on the bottom), for a time base set at 500 ns [14].

http://dx.doi.org/10.5772/67854

From **Figures 25** and/or **26**, the maximum quench detection time of the QPS as t_Q = 800 ns can be determined by assessing transition from logic zero to logic one (positive logic) of the signal U_{Q2} or by assessing transition from logic one to logic zero (positive logic) of the signal $U_{Q1,}$ respectively. The reaction time of the QPS, $t_{R,}$ will take into account and by the actual transition from logic zero to logic one (positive logic), 't_{on}', for both the command driver's and the IGBT's transistors, respectively. Thus, the transition from logic zero to logic one and transition from logic one to logic zero, respectively, for the driver command type VLA 517—01R—FUJI [15], t_{on}-driver = t_{off}-driver = t_{DRIVER} = 1.5 μs.

Also, the transition from logic one to logic zero for high-power IGBT transistor type Fuji 2MBI600NT – 060 t_{off}-IGBT is determined based on the dispersion of such semiconductor device fabrication: $(t_{off}\text{-}IGBT)_{MIN}$ = 0.48 μs and $(t_{off}\text{-}IGBT)_{MAX}$ = 1.20 μs. The reaction time t_R can be calculated as follows:

(a) The minimum reaction time is

$t_{RMIN} = t_Q + t_{DRIVER} + (t_{off} - IGBT)_{MIN}$ = 0.8 μs + 1.5 μs + 0.48 μs = 2.78 μs.

(b) The maximum reaction time is

$t_{RMAX} = t_Q + t_{DRIVER} + (t_{off} - IGBT)_{MAX}$ = 0.8 μs + 1.5 μs + 1.2 μs = 3.5 μs.

The actual detection time lies in the interval t_R = 2.78–3.5 μs.

Advantages of the QPS [16], which provides the HTS coil structures protection to quench, are as follows:

- Makes a quench detection under quench detection time t_0 = 800 ns;
- Makes a decoupling of the power supply, which supplies the superconducting coil through an electronic ultrafast switch, capable of commuting under 1 μs;
- Makes the crossing of the superconducting coil in parallel on a discharge resistance, $R_{D,}$ after the decoupling from the voltage power supply, through an electronic ultrafast switch capable of commuting under 1 μs.

2.2. The case of a variable number of HTS superconducting coils, which may form dipolar, cuadripolare, sextupolare or octupolare structures

Active protection for multipolar set of superconducting coils, whose block diagram is given in **Figure 27**, operates in the following way:

Constructively, a multiple number of 2, the superconducting coils 2–8 multipolar BS1, …, BS8 superconducting coils forming the multipole assembly are connected in series. A multiple number of 2, from 2 to 8 electronic amplifiers with galvanic isolation blocks, equal to the number of superconducting coil assembly previously established, BIG1, BIG2, …, BIG8, having the role of individually conditioning the useful signal originated from each superconducting coil in part, are disposed in parallel with each superconducting coil in part, **Figure 27**. The two ultrafast electronic switches, **Figure 27**, *K*1 and *K*2, respectively,

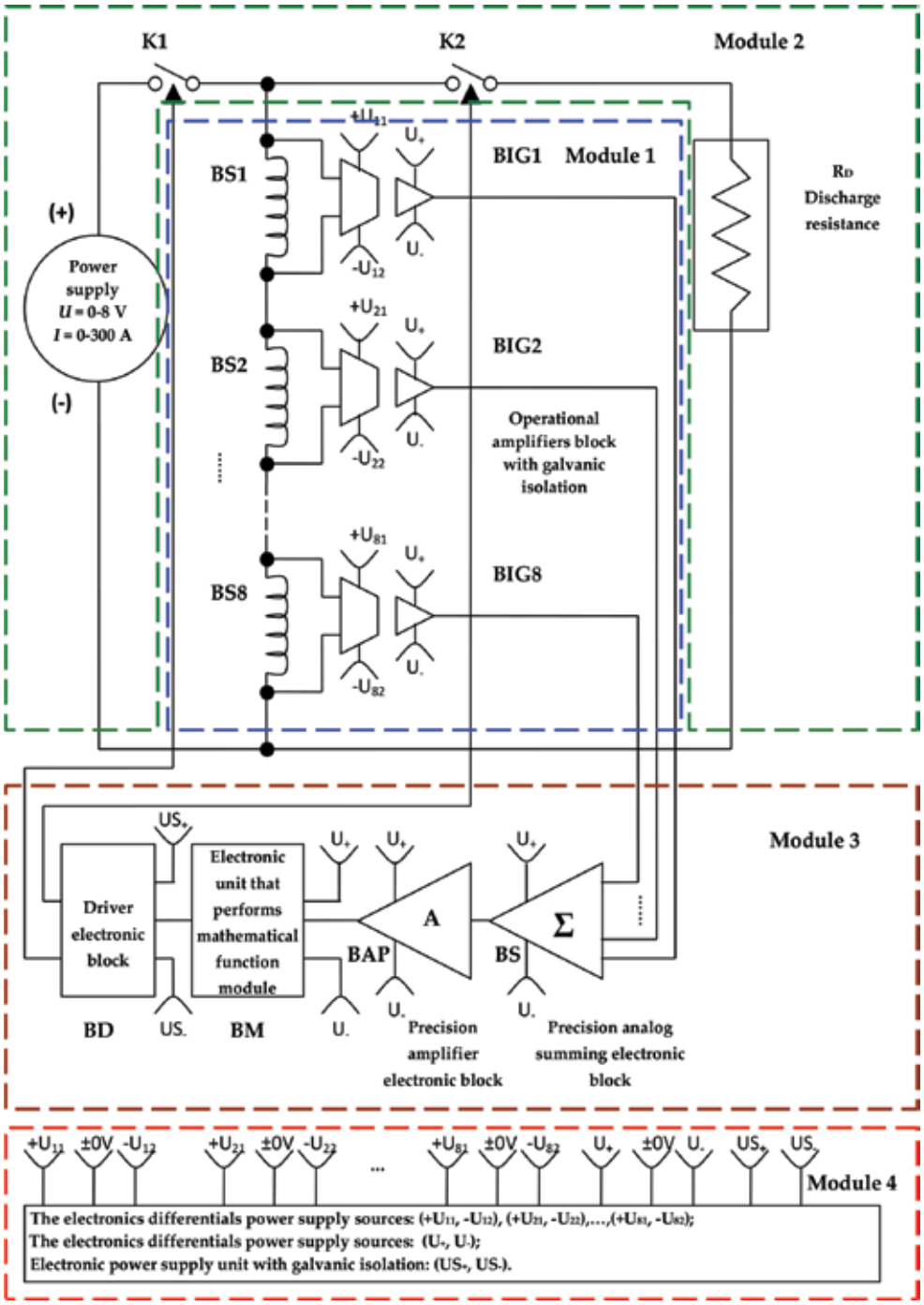

Figure 27. The block diagram of the experimental model of the QPS, which provides the HTS coils structures protection to quench, for the case of a variable number of HTS coils, that may form dipolar, cuadripolare, sextupolare or octupolare structures.

http://dx.doi.org/10.5772/67854

perform connecting and disconnecting the power source voltage and discharge resistance $R_{D,}$ respectively [17].

The first ultrafast electronic switch, *K*1, allows for powering the superconducting multipolar coils BS1, …, BS8 from the power supply voltage, in normal operation, when all the superconducting coils are in a superconducting state. Also, the first ultrafast electronic switch, *K*1, allows power supply decoupling when at least one of the multipolar superconducting coils assemblies BS1, …, BS8 was normalized.

The second ultrafast electronic switch, *K*2, allows coupling of the superconducting coils multipolar BS1, …, BS8 on a discharge resistance, R_D, in the case when at least one of the multipolar superconducting coils assemblies BS1, …, BS8 was normalized. Also, the second ultrafast electronic switch *K*2 allows multipolar superconducting coil BS1, …, BS8 decoupling from discharge resistance, R_D, in normal operation, when all the superconducting coils are in a superconducting state.

One of the important electronic modules is the precision analogue summing circuit, **Figures 27** and **28**. The precision analogue summing circuit is achieved using three analogue-integrated circuits type AMP 03, instrumentation operational amplifier from Analog Devices [18]. Each of these operational amplifiers is used in specific connection of summing [18]. At the exit V_{OUT}, **Figure 28**, we obtain the sum of all four signals that are applied to the inputs IN1, IN2, IN3 and IN4.

The performance of an active electronic protection system (QPS), in both cases A and B, can be evaluated by the visualization and recording of dissipated energy on the discharge resistance R_D, **Figures 11** and **27**, by using the system shown in **Figure 29**. When a high-temperature superconductor (HTS) coil structure that is in a superconductive state is shifting into normal conduction state (quench), the evolution of voltage drop on the superconducting coil structures will be that around the critical current, **Figure 10** and **Table 4**.

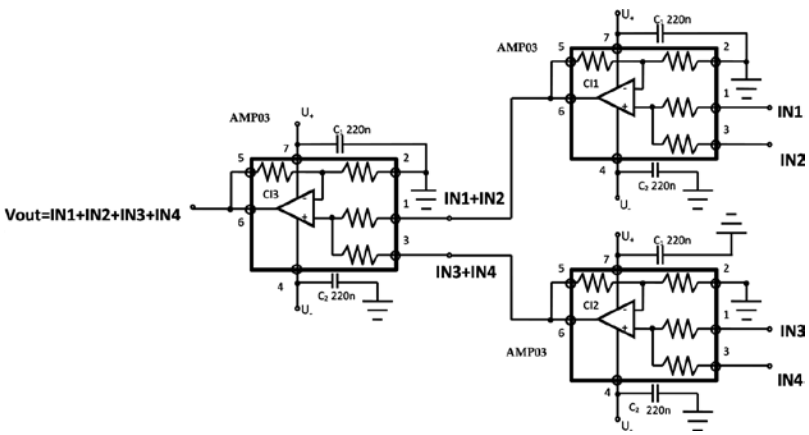

Figure 28. The electronic design of the precision analogue summing circuit, for the case of a HTS coils, cuadripolare structures.

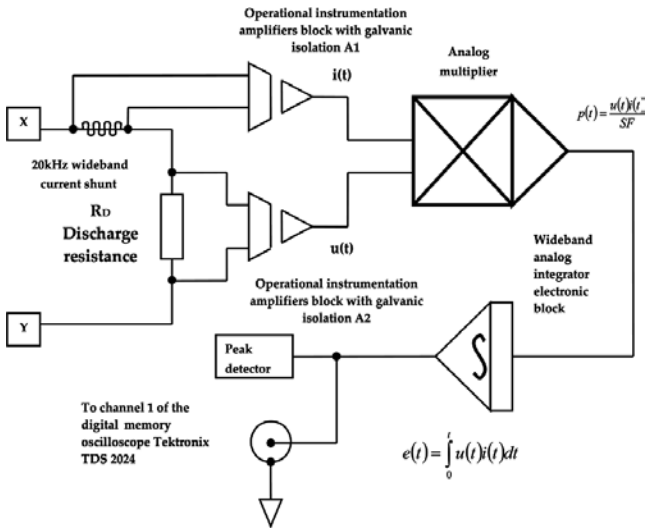

Figure 29. The block diagram of the measurement apparatus, which allows the visualization and recording the dissipated energy on the discharge resistance $R_{D.}$

***I* [A]**	***U* [mV]**
10	3.75
20	10.4
20	9.5
30	14
40	19
45	21
50	24.6
55	28.6
60	32.44
65	37.64
70	44.22
75	52
80	61.4
85	70
90	81.35
95	94
100	147
110	650
120	>650 (Quench)

Table 4. The voltage U picked from the superconducting coil L, versus the injected current I, at 77.46 K temperature.

The QPS will detect a quench situation. By multiplying the instantaneous current $i(t)$ that passes through the discharge resistance R_D with the instantaneous voltage $u(t)$ from the discharge resistance $R_{D,}$ the instantaneous power is obtained, **Figure 29**. The dissipated energy on the discharge resistance R_D is obtained by integrating the instantaneous power.

The YBCO tape high-temperature superconductor, with a critical temperature of 92 K, is used in the construction of superconducting coils tested. The superconducting coil structures are immersed to a cryostat filled with liquid nitrogen as cryogenic agent to decrease the working temperature of the HTS coil structures at about 77 K. Heat transfer by convection is minimized by creating a vacuum at a level of 0.001 mbar.

The experimental results confirm that the quench protection works as expected for the working conditions of the YBCO tape HTS coil structures. **Figure 30** shows the QPS of the superconducting coil during the experiments.

Figure 30. The experimental setup of the quench protection system of the superconducting coil during the experiments (the superconducting coil and the power supply are connected) [14].

3. Measurement of the electrical resistance of the sensing element as part of the resistive type gas sensors

Rare-earth oxides have been extensively explored for several advanced applications, such as in electronics, optics and heterogeneous catalysis, thanks to their peculiar properties arising from the availability of the 4f shell [19]. Ceria, either in its pure form or doped with cations Ca^{2+}, Mg^{2+}, Sc^{2+}, Y^{3+}, Zr^{4+}, potentially has a wide range of applications like gas sensors [20],

oxygen pumps and amperometric oxygen monitors and is adopted in three-way catalysts for reducing the emission of the toxic pollutants (CO, NO*x* and hydrocarbons, etc.) from automobile, owing to its high oxygen storage capacity, associated with its rich oxygen vacancies and low redox potential between Ce^{3+} and Ce^{4+}. CeO_2 doped with rare-earth ions exhibits high oxide ion conductivity at a relatively low temperature (about 600°C) and thus has been applied in solid oxide fuel cells [21, 22]. In case of rare-earth-doped CeO_2, the Y_2O_3 (YDC) system has been studied due its relatively high electrical conductivity and the relative abundance of the yttrium element. The measured electrical conductivity value is 3.0×10^{-3} S/cm at 500°C and 6.0×10^{-2} S/cm at 700°C. If the sensing element is resistance, as components of the gas sensor can range from less than 100 ΩΩto several hundred of kΩ, depending on the sensing element design and the physical environment in which to be measured, you can use two main methods, as follows: measuring resistance indirectly, using a constant current source or measuring resistance using the Wheatstone bridge for which a single element varies.

3.1. Measuring resistance of the sensing element indirectly, by using a constant current source

If the power dissipation through the resistive sensing element is small, a technique for measuring resistance can be used, as shown in **Figure 31**. This technique consists of measuring the voltage output when a constant current is injected through the resistive sensing element, using an accurate means of measuring the voltage and an accurate current source, respectively. Thereby, any change in the current will be interpreted as a resistance change.

3.2. Measuring resistance of the sensing element by using the Wheatstone bridge for which a single element varies

A Wheatstone bridge measures resistance indirectly by comparison with a similar resistance, **Figure 32(a)**. In this case, all the resistances are nominally equal, but one of them (the sensing element) is variable by an amount ΔR. As the equation indicates, **Figure 32(b)**, the relationship between the bridge output and ΔR is not linear. By using an instrumentation operational amplifier, (in-amps) as a Wheatstone bridge amplifier, is performed a better gain accuracy. Usually, this gain accuracy is set with a single resistor, RG and does not unbalance the bridge [23].

Excellent common mode rejection can be achieved with modern in-amps. The excitation voltage V_B is typically 10 V_{CC} stabilized.

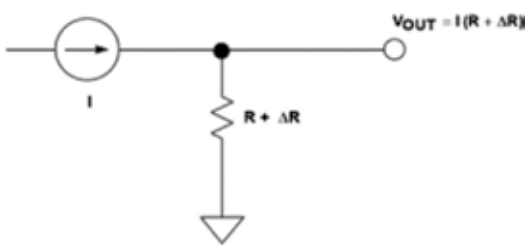

Figure 31. Method of indirect measurement of the resistance, using a constant current source.

http://dx.doi.org/10.5772/67854

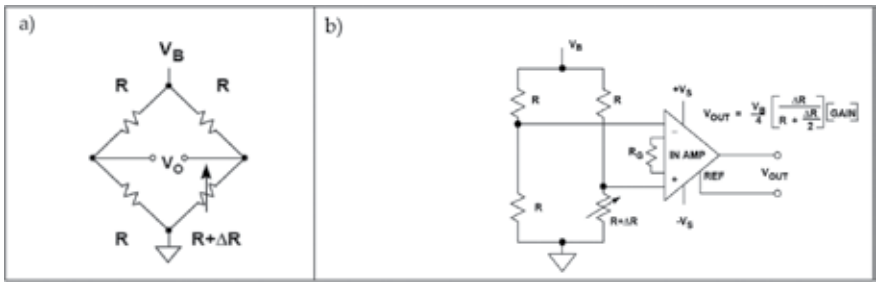

Figure 32. A single-element-varying Wheatstone bridge topology, which uses an instrumentation operational amplifier (in-amps), as a bridge amplifier. (a) A single-element varying Wheatstone bridge. (b) Using an instrumentation operational amplifier as a Wheatstone bridge amplifier.

Author details

Lucian Pîslaru-Dănescu[1]* and Lipan Laurențiu Constantin[2]

*Address all correspondence to: lucian.pislaru@icpe-ca.ro

1 National Institute for Electrical Engineering ICPE-CA, Bucharest, Romania

2 University Politehnica of Bucharest, Bucharest, Romania

References

[1] S. Moreau, M. Bergeron, and R. Clement, "COMSOL Multiphysics modeling for measurement device of electrical resistivity in laboratory test cell", *COMSOL Conference, Boston, October 13–15*, 2011.

[2] I. Lingvay, C. Lingvay, L. Pîslaru-Dănescu, and G. Velciu, "Method and Apparatus for electric resistivity measurement of the reinforced concrete structures", (in Romanian), OSIM, Patent Application *nr. A/00349/2012.*

[3] J. Molina and R. Mark Stitt, Filter Design Program for the UAF 42 Universal Active Filter, *Application Bulletin, Burr-Brown, Texas Instruments*, Tucson, AZ, PO Box 11400, AZ 85734, Street Address: 6730 S, 1993.

[4] Classic Application Notes Collection, *Analog Devices*, One Technology Way, P.O. Box 9106, Norwood, MA 02062-9106, U.S.A., 2008.

[5] ICL7107 3½ Digit LCD/LED Display, A/D Converters, *Data Sheet, Intersil*, 2005.

[6] T. Dănilă and N. Cupcea, *Operational Amplifiers* (in Romanian), Publisher Ed. Teora, Bucuresti, 1994.

[7] L. Pîslaru-Dănescu, A. M. Morega, M. Morega, and V. Stoica, "New concept of measurement apparatus for the in situ electrical resistivity of concrete structures", *8th*

International Symposium on Advanced Topics in Electrical Engineering, ATEE 2013, 23–25 May 2013, Bucharest, Romania, Proceedings of the International Symposium on Advanced Topics in Electrical Engineering (ATEE), 2013. pp. 1–6, Print ISBN: 978-1-4673-5979-5, E-ISBN: 978-1-4673-5980-1, ISSN: 2068-7966, DOI: 10.1109/ATEE.2013.6563531, Accession Number: WOS:000332928500185

[8] A.M. Neville, *Properties of Concrete*, New York: Wiley & Sons, 4th Edition, 1996, ISBN 0470235276.

[9] H. Arup and O. Klinghoffer, "Junction potentials at a concrete/electrolyte interface", in *Proceedings of EUROCORR'97, Sept. 22–25, Trondheim, Norway*, 1997, vol. I, pp. 455–459.

[10] R. Myrdal, "Phenomena that disturb the measurement of potentials in concrete", in *Proceedings of Corrosion/96, paper No 339, NACE, Houston, TX*, 1996.

[11] R. Myrdal, "Potential gradients in concrete caused by charge separations in a complex electrolyte", in *Proceedings of Corrosion/97, paper No 278, NACE, Houston, TX*, 1997.

[12] T.K. Simon and V. Vass, "The electrical resistivity of concrete", Concr. Struct., 13, 2012; 61–64.

[13] Y. Yang, B. Wei, P. Chen, H. Zhang, et al., "The quench protection system for superconducting magnetic energy storage", IEEE Trans. App. Supercon., 2013; **23**: 3, DOI:10.1109/TASC.2012.2233855.

[14] L. Pîslaru-Dănescu, A. M. Morega, V. Stoica, M. Morega, and I. Dobrin, "A new electronic active system for protection to quench hazard in high temperature superconducting coils", *9th International Symposium on Advanced Topics in Electrical Engineering ATEE 2015, 7–9 May 2015, Bucharest, Romania, Proceedings of the International Symposium on Advanced Topics in Electrical Engineering (ATEE)*, 2015, pp. 692–697, ISBN: 978-1-4799-7514-3, ISSN: 2068-7966, DOI: 10.1109/ATEE.2015.7133889

[15] FUJI **VLA 517 – 01R,** *Application Manual*, Fuji Electric Co., Ltd., Electronics Group, Tokyo, Japan, 1997.

[16] L. Pîslaru-Dănescu, I. Dobrin, V. Stoica, L. C. Lipan, and I. Pisica, "Apparatus for active protection for superconducting coil at superconducting motors", (in Romanian), OSIM, Patent *nr.* 128881/2011.

[17] L. Pîslaru-Dănescu and I. Dobrin, "Active protection for superconducting multipolar coils assembly", (in Romanian), OSIM, Patent *nr. A/01004/29.11.2012.*

[18] Analog Devices, "*Precision, unity-gain differential amplifier*, *AMP 03*", Data Sheet, 2003, Rev. F., Norwood, MA, USA.

[19] L. Liao, H. X. Mai, Q. Yuan, H. B. Lu, J. C.Li, C. Liu, C.H. Yan, Z. X. Shen, and T. Yu,"Single CeO_2 nanowire gas sensor supported with Pt nanocrystals: gas sensitivity, surface bond states and chemical mechanism", J. Phys. Chem. C, 2008; **112:** 9061–9065.

[20] J. G. Li, T. Ikegami, J. H. Lee, and T. Mori, "Characterization and sintering of nanocrystalline CeO_2 powders synthesized by a mimic alkoxide method", Acta Mater., 2001; **49**: 419–426.

[21] H.-J. Choi, J. Moon, and H.-B. Shim, "Preparation of nanocrystalline CeO_2 by the precipitation method and its improved methane oxidation activity", J. Am. Ceram. Soc., 2006; **89(1)**: 343–345.

[22] J-H. Lee, J. Kim, S.W. Kim, HW. Lee, and H.S. Song, "Characterization of the electrical properties of Y_2O_3-doped CeO_2 rich CeO_2-ZrO_2 solid solutions", Solid State Ionics, 2004; **166**: 45–52.

[23] W. G. Jung, "*Operational Amplifier Application Hndbook*", Newnes, An imprint of Elsevier 30 Corporate Drive, Suite 400, Burlington, MA 01803, USA Linacre House, Jordan Hill, Oxford OX2 8DP, UK, 2005 by Analog Devices Inc., ISBN 0-7506-7844-5.

Chapter 5

Estimation of Hydrological Parameters from Geoelectrical Measurements

Héctor José Peinado Guevara,
Jaime Herrera Barrientos, Omar Delgado Rodríguez,
Víctor Manuel Peinado Guevara,
Omar Llanes Cárdenas and
María Ladrón De Guevara Torres

Additional information is available at the end of the chapter

http://dx.doi.org/10.5772/67990

Abstract

In the coastal aquifer of the lowlands on the right side of the river Sinaloa there is need for fresh water for agricultural development since, around 15% of the water used in agricultural irrigation, is from underground sources. This situation is exacerbated in periods of drought, which promotes drilling with the risk of finding brackish water in them; besides, there is the risk of not meeting water demand due to low hydraulic transmissivity (T) of the aquifer, putting at risk the drilling costs that this implies. In this sense, the determination of T and K (hydraulic conductivity) is important for the development and management of groundwater exploitation of the study area. Generally by means of pumping tests in wells, T is obtained, with high costs, so there are few values of T. K is generally obtained by wells and laboratory test. The aim of this chapter is to establish an empirical relationship between T and K with Dar-Zarrouk parameter in porous media, transverse resistance (T_R), in addition to a characterization of the water quality through the electrical resistivity. This parameter is estimated from surface resistivity measurements, which are more economical in relation to the pumping tests; thus, T was characterized in the study area. The coefficient of correlation of the exponential adjustment is 0.79 and the relation is $T = 137185.7\ T_R^{0.020758} - 156691$ and $K = 367.21^{0.0548} - 518.813$ with coefficient of correlation of 0.678.

Keywords: electrical resistivity, water quality, transverse resistance, hydraulic transmissivity, hydraulic conductivity

1. Introduction

Groundwater of the coastal aquifer in the lowlands of the right side of the Sinaloa River constitutes an important support element for the development of agricultural activity in the region, especially during periods of drought. In order to extract groundwater, it is necessary to perform perforations, whose costs are high. In addition to the high cost is the uncertainty of finding fresh water, so it is desirable to have a preliminary characterization of the quality of groundwater, as well as the hydraulic property, which defines the aquifer water production. Hydraulic transmissivity (T) determines the flow of groundwater that is transmitted through a vertical strip of aquifer-wide unit under a hydraulic gradient unit. This parameter is required in numerical flow modeling processes [1, 2]; recharge tests; and in the determination of the radius of influence of a well for the determination of the perimeters of protection to the contamination of well water, among others. It is useful to estimate the resource groundwater and its integral management [3] through pumping tests, which generally are scarce due to high costs; therefore, the power to determine it through geoelectric parameters such as the resistivity of the aquifer formation, obtained through a vertical electrical sounding [4] is of interest, since this is a non-destructive, economical method and no drilling is required for its realization. The hydraulic limitations presented by the aquifers are directly related to the permeability and thickness that each sequence of the sedimentary cover can develop [5]. The physical analogy between hydraulic and electric flow has been a motivation to study for several authors [2, 3, 6–12] who present relations between electrical and hydraulic parameters of an aquifer. Nourbehect [13] presents a general theoretical approach on the coupling between various flows of fluids of nature through a functional relation, which allows to establish that there are relations between electrical and hydraulic parameters. In this work, we are experimenting in the search for exponential relations between R_o and R_w; T and K with the electric transverse resistance. The transverse resistance is one of the Dar-Zarrouk parameters and has been proved to be useful in the evaluation of hydraulic conductivity and transmissivity [14–20]. In a flat and stratified earth model, each geoelectric layer is characterized by a thickness h and an electrical resistivity ρ. These parameters allow obtaining the parameter of Dar-Zarrouk, the electric transversal resistance (T_R), which, for a layered medium of n layers, in each layer is defined as:

$$T_R = h\rho \tag{1}$$

Niwas and Singhal [21] found analytic relationship between the parameters of Dar-Zarrouk and T as:

$T = (K\sigma)T_R$ and assuming that the product $K\sigma$ remains unchanged in areas with similar geological setting and water quality $T = CT_R$. By knowing the value of this constant C, the T and K can be calculated by knowing T_R.

Ponzini et al. [8] found an empirical function between the transversal electrical resistance of an aquifer with its T. The shape of the relation between aquifer properties and geophysical parameters can be linear or non-linear [16]. The empirical function found is of the potential type of the form $TR = AT^M + B$, where T_R is transversal resistance, T the hydraulic transmissivity, and

http://dx.doi.org/10.5772/67990

the terms *A, M*, and *B* are constant. Soupios et al. [22] found relations between electrical cross-resistance and hydraulic transmissivity with an expression of the form proposed by Ponzini et al. [8]. Perdomo et al. [23] established a relation of the form $T = A.TR^M$. On the other hand, Kazakis et al. [12] obtained linear relations between the K and the resistivity of the aquifer. Some authors have found a linear relationship between T and T_R [16–19]. The works of these authors suggest that there is a relation between the transmissivity of an aquifer and the parameter of Dar-Zarouk, also that this relation is influenced by the geo-hydrological conditions of the place and maintains an exponential relation. Under these circumstances and taking into account that T, T_R, and electrical resistivity can be obtained from surface measurements of electrical resistivity in combination with pumping tests, it is possible to find relations for the study area.

2. Materials and methods

2.1. Description of the study area

The study area is located between the coordinates 25°16′50″ and 25°41′13″ north latitude and 108°24′51″ to 108°41′22″ west longitude (see **Figure 1**). The climate is dry, very warm, and warm with rains in summer. The average annual precipitation is 300–400 mm (1986–2013) [24]. The average annual temperature is 22–24°C for the 1986–2013 series [24]. Soils are of alluvial origin,

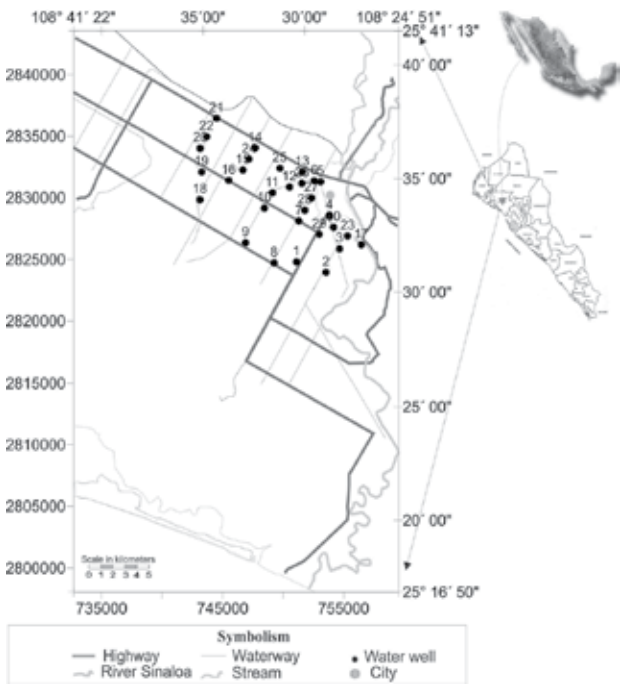

Figure 1. Localization of the study area.

Cenozoic era, quaternary period, predominating soils Vertisol (62.55%), Solonchak (21.72%), Cambisol (3.17%), Kastañozem (2.58%), Regosol (2.13%), Phaeozem (1.52%), Arenosol (1.24%), Fluvisol (0.92%), and Leptosol (0.56%) [25].

The topographical relief is smooth, has a gradient that goes from 0.5 to 1 m per kilometer in a northeasterly direction (**Figure 2**). This was obtained from the heights of the ledge of the wells.

2.2. Wells information

Thirty wells were analyzed with a depth between 100 and 150 m, which were built by the National Water Commission. The wells are geotagged with a portable GPS brand Magellans. Water samples were obtained from each well; for this the wells in operation were sought, and groundwater electrical conductivity was measured *in situ*. Each of the wells counts with information of pumping tests at constant flow rate and steady state in recovery, lithologic columns, and well construction design. With the information of the pumping tests, T was obtained by the Theis method [26].

The interpretation of the pumping tests indicated that 3.3% of the T values are comprised in medium high, 6.7% in high, and 90% in very high according to the classification of Villanueva and Iglesias [26].

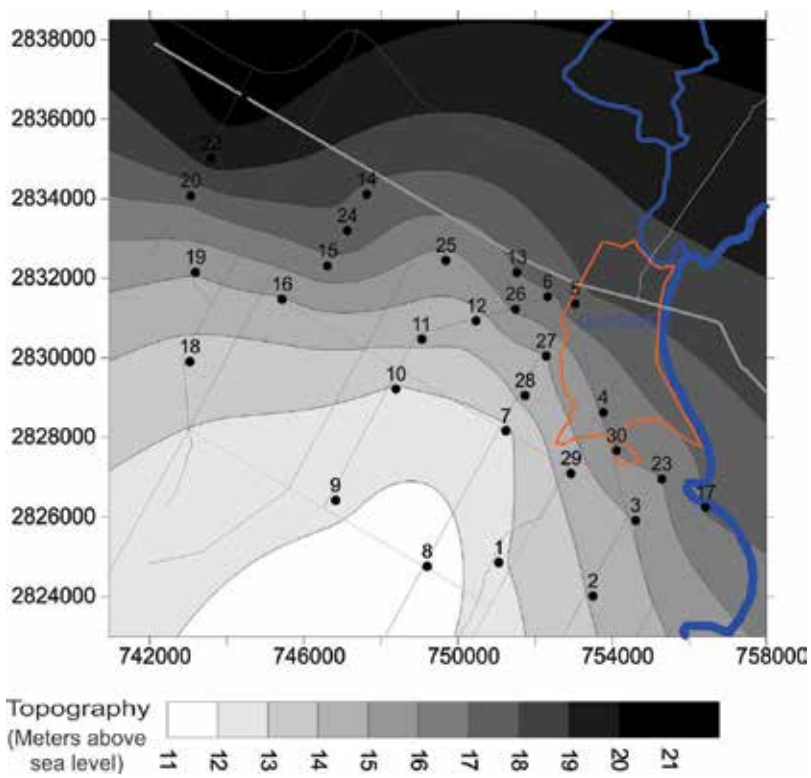

Figure 2. Topographic relief of the study area.

http://dx.doi.org/10.5772/67990

The Theis method presupposes that the well crosses the whole aquifer. In this case, the correction was not made, because at the moment, neither with geophysics nor with the columns of the wells, the total thickness of the aquifer is known. On the other hand, the impact of the lack of correction is insignificant, since the observed descents are less than 15% of the total saturated thickness, that is, the thickness is greater than 150 m and the observed descent is less than 10 m; thus, according to [26] it is not necessary to make the correction to Dupuit when the descents are inferior to 15 by 100 of the initial saturated thickness, H_0.

2.3. Aquifer geometry

With the information of the 30 lithological columns of wells, the geometry of the aquifer of the study area was determined. **Figure 3** shows a section with the sequence of materials where an abundance of gravel with silty clay matrix, standing out in the presence of a body of gravel is seen. The lithological columns of the wells that have depths between 100 and 150 m do not show a geological or hydrogeological basement.

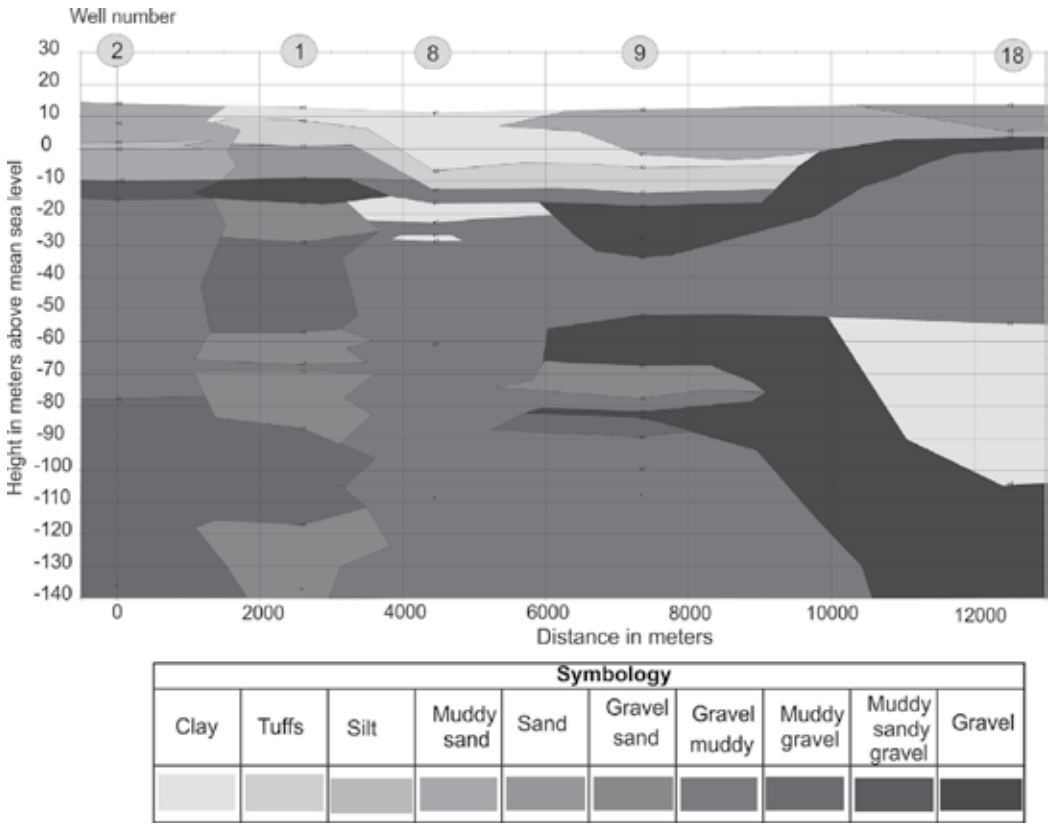

Figure 3. Section perpendicular to the Sinaloa River.

2.4. Vertical electrical soundings

Fourteen wells were selected from 30 wells. In these, a vertical electrical survey was carried out, having them as the center of the sounding. The Schlumberger array was used with a maximum current electrode separation of 500 m the soundings were interpreted by direct modeling using the Guptasarma algorithm [27].

2.5. Relation between R_w and R_o

With the modeling of the vertical electrical sounding, the resistivity (R_o) of the saturated thickness of the formation is obtained. R_w value is obtained from the field measurement of well water samples in pumping. From the different values of R_o and R_w by minimum squares adjustments, the constants A and B of the linear relation are obtained:

$$R_W = A\,R_O + B \tag{2}$$

3. List of hydrological parameters (T and K) with geoelectric measurements and pumping tests

With information from true resistivity (R_o) of each layer and its thickness (h) T_R was obtained, which was related to T and K from the exponential expressions of the form:

$$T = A\,.\,T\,R^M + B \tag{3}$$

$$K = A\,.\,T\,R^M + B \tag{4}$$

Where T is the hydraulic transmissivity, K is the hydraulic conductivity, T_R is the transverse resistance, and A, M and B are constants obtained by minimum squares adjustment.

4. Results and discussion

4.1. Geoelectric sounding

Figure 4 shows the result of the VES performed in wells 1 and 10. For the modeling of the VES data, the available information of the lithological columns, static level of the water, and its salinity was considered. Experimental data and their corresponding models, as well as the root-mean-square (RMS) error of each adjustment are presented. The lithological relationship with electric resistivity allows delimiting the aquifer area, characterized by predominantly low clayey materials. In the case of well 1, the electrical resistivity was 13.04 Ω-m, and in the case of well 10, it varied from 9 to 29 Ω-m. The presence of materials with clay wells favors the $T - T_R$ ratio [10].

http://dx.doi.org/10.5772/67990

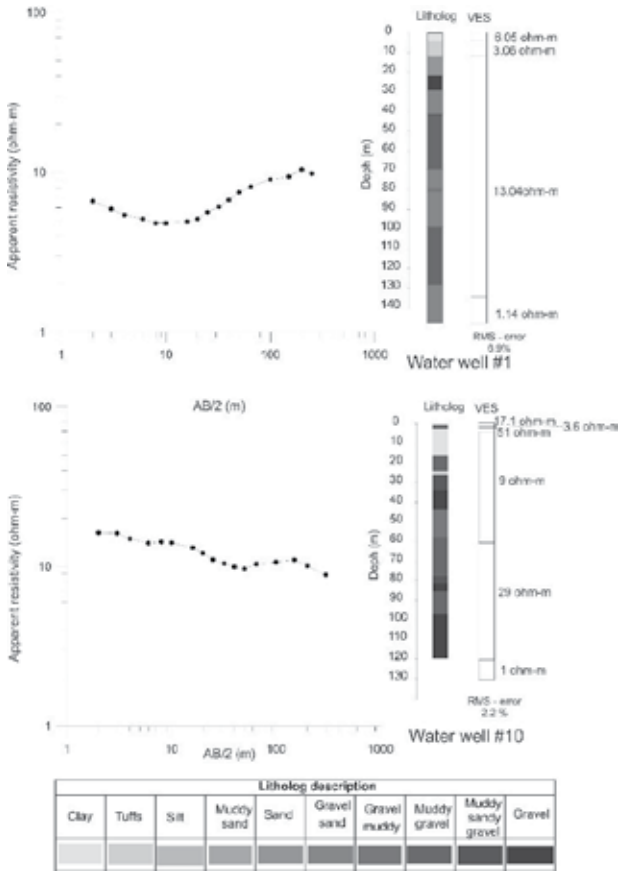

Figure 4. VES experimental data with their respective interpreted model compared with lithological column.

4.2. Water quality

Some authors [11, 28–30] have successfully applied the Archie's law to hydrogeology studies. **Figure 5** shows the fit for 14 pairs of $R_w - R_o$ values that illustrate a linear function directly proportional connecting the groundwater resistivity (R_w) and the saturated layer resistivity (R_o); as the pore water resistivity increases, the formation resistivity increases as well. The constants A and B are 1.014091 and −2.316, respectively. The correlation factor resulting from the adjustment is 0.90, therefore

$$R_w = 1.014\, R_o - 2.316 \tag{5}$$

The practical meaning of this relation is that, if it is desired to perform a perforation in the study area, it is possible to perform a vertical electrical sounding prior to drilling; its interpretation can be determined by R_o, which when placed in the above expression enables a priori

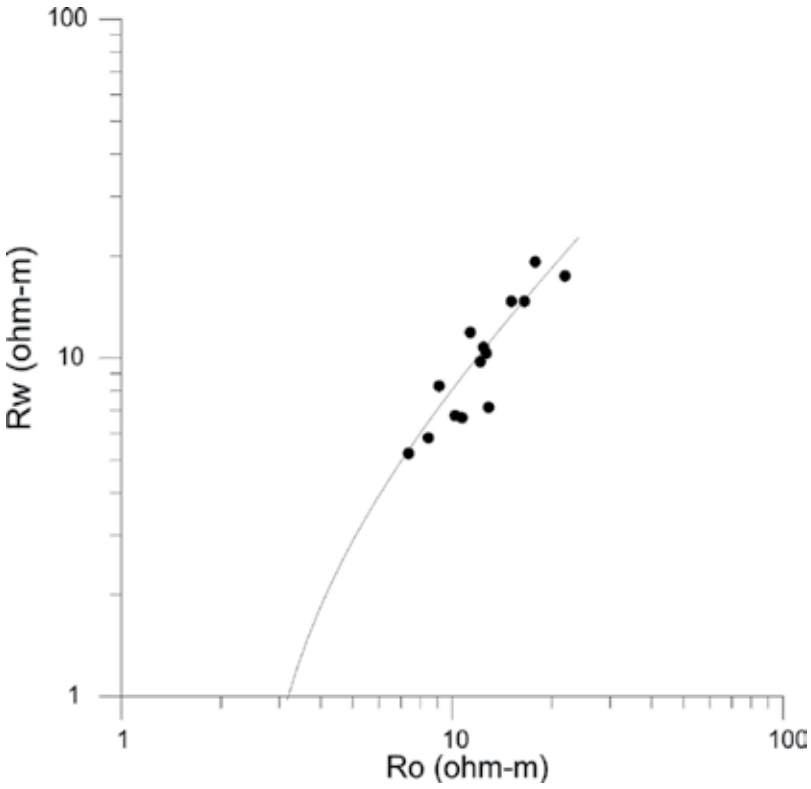

Figure 5. Bulk resistivity versus aquifer resistivity.

value, R_w. Electrical conductivity (EC) of water is inversely proportional to the electrical resistivity and is determined by the expression

$$\text{EC} = \frac{10}{R_w} \tag{6}$$

With the value of the EC and considering the relationship between EC and total dissolved solids (TDS), salinity can be obtained by the expression [31]

$$\text{TDS} = \frac{1000\text{EC}}{1.65} \tag{7}$$

With the value of TDS, the type of water expected can already be determined [32]. From the interpretation of the VESs, it was found that the resistivity of the aquifer formation R_o varies between 7.4 and 21.9 Ω-m, for its part, the water of the formation presented a resistivity that oscillated between 5.2 and 19.2 Ω-m (see **Table 1**). Value of R_o is 10 Ω-m and R_w is 7.825 Ω-m. This value corresponds to 774 ppm of TDS (salinity); thus, it is fresh water according to the classification of Heath [32]

4.3. The relationship between *T* and T_R

From R_o and aquifer thickness (*h*) values, T_R was determined. **Table 1** shows the T_R values for 14 wells and their respective *T* and *K* values. **Figure 6** shows that T_R and *T* have a relationship

http://dx.doi.org/10.5772/67990

Well number	Well depth	Porewater resistivity (R_w, Ω-m)	Hydraulic transmissivity (m^2/day)	Hydraulic conductivity (m/day)	Computed parameters—VES interpretation		
					h (m)	R_o resistivity (Ω-m)	*TR* transverse resistance (Ω m^2)
1	150	10.3	3410.3	25.8	132.2	12.7	1676.3
2	150	14.7	2925.4	22.5	130.3	15.1	1965.2
3	120	19.2	1588.2	22.7	70.0	17.8	1246.6
6	150	10.8	3157.8	35.3	89.5	12.4	1111.3
7	134	6.7	3116.2	31.3	99.7	10.7	1066.8
10	120	17.5	4294.6	47.8	89.8	21.9	1968.1
11	121	14.7	2354.1	30.7	76.7	16.5	1266.3
13	120	11.9	1694.8	17.7	95.9	11.3	1088.1
19	120	8.3	452.4	4.8	94.9	9.1	865.0
20	150	5.8	1675.7	14.7	113.6	8.5	962.0
21	150	5.2	987.4	7.8	126.5	7.4	932.4
22	120	6.8	715.5	8.3	86.0	10.2	876.0
28	122	7.2	3139.2	31.9	98.4	12.9	1265.5
29	120	9.8	2063.2	21.5	95.8	12.2	1164.4

Table 1. Data used and interpreted parameters.

as those found in Refs. [8, 11, 23]. The adjustment to the graph is of exponential type with values of the coefficients *A*, *M*, and *B* of 137185.7, 0.020758, and −156691, respectively. The coefficient of correlation of the exponential adjustment is 0.79.

$$T = 137185.7\ T_R^{\ 0.020758} - 156691 \tag{8}$$

The values of the coefficients depend on the geological conditions, so Ebong et al. [11] found $T = 0.2319 T_R^{\ 0.7246}$, Perdomo et al. [23] $T = 0.53\ T_R^{\ 0.98}$, Ponzini et al. [8] $T_R = 4.022 \times 10^3 T^{0.577} + 17.2$.

Other authors have found direct linear relationship: Niwas and Celik [10] assumed that the product $K\sigma$ remains unchanged in areas with similar geological setting and water quality; Frohlich and Kelly [33], for a constant water resistivity value of 100 Ω-m, obtained a linear relationship between T_R and T; and Kosinsky and Kelly [34] in glacial outwash material.

Since $K\sigma$ is not constant, then according to [10], the expected relation between T and T_R is not linear but exponential. This is due to the geological nature of the study area, which is expressed through the distribution of T and the EC of the aquifer. The values of T are high and vary from 452.4 to 4294.6 m^2/day. The EC varies between 0.45 and 1.35 mS/cm.

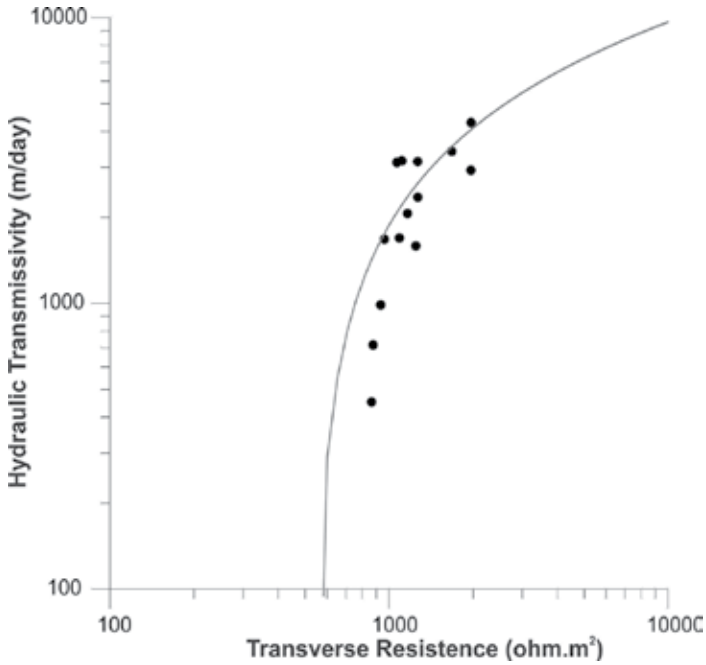

Figure 6. Relation between hydraulic transmissivity and transverse resistance.

4.4. The relationship between K and T_R

Hydraulic conductivity K was obtained from the relation $T = Kb$, finding that this varies from 4.77 m/day to 47.83 m/day. It is an essential parameter to describe water movement under saturated conditions [35]. With the T_R and K values of each well, **Figure 6** was constructed, which in an analogous way to $T - T_R$. The values of the coefficients of the exponential adjustment A, M, and B were 367.21, 0.0548, and −518.813, respectively. The coefficient of correlation of the exponential adjustment is 0.678.

$$K = 367.21^{0.0548} - 518.813 \quad (9)$$

Measurements of aquifer resistivity are useful to estimate the aquifer hydraulic conductivity due to the fundamental relation between K and electrical conductivity [36]. Kelly [37] worked with glacial outwash materials and obtained a linear connection between resistivity and K in relatively uniform water quality. The exponential relation allows to correlate K with T_R, in an area where T and σ already indicated are not uniform.

5. Conclusions

Exponential relations between geohydrologic parameters (T, K) and geoelectric parameter (T_R) have been found with a good statistical adjustment. These relations allow to characterize the

water quality and the transmission capacity of the aquifer; therefore, for placements between the wells with which the empirical relations were obtained, there is a characterization so that from the realization of VES a geoelectric section of the subsoil, which includes the value of R_o, thus obtaining T_R. When T_R is obtained, relations with T and K can be found. With these relations, scenarios can be proposed on descents in future wells to be performed. Thus, the relations found guide the planning and use of groundwater.

Acknowledgements

Our gratitude to the General Direction of Research and Post graduate of the Autonomous University of Sinaloa for supporting the Project and generating the suitable conditions to fulfill the present work.

Author details

Héctor José Peinado Guevara[1]*, Jaime Herrera Barrientos[2], Omar Delgado Rodríguez[3], Víctor Manuel Peinado Guevara[1], Omar Llanes Cárdenas[4] and María Ladrón De Guevara Torres[5]

*Address all correspondence to: hpeinado75@hotmail.com

1 Escuela de Ciencias Económicas y Administrativas, Universidad Autónoma de Sinaloa, San Joachín, Guasave, Sinaloa, México

2 Centro de Investigación Científica y de Educación Superior de Ensenada, Baja California, Zona Playitas, Ensenada, B.C., México

3 División de Geociencias Aplicadas, Instituto Potosino de Investigación Científica y Tecnológica, San Luis Potosí, S.L.P., México

4 Instituto Politécnico Nacional Unidad CIIDIR-Sinaloa, Colonia San Joachin, Guasave, Sinaloa, México

5 Instituto Politécnico Nacional Unidad CIIDIR-Oaxaca, Noche Buena, Santa Cruz Xoxocotlán, Oaxaca, México

References

[1] Painter SL, Woodbury AD, Jiang Y. Transmissivity estimation for highly heterogeneous aquifers: comparison of three methods applied to the Edwards Aquifer, Texas, USA. Hydrogeology Journal. 2007; **15**(2): 315–331. doi:10.1007/s10040-006-0071-y

[2] Asfahani J. Hydraulic parameters estimation by using an approach based on vertical electrical soundings (VES) in the semi-arid Khanasser valley region, Syria. Journal of African Earth Sciences. 2016; **117**: 196–206. doi:10.1016/j.jafrearsci.2016.01.018

[3] Tizro AT, Voudouris K, Basami Y. Estimation of porosity and specific yield by application of geoelectrical method–a case study in western Iran. Journal of Hydrology. 2012; **454**: 160–172. doi:10.1016/j.jhydrol.2012.06.009

[4] Orellana E. Geoelectric prospecting in direct current (2nd ed.). Madrid: Paraninfo; 1982, 578 p. [In Spanish]

[5] Silva Busso AS, Amato SD. Hydrogeological aspects of the periserrana region of Tandilia (Buenos Aires, Argentina). Boletín geológico y minero. 2012; **123**(1): 27–40. [In Spanish]

[6] Archie GE. The electrical resistivity log as an aid in determining some reservoir characteristics. Transactions AIMME. 1942; **46**: 54. doi:10.2118/942054-G

[7] Croft MG. A method of calculating permeability from electric logs. Geological Survey Research. 1971; **750-B**, 265–269

[8] Ponzini G, Ostroman A, Molinari M. Empirical relations between electrical transverse resistance and hydraulic transmissivity. Geoexploration. 1984; **22**(1): 1–15. doi:10.1016/0016-7142(84)90002-4

[9] Chandra S, Ahmed S, Ram A, Dewandel B. Estimation of hard rock aquifers hydraulic conductivity from geoelectrical measurements: a theoretical development with field application. Journal of Hydrology. 2008; **357**(3): 218–227. doi:10.1016/j.jhydrol.2008.05.023

[10] Niwas S, Celik M. Equation estimation of porosity and hydraulic conductivity of Ruhrtal aquifer in Germany using near surface geophysics. Journal of Applied Geophysics. 2012; **84**: 77–85. doi:10.1016/j.jappgeo.2012.06.001

[11] Ebong ED, Akpan AE, Onwuegbuche AA. Estimation of geohydraulic parameters from fractured shales and sandstone aquifers of Abi (Nigeria) using electrical resistivity and hydrogeologic measurements. Journal of African Earth Sciences. 2014; **96**: 99–109. doi:10.1016/j.jafrearsci.2014.03.026

[12] Kazakis N, Vargemezis G, Voudouris KS. Estimation of hydraulic parameters in a complex porous aquifer system using geoelectrical methods. Science of the Total Environment. 2016; **550**: 742–750. doi:10.1016/j.scitotenv.2016.01.133

[13] Nourbehect B. Irreversible thermodynamic effects in inhomogeneous media and their applications in certain geoelectric problems (No. 9017-4). Massachusetts Institute of Technology Cambridge Geophysics Laboratory; 1963, 149 p

[14] Joel ES, Olasehinde PI, De DK, Omeje M, Adewoyin OO. Estimation of aquifer transmissivity from geo-physical data. A case study of Covenant University and Environs, southwestern Nigeria. Science International (Lahore). 2016; **28**(4): 3379–3385

[15] Aizebeokhai AP, Oyebanjo OA. Application of vertical electrical soundings to characterize aquifer potential in Ota, Southwestern Nigeria. International Journal of Physical Sciences. 2013; **8**(46): 2077–2085

[16] Sattar GS, Keramat M, Shahid S. Deciphering transmissivity and hydraulic conductivity of the aquifer by vertical electrical sounding (VES) experiments in Northwest Bangladesh. Applied Water Science. 2016; **6**(1): 35–45. doi:10.1007/s13201-014-0203-9

[17] Teikeu WA, Njandjock PN, Bisso D, Atangana QY, Nlomgan JPS. Hydrogeophysical parameters estimation for aquifer characterisation in hard rock environment: a case study from Yaounde, Cameroon. Journal of Water Resource and Protection. 2012; **4**(11): 944–953. doi:10.4236/jwarp.2012.411110

[18] Utom AU, Odoh BI, Okoro AU. Estimation of aquifer transmissivity using Dar Zarrouk parameters derived from surface resistivity measurements: a case history from parts of Enugu Town (Nigeria). Journal of Water Resource and Protection. 2012; **4**(12): 993–1000. doi:10.4236/jwarp.2012.412115

[19] Oborie E, Udom GJ. Determination of aquifer transmissivity using geoelectrical sounding and pumping test in parts of Bayelsa State, Nigeria. Journal of Physical and Environmental Science Research. 2014; **2**(2): 32–40

[20] Singh S, Singh VS. Estimation of hydraulic characteristics from electrical resistivity data in coastal aquifers of southern India. Journal of the Geological Society of India. 2016; **88**(1): 77-86. DOI: 10.1007/s12594-016-0460-3

[21] Niwas S, Singhal DC. Estimation of aquifer transmissivity from Dar-Zarrouk parameters in porous media. Journal of Hydrology. 1981; **50**: 393–399. doi:10.1016/0022-1694(81)90082-2

[22] Soupios PM, Kouli M, Vallianatos F, Vafidis A, Stavroulakis G. Estimation of aquifer hydraulic parameters from surficial geophysical methods: a case study of Keritis Basin in Chania (Crete–Greece). Journal of Hydrology. 2007; **338**(1): 122–131. doi:10.1016/j.jhydrol.2007.02.028

[23] Perdomo S, Ainchil JE, Kruse E. Hydraulic parameters estimation from well logging resistivity and geoelectrical measurements. Journal of Applied Geophysics. 2014; **105**: 50–58. doi:10.1016/j.jappgeo.2014.02.020

[24] INEGI (National Institute of Statistic and Geography). Statistical and geographical directory of Sinaloa, Mexico. 2014; 53 p. [In Spanish]

[25] INEGI (National Institute of Statistic and Geography). Geographical Information of the United Mexican States, municipality of Guasave, Sinaloa, Mexico. Geostatistical key 25011. México; 2009, 9 p. [In Spanish]

[26] Villanueva M, Iglesias L. Wells and aquifers evaluation techniques through pumping tests. Madrid: Ibergesa; 1984, 426 p. [In Spanish]

[27] Guptasarma D. Optimization of short digital linear filters for increased accuracy. Geophysical Prospecting, 1982; **30**: 501–514. doi:10.1111/j.1365-2478.1982.tb01320.x

[28] Peinado-Guevara H, Green-Ruíz C, Herrera-Barrientos J, Escolero-Fuentes O, Delgado-Rodríguez O, Belmonte-Jiménez S, Ladrón De Guevara M. Relationship between chloride concentration and electrical conductivity in groundwater and its estimation from

vertical electrical soundings (VESs) in Guasave, Sinaloa, Mexico. Ciencia e investigación agraria. 2012; **39**(1): 229–239. doi:10.4067/S0718-16202012000100020

[29] Norzagaray-Campos M, Herrera-Barrientos J, Herrera-Barrientos F, Muñoz-Sevilla P, Yuri-Mendoza E. Capurro-Filigrasso: Simulación bidimensional del transporte de solutos en la costa del acuífero Santo Domingo, Ensenada; B. C. México. Revista Geologica America Central. 2002; **27:** 153–163

[30] Grellier S, Reddy KR, Gangathulasi J, Adib R, Peters CC. Correlation between electrical resistivity and moisture content of municipal solid waste in bioreactor landfill. Geotechnical Special Publication. 2007; **163**: 1–14

[31] Peinado GHJ, Green RCR, Herrera BJ, Escolero FÓA, Delgado RO, Belmonte JSI, Ladrón De Guevara MDLÁ. Quality and suitability for agricultural and domestic use of water from the Sinaloa river aquifer, coastal portion. Hidrobiológica. 2011; **21**(1): 63–76

[32] Heath RC. Basic ground-water hydrology. U.S. Geological Survey Water-Supply paper 2220. U.S. Geological Survey, Reston, Virginia, ISBN 0-607-68973-0. 1983; 86 p.

[33] Frohlich RK, Kelly WE. The relation between hydraulic transmissivity and transverse resistance in a complicated aquifer of glacial outwash deposits. Journal of Hydrology. 1985; **79**: 215–229. doi:10.1016/0022-1694(85)90056-3

[34] Kosinsky WK, Kelly WE. Geoelectric sounding for predicting aquifer properties. Ground Water. 1981; **19**(2): 163–171. doi:10.1111/j.1745-6584.1981.tb03455.x

[35] Jadczyszyn J, Niedzwiecki J. Relation of saturated hydraulic conductivity to soil losses. Polish Journal of Environmental Studies. 2005; **14**(4): 431–435

[36] Kaleris VK, Ziogas AI. Estimating hydraulic conductivity profiles using borehole resistivity logs. Procedia Environmental Sciences. 2015; **25:** 135–141. doi:10.1016/j.proenv.2015.04.019

[37] Kelly WE. Geoelectric sounding for estimating aquifer hydraulic conductivity. Ground Water. 1978; **15**(6): 420–425. doi:10.1111/j.1745-6584.1977.tb03189.x

Chapter 6

Assessment of Cryoprotectant Concentration by Electrical Conductivity Measurement and Its Applications in Cryopreservation

Zhiquan Shu, Hsiu-Hung Chen, Xiaoming Zhou and Dayong Gao

Additional information is available at the end of the chapter

http://dx.doi.org/10.5772/67747

Abstract

This chapter presents an important application of the electrical conductivity measurement in cryopreservation. Long-term cryopreservation of cells and tissues is essential in both clinical treatments and fundamental researches. In order to reduce the cryo-injury to the cells during cryopreservation, cryoprotective agents (CPAs) should be added before freezing, but also removed after thawing duo to the cytotoxicity. In these steps, severe osmotic stresses may result in injuries to the cells too. Therefore, monitoring the addition and removal of CPAs to the cell samples is critical in order to prevent the osmotic injury. In this chapter, the electrical conductivity measurement was applied to assess the CPA concentration in cryopreservation. Firstly, the standard correlations between the CPA concentration and the electrical conductivity of the solutions (including CPA-NaCl-water ternary solutions and CPA-albumin-NaCl-water quaternary solutions) were experimentally obtained for a few mostly used CPAs. Then a novel "dilution-filtration" system with hollow fiber dialyzer was designed and applied to remove the CPA from the solutions effectively. Measurement of electrical conductivity was validated as a safer and easier way to on-line and real-time monitoring of CPA concentration in cell suspensions. This work demonstrated a very important application of electrical conductivity in the biomedical engineering field.

Keywords: electrical conductivity (EC), cryopreservation, cryoprotective agent (CPA), addition and removal of CPA, dilution-filtration, hollow fiber dialyzer

1. Introduction

Cryopreservation of biological materials, including DNA/RNA, virus, bacteria, cells, tissues, and organs, both diseased and healthy samples, is essential for both fundamental researches and clinical applications. In cryopreservation, biological materials are cooled down to dormant state at low temperatures (such as −80 or −196°C, the temperature of liquid nitrogen) for long-term storage, and later thawed back to the normal physiological temperatures before usage with recovered viability and functionalities. However, there is a contradictory between the facts that the biological materials can be sustained at low temperatures, whereas their functions can be damaged during the cooling and thawing processes. There were very few successful cases of cryopreservation before 1940s.

Since glycerol was discovered to protect cells from cryoinjury in the late 1940s [1], the field of cryopreservation entered a new era. In order to reduce the cryoinjury to cells, cryoprotective agents (CPAs) should be added before freezing. Later, more and more CPAs have been proved effective for different cell types under diverse conditions, such as dimethyl sulfoxide (DMSO or Me_2SO), glycerol, propylene glycol (PG), ethylene glycol (EG), sugars (glucose, sucrose, trehalose), and macromolecules (dextran, hydroxyethyl starch (HES), polyvinylpyrrolidone (PVP)), which have indelible contributions to fundamental researches and clinical trials. However, CPAs might be toxic to cells, especially when cells and CPAs coexist at temperatures above 0°C for extended time. Meanwhile, if the added CPA is infused to patients together with the frozen-thawed cells, adverse reactions from mild to severe life-threatening problems may happen. For example, as the most widely used CPA, Me_2SO transplanted to patients may cause nausea, vomiting, chill, dyspnea, cardiac arrhythmia, hypotension, oliguric renal failure, and heart block, especially for pediatric patients [2–5]. The adverse effects of Me_2SO can even be cumulative when multi-dose cell therapies are implemented. Thus, generally, it is recommended to remove CPA from the cell suspension after thawing to an acceptable extent.

However, during the CPA removal, as well as its addition, osmotic injuries may happen to the cells if suboptimal procedures are applied. When a CPA with high concentration is added to or removed from cell suspensions, due to the osmolality difference between intracellular and extracellular solutions, cells will shrink or expand dynamically. This cell volume excursion can cause severe injury to the cells, that is, osmotic injury [6]. Therefore, fast and accurate assessment of the CPA concentration in the cell suspension during addition and removal is very important. In order to assess the CPA concentration in cell suspensions, a few methods have been applied by researchers, such as capillary zone electrophoresis [7]), high-performance liquid chromatography (HPLC) [8], and gas chromatography [9]. However, all these approaches are very complex, time-consuming, and expensive. In addition, special chemical agents, apparatuses, and expertise are needed. Inspired by the fact that the electrical conductivity of solutions depends on the composition and concentration of the ingredients, in this chapter, we demonstrated a method of electrical conductivity (EC) measurement to assess the CPA concentration [10, 11], which has been proved much simpler and cheaper, thus, more applicable for real-time monitoring of the CPA concentration during the CPA addition and washing procedures.

For the CPA removal method, nowadays, centrifugation is the most widely used method [12–16]. Briefly, isotonic washing solution is added to the cell-CPA suspension slowly. After equilibration

http://dx.doi.org/10.5772/67747

for a few minutes, the mixture is centrifuged, and then, CPA in the supernatant is removed. This dilution-centrifugation procedure usually needs to be repeated for a few times until the residual CPA concentration reaches an acceptable level. This method has many disadvantages, such as intense labor and time consumption, high possibility of contamination, osmotic and mechanical injury to the cells, clumping of cells due to centrifugation, and others. Thus, it would be highly desirable to find more reliable alternative methods for a CPA removal. Thus far, a few alternative approaches have been developed for CPA removal. Dialysis mass transfer in hollow fiber dialyzer has been proposed by some researchers [17–20]. However, the large osmolality gradient across the hollow fiber membranes can cause severe osmotic damage to the cells, especially at the beginning of the mass transfer process when cell suspension and diluent solution mix together in the dialyzer. To reduce osmotic injury to the cells, priming of the dialyzer with hyperosmotic solution first, which introduces extra complexity and time consumption, is generally required. Meanwhile, due to the non-uniform distribution of osmolality gradient across hollow fiber membranes along the fibers, mass transfer in the dialyzer is very complicated and hard to be well controlled. These problems prevent dialysis method from being an effective and reliable approach for CPA removal. Recently, Hubel et al. developed a method based on mass diffusion in microfluidic flows for CPA removal [21, 22]. However, therein the mass transfer rate is low since passive diffusion due to concentration gradient is the driving force for mass transfer. This system is hard to be scaled up for large volume samples.

In order to overcome the difficulties mentioned above, we proposed a method of "dilution-filtration" with hollow fibers for removing CPAs [11, 23, 24] (which is also applicable for CPA addition). The osmotic shock to cells when contacting with diluent and the removal rate of CPA can be well controlled by the dilution ratio and filtration rate, respectively. Compared to other methods, this "dilution-filtration" system can decrease cell loss, improve CPA removal effectiveness, easily manipulate the final sample volume, and diminish the possibility of contamination due the closed-loop system.

In this chapter, the electrical conductivity measurement was applied to assess the CPA concentration in cryopreservation. First, the standard correlations between the CPA concentration and the electrical conductivity of the solutions (including CPA-NaCl-water ternary solutions and CPA-albumin-NaCl-water quaternary solutions) were experimentally obtained for a few mostly used CPAs, including Me_2SO, EG, and glycerol. Then, the "dilution-filtration" system with hollow fiber dialyzer was applied to remove CPA from the solutions.

2. Electrical conductivity (EC) of the CPA solutions

2.1. Materials and methods

2.1.1. Measurements of EC of the Me_2SO-NaCl-water ternary solutions

The EC of Me_2SO-NaCl-water ternary solutions with different Me_2SO and NaCl concentrations was measured. In the solution preparation, NaCl-water solutions (NaCl: 99.6% pure, Mallinckrodt Baker, Inc., Phillipsburg, NJ) were first prepared with NaCl concentrations of 0.9, 1.8, 4.5, and 9 wt%, which were presented as r = 1, 2, 5, and 10, respectively, that is, r is the

relative concentration of NaCl compared to the isotonic NaCl solution. Then, Me_2SO (100% pure, Mallinckrodt Baker, Inc., Phillipsburg, NJ) was added to the NaCl-water solutions with volume percentages of 0, 2.5, 5, 7.5, 10, 20, 30, 40, and 50% (v/v). The EC data of the ternary solutions were measured with a conductivity meter (Orion 4-Star, Thermo Fisher Scientific Inc., Waltham, MA) at the AUTO-READ mode at room temperature (22 $\pm$ 0.5°C). After each measurement, the conductivity probe was rinsed with DI water and dried before the next measurement. Each individual solution was measured three times.

2.1.2. Measurements of EC of glycerol-NaCl-water and ethylene glycol-NaCl-water ternary solutions

Glycerol and EG are the other two types of CPAs that have been widely used in cryopreservation. Similar to the procedures mentioned above, the ternary solutions consisted of glycerol or EG (Mallinckrodt Baker, Inc., Phillipsburg, NJ), NaCl and DI water. When preparing the ternary solutions, NaCl crystal powder was first dissolved in DI water by weight to obtain final concentrations of 0.9, 1.8, 4.5, and 9 wt%, which were presented as r = 1, 2, 5, and 10, respectively. Second, glycerol or EG was added to NaCl-water solutions with different volume percentages from 0 to 50% (v/v). When preparing the glycerol solution, mass weighting was applied to precisely control the glycerol volume since small volume of glycerol was hard to be prepared due to its high viscosity. Then, the solutions with different NaCl and CPA concentrations were measured at room temperature for EC. For each solution, the measurement was performed at least for three times.

2.1.3. Effect of albumin on the electrical conductivity of the NaCl-albumin-water ternary solutions

Albumin usually exists in blood, culture medium, and cell products. In order to investigate the influence of albumin on the EC of the solution, NaCl-albumin-water ternary solutions were prepared. Similar to the procedure above, 0.9% (w/v) NaCl solution was prepared first. Then, bovine serum albumin (Sigma-Aldrich) was added to the NaCl solution with different final concentrations: 0, 2, 4, 6, 8, and 10% (w/v). Then, the EC of these solutions was measured at room temperature. Each solution was measured for three times.

2.1.4. Effect of Me_2SO on the electrical conductivity of the NaCl-albumin-Me_2SO-water quaternary solutions

In cryopreservation, cells may be in the NaCl (or other salts)-albumin-Me_2SO-water solution. During Me_2SO addition and removal, Me_2SO concentration increases or decreases, while albumin remains in the suspension. In order to apply the EC measurement to assess the Me_2SO concentration, we need to consider the influence of Me_2SO on the EC data.

NaCl-albumin-Me_2SO-water solutions with different Me_2SO concentrations were prepared and measured. Briefly, a ternary solution of 0.9% (w/v) NaCl-5% (w/v) albumin-water was prepared first. Here, 5% albumin concentration was chosen because this concentration was generally used in cell culture media. Then, this ternary solution was mixed with Me_2SO to make NaCl-albumin-Me_2SO-water solutions with different Me_2SO concentrations (0, 2.5, 5, 7.5, 10, 20, 30, 40, 50% (v/v)). When preparing these solutions, they were immersed in ice and the mixing was performed slowly such that the solution temperature was not heated up too

much. Then, the EC of these solutions was measured at room temperature. Each solution was measured at least for three times.

2.2. Results

2.2.1. Standard electrical conductivity data of Me_2SO-NaCl-water ternary solutions

The EC data of Me_2SO-NaCl-water ternary solutions are shown in **Figure 1**. Obviously, the EC depends on both the concentrations of NaCl and Me_2SO. The higher of NaCl concentration (larger r value) or the lower of Me_2SO concentration, the higher will be the EC of the solution. From the data, it shows that the dependence of EC on Me_2SO and NaCl concentrations can be written as an exponential function:

$$EC = A \times e^{B \cdot C} \tag{1}$$

where EC is the electrical conductivity of the ternary solutions (mS/cm); C is the concentration of Me_2SO (v/v, %); A and B are constants. It is interesting that B = −0.036, the same for different r values (different NaCl concentrations) (except B = −0.035 for r = 1, which difference may be due to the measurement accuracy). A is determined by NaCl concentration (shown in **Figure 2**) and can be estimated by:

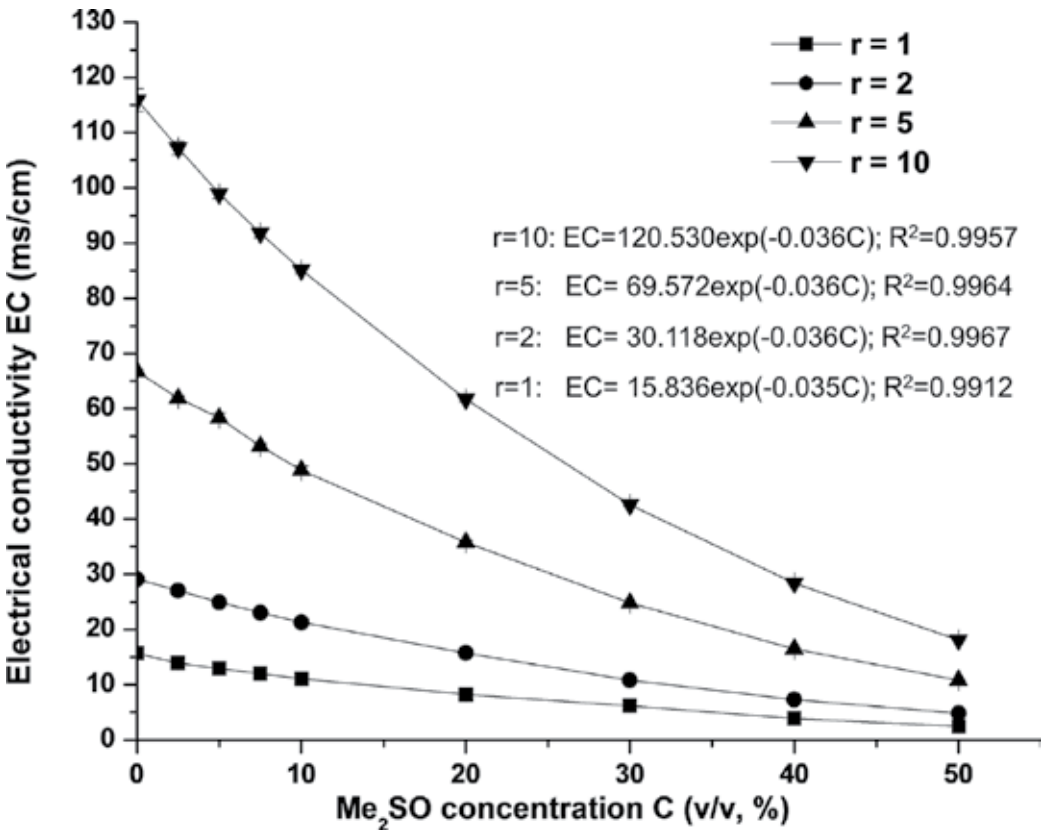

Figure 1. Electrical conductivity of Me_2SO-NaCl-water ternary solutions.

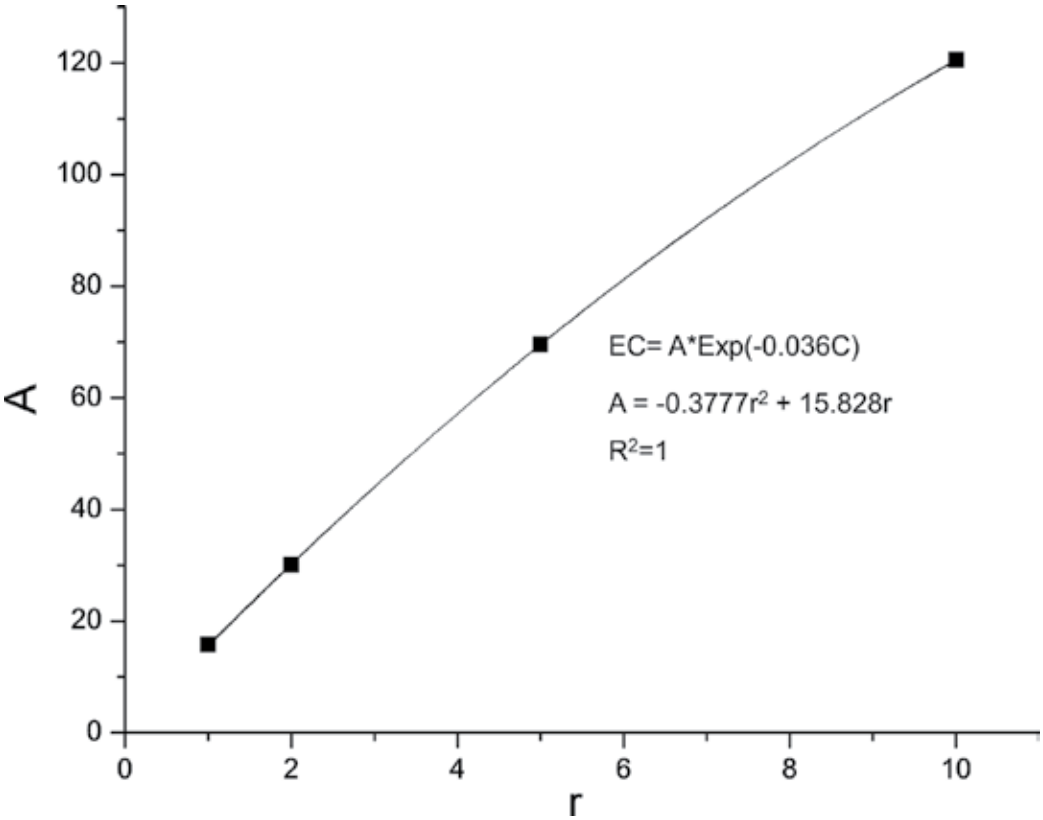

Figure 2. Dependence of A on NaCl concentration (*r*).

$$A = -0.3777r^2 + 15.828r \tag{2}$$

Accordingly, the EC of Me_2SO-NaCl-water ternary solutions can be estimated by:

$$EC = (-0.3777r^2 + 15.828r) \times e^{-0.036 \cdot C} \tag{3}$$

Specifically, for Me_2SO-0.9% NaCl-water ternary solutions (r = 1, the general case for cell suspension), the dependence of EC on Me_2SO concentration can be fitted by:

$$EC = 15.836 \times e^{-0.035 \cdot C} \tag{4}$$

2.2.2. Standard electrical conductivity data of glycerol-NaCl-water and ethylene glycol-NaCl-water ternary solutions

The EC results of glycerol-NaCl-water and ethylene glycol-NaCl-water ternary solutions are shown in **Figures 3** and **4**. Obviously, when CPA concentration increases or salt concentration decreases, the EC of the solution decreases. The dependence of CPA concentration on the EC can be also fitted by exponential equations.

http://dx.doi.org/10.5772/67747

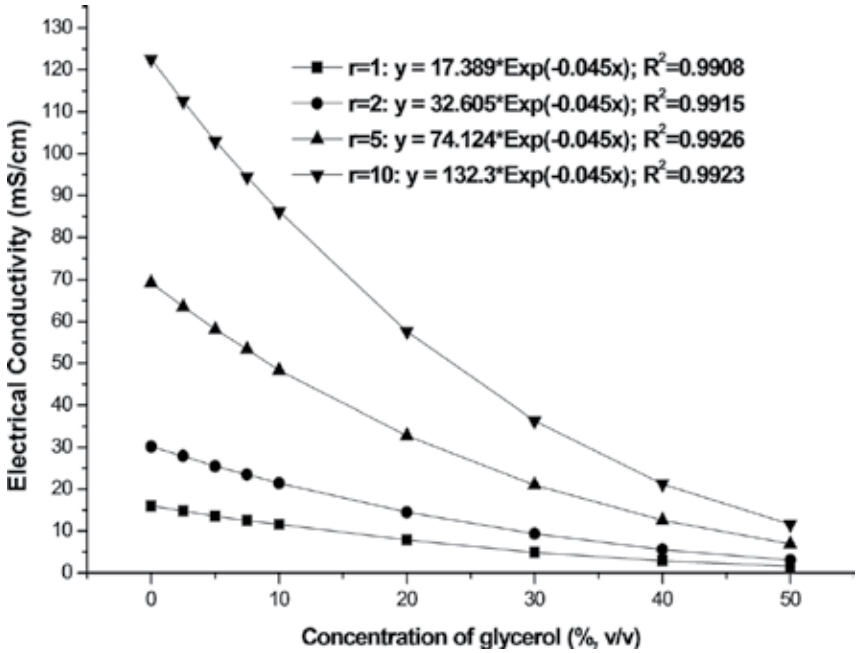

Figure 3. Electrical conductivity of glycerol-NaCl-water ternary solutions.

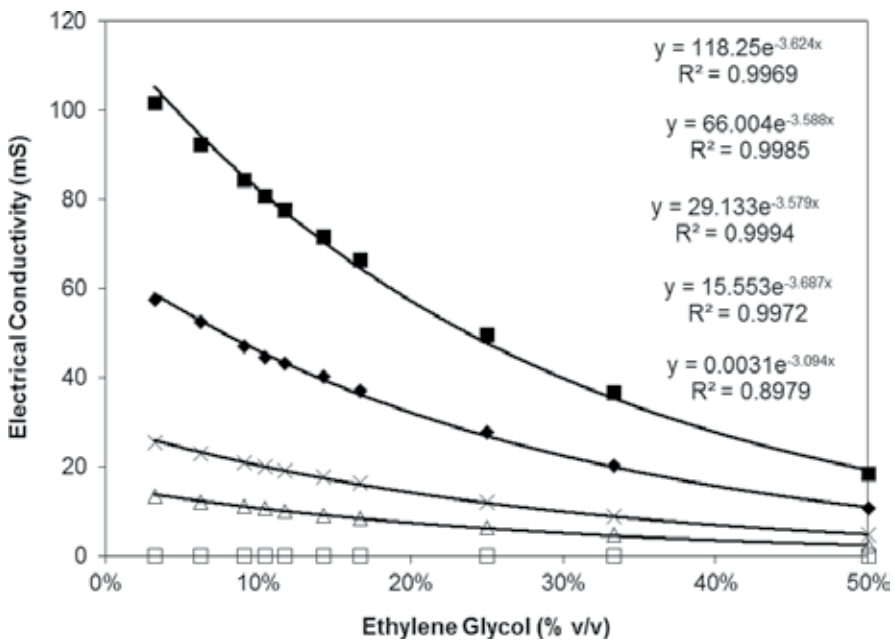

Figure 4. Electrical conductivity of ethylene glycol-NaCl-water ternary solutions.

For glycerol-NaCl-water ternary solutions, it can be presented as follows:

$$EC = A \cdot e^{-0.045C}, \quad (R^2 > 0.99) \tag{5}$$

For ethylene glycol-NaCl-water ternary solutions, the EC can be predicted as follows:

$$EC = A \cdot e^{-0.036C}, \quad (R^2 > 0.99) \tag{6}$$

A is determined by the salt concentration (r value).

2.2.3. Effect of albumin on the electrical conductivity of the 0.9% NaCl-albumin-water ternary solutions

The effect of albumin on the EC of albumin-NaCl-water ternary solutions is shown in **Figure 5**. In this experiment, the concentration of NaCl in the solutions was constant (0.9% w/v), and albumin concentration changed from 0 to 10% (w/v). Obviously, when the concentration of albumin increases, the EC of the solution decreases. The data can be fitted linearly as follows:

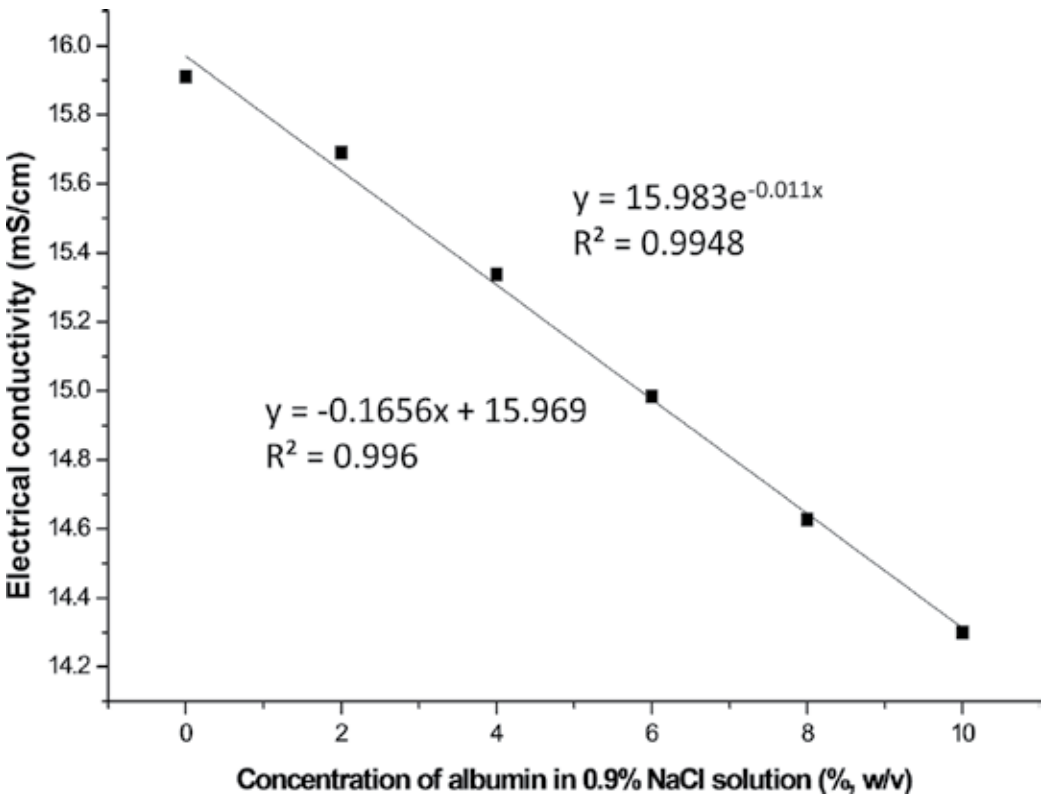

Figure 5. Effect of albumin on the electrical conductivity of albumin-0.9% NaCl-water ternary solutions.

$$EC = -0.1656 \cdot C + 15.969, \quad (R^2 = 0.996) \tag{7}$$

where C is the concentration of albumin (w/v%).

The data can also be fitted exponentially as follows:

$$EC = 15.983 \cdot e^{-0.011C}, \quad (R^2 = 0.9948) \tag{8}$$

Compared to Eq. (3), it implies that albumin and Me_2SO decrease the EC of the solutions with similar exponential ways, yet with different decreasing rates. For Me_2SO, the exponential constant B is −0.036, and for albumin, the constant is −0.011.

2.2.4. Effect of Me_2SO on the electrical conductivity of the 0.9% NaCl-5% albumin-Me_2SO-water quaternary solutions

In the Me_2SO-albumin-NaCl-water quaternary solutions, only the concentration of Me_2SO was changed. Its effect on the EC of the solutions is shown in **Figure 6**. Once again, we can see that the data can be well fitted by an exponential function as follows:

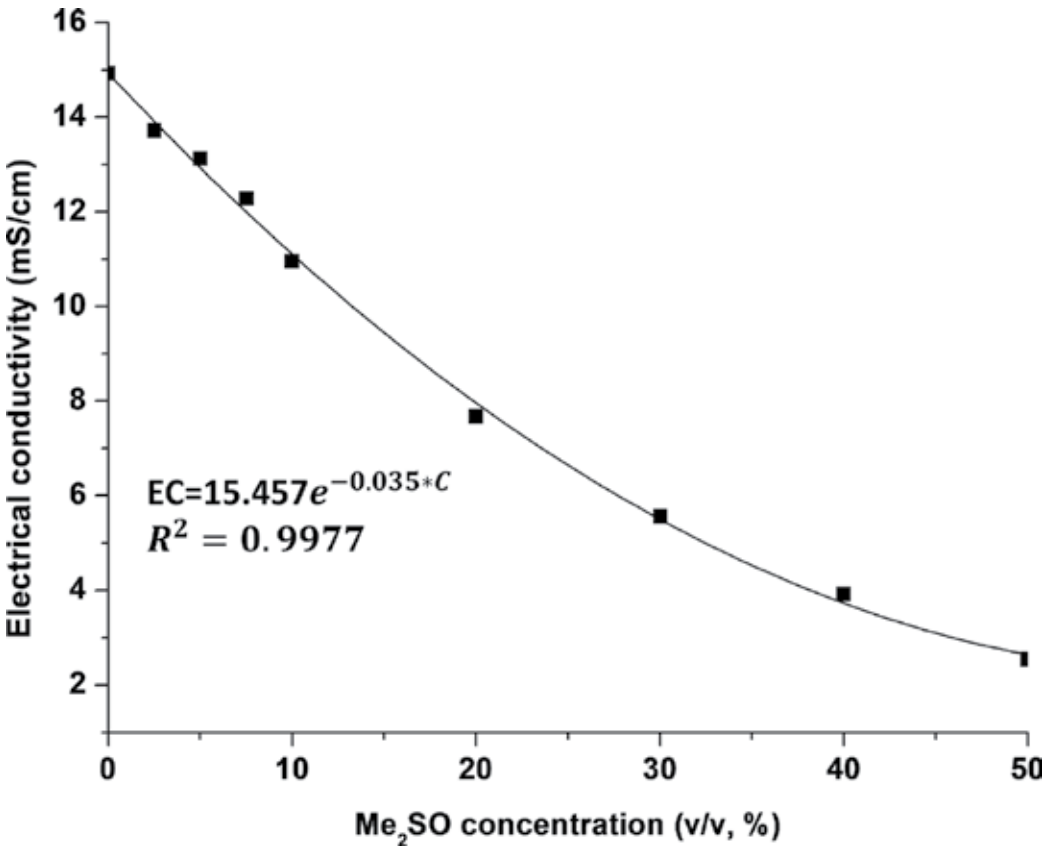

Figure 6. Effect of Me2SO on the electrical conductivity of Me_2SO-5% albumin-0.9% NaCl-water solutions.

$$EC = 15.457 \cdot e^{-0.035C}, \quad (R^2 = 0.9977) \tag{9}$$

where the exponential constant is −0.035, very close to the constant in Eq. (3).

3. Removal of CPA with dilution-filtration and assessment of CPA concentration with electrical conductivity measurement

3.1. Materials and methods

3.1.1. "Dilution-filtration" system for CPA removal

The "dilution-filtration" system for CPA removal is sketched in **Figure 7**. It mainly consists of three peristaltic pumps (400F/M1, Watson-Marlow, Wilmington, MA), one hollow fiber dialyzer (Hemoflow, F5HPS, Fresenius Medical Care, St. Wendel, Germany), a T-shape connector, and some silicon tubings (985-75, Pall, Port Washington, NY). Pump 1 and pump 3 cooperate to control the fluxes of diluent (q_d) and cell suspension (q_c). Diluent and cell suspension mix thoroughly in the T-shape connector and tubing, pass through the hollow fibers, and then, return to the cell suspension container. Pump 2 controls the filtration rate (q_u). Filtrated solution is collected in the waste solution container. Herein, the diameter of the tubings perfectly matches the pumps. When the peristaltic pump stops, it can also function to clamp the tubing loop, which prevents pressure loss inside the dialyzer. The dialyzer made of polysulfone was chosen in this work because of its large cross-membrane flux capability, high clearance efficiency of CPA, and low cost. Macromolecules (such as proteins and albumin) and cell debris cannot pass through the hollow fiber membranes, which leads to the simplicity of contents in the waste solution (only saline and permeable CPA, e.g., Me_2SO) and benefits the monitoring of CPA concentration.

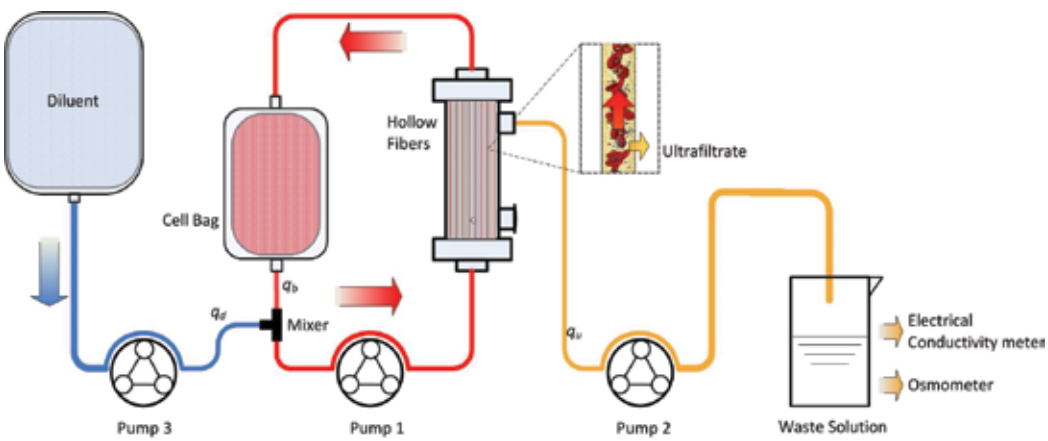

Figure 7. "Dilution-filtration" system for CPA removal.

http://dx.doi.org/10.5772/67747

3.1.2. Me_2SO removal with the "dilution-filtration" system

The 10% (v/v) Me_2SO-0.9% (w/v) NaCl-water ternary solution and 10% Me_2SO (v/v)-5% (w/v) BSA-0.9% (w/v) NaCl-water quaternary solution were used to mimic cell suspension with CPA. Isotonic NaCl solution (0.9%, w/v) was used as diluent. The actual pumping and filtration rates of the three pumps were calibrated before experiments. The "dilution-filtration" protocol was as follows:

Step 1 (priming): Pump 2 and pump 3 were shut down. Pump 1 was run at 100 mL/min for 1 min to drive the "cell suspension" to prime the hollow fibers (from bottom to top) and tubings.

Step 2 (dilution-filtration): Pump 1 and pump 3 were set to achieve q_c = 200 mL/min and q_d = 20 mL/min. Pump 2 was set to achieve filtration rate of q_u = 20 mL/min. Herein, $q_d = q_u$ such that the volume of "cell suspension" kept constant. The "cell suspension" container was kept agitating for better mixing. This step was run for 45 min. The osmolality and EC of both the "cell suspension" and waste solution were measured after every minute during the process.

Step 3 ("cell suspension" retrieval): Pump 2 and pump 3 were shut down. Pump 1 was set to run slowly (20 mL/min) in reverse direction for at least 4 min to retrieve the "cell suspension" in the tubings and dialyzer back to the cell suspension container.

3.1.3. Real-time monitoring of Me_2SO concentration

In order to real-time monitor the Me_2SO concentration during processing, EC measurements of the filtrated product (waste solution) were implemented. In Step 2 of the procedure (dilution-filtration) described above, after every minute, the EC of the newly collected waste solution (volume: ~20 mL) was measured. For verification, the osmolality of the waste solution was also measured by an osmometer (Wescor Inc., Logan, UT) with the working mechanism of vapor pressure assessment. The EC and osmolality of the "cell suspension" in the experiments were also measured after each minute of dilution-filtration for comparison with those of waste solution. All the measurements were conducted twice for each data.

3.2. Results

3.2.1. Me_2SO removal from Me_2SO-0.9% NaCl-water ternary solution by "dilution-filtration"

The experiment results of Me_2SO removal from Me_2SO-0.9% NaCl-water ternary solution by "dilution-filtration" system are shown in **Figure 8**. After processing for 45 min, the volume of "cell suspension" was 196 mL, which was very close to the original volume (200 mL). Totally, 860 mL isotonic NaCl solution was used as diluent. **Figure 8A** shows the EC and osmolality of the waste solution that was achieved every minute. According to Eq. (4), EC data were converted to Me_2SO concentrations of the waste solution, shown in **Figure 8B**. The Me_2SO concentration decreased to <1% (v/v) after 35 min. The results also show that Me_2SO concentrations estimated

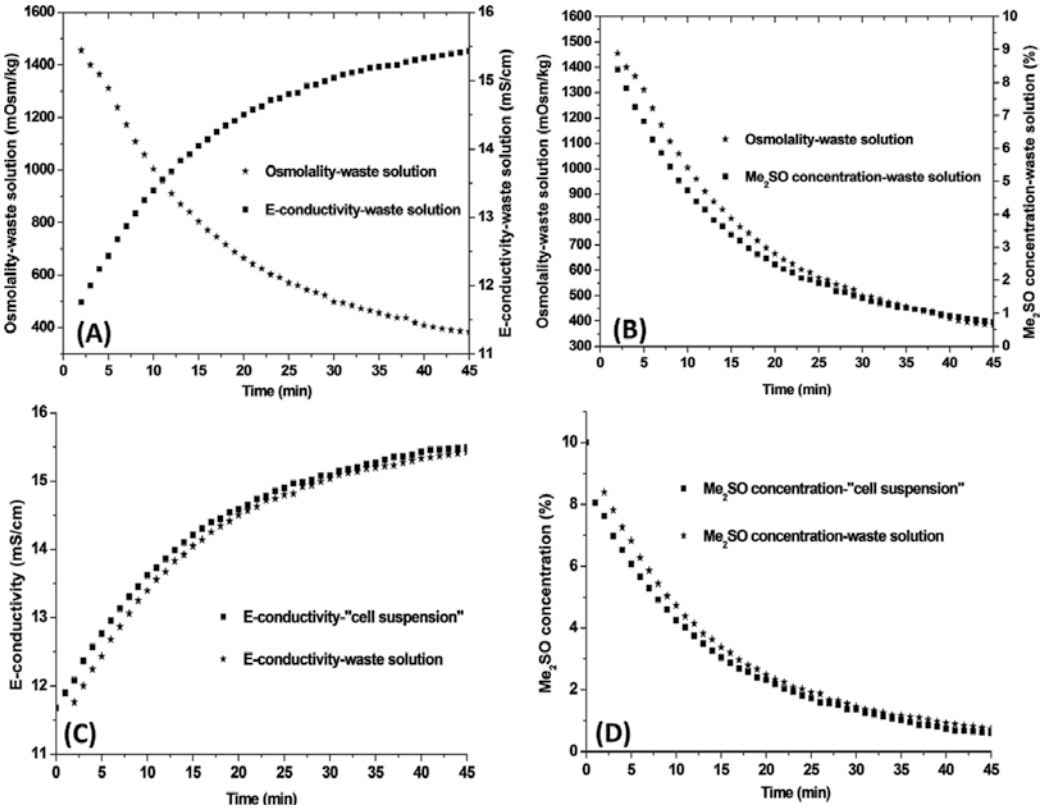

Figure 8. Me_2SO removal from Me2SO-NaCl-water ternary solution by "dilution-filtration." (A) Conductivity and osmolality of waste solution; (B) Me_2SO concentration and osmolality of waste solution; (C) conductivity of "cell suspension" and waste solution; and (D) Me_2SO concentration of "cell suspension" and waste solution.

by electrical conductivity measurements match the osmolality data very well, which implies EC measurement can be used to monitor the Me_2SO concentration during processing.

The EC data and converted Me_2SO concentrations of "cell suspension" and waste solution are shown in **Figure 8C** and **D**. After about 10 min, the difference between "cell suspension" and waste solution was very small. After 20 min, they were almost identical to each other. The discrepancy between "cell suspension" and waste solution in the beginning was caused by the experiment design and sample procurement method. In the first 2 min, waste solution was cumulated in the dialyzer head part for priming and therefore, the Me_2SO concentration was high. Only after the 3rd minute, waste solution sample could be procured and measured; however, herein, the waste solution sample was actually the mixture of that achieved in the first 3 min. Therefore, it had higher Me_2SO concentration and lower EC than "cell suspension." After a few minutes, the cumulative effect disappeared, and the readings of "cell suspension" and waste solution became identical.

http://dx.doi.org/10.5772/67747

The theoretical prediction of the concentration of Me_2SO in the "cell suspension" is a mixing-dilution problem. The Me_2SO concentration (C_{Me_2SO}) can be estimated by the governing equation:

$$V_{Cell} \cdot \frac{dC_{Me_2SO}}{dt} = -\frac{m}{m+1} \cdot f_{Diluent} \cdot C_{Me_2SO} \tag{10}$$

where V_{Cell} is the volume of "cell suspension" (mL), t is time (min), m is the flux ratio of cell suspension to diluent, and $f_{Diluent}$ is the flow rate of diluent (mL/min).

Solving this equation, the concentration of Me_2SO can be estimated as follows:

$$C_{Me_2SO}(t) = C_{Me_2SO}(t=0) \cdot e^{-\frac{f_{Diluent}}{V_{Cell}} \cdot \frac{m}{m+1} \cdot t} \tag{11}$$

In our experiment, the initial concentration was $C_{Me_2SO}(t=0) = 10\%$, flux of diluent was 20 mL/min, m = 10, and volume of "cell suspension" was 200 mL. So, theoretically, the Me_2SO concentration in "cell suspension" was theoretically predicted as follows:

$$C_{Me_2SO}(t) = 10 \cdot e^{-\frac{20}{200} \cdot \frac{10}{10+1} \cdot t} = 10 \cdot e^{-0.091 \cdot t}(\%) \tag{12}$$

According to the results presented in **Figure 8D**, actually the Me_2SO concentration in "cell suspension" during the whole removal process (45 min) can be fitted as $C_{Me_2SO}(t) = 10e^{-0.07t}$ (R^2 = 0.9741), which was close to but a little different with theoretical prediction. The discrepancy may be caused by the fact that the fluxes of "cell suspension," diluent, and filtration cannot be precisely controlled as programed after longer time running since the engagement between tubing and pumps may get worse due to fatigue of the plastics. This hypothesis can be proved by the fact that in the first 10 min of the experiment (with good engagement and precise flux control), the Me_2SO concentration data of "cell suspension" can be fitted as follows: $C_{Me_2SO}(t) = 10e^{-0.091t}$ (R^2 = 0.9372), which perfectly matches the theoretical prediction.

3.2.2. Me_2SO removal from Me_2SO-5% BSA-0.9% NaCl-water quaternary solution by "dilution-filtration"

The results of Me_2SO removal from the Me_2SO-5%BSA-0.9% NaCl-water quaternary solution by "dilution-filtration" system are shown in **Figure 9**. **Figure 9A** shows the EC and osmolality of the waste solution that was achieved every minute. According to Eq. (4), EC data were converted to Me_2SO concentrations of the waste solution, shown in **Figure 9B**. The Me_2SO concentration decreased to <1% (v/v) after 35 min. The EC data and converted Me_2SO concentrations of "cell suspension" and waste solution are shown in **Figure 9C** and **D**. ECs of "cell suspension" were always lower than those of waste solution due to the existence of

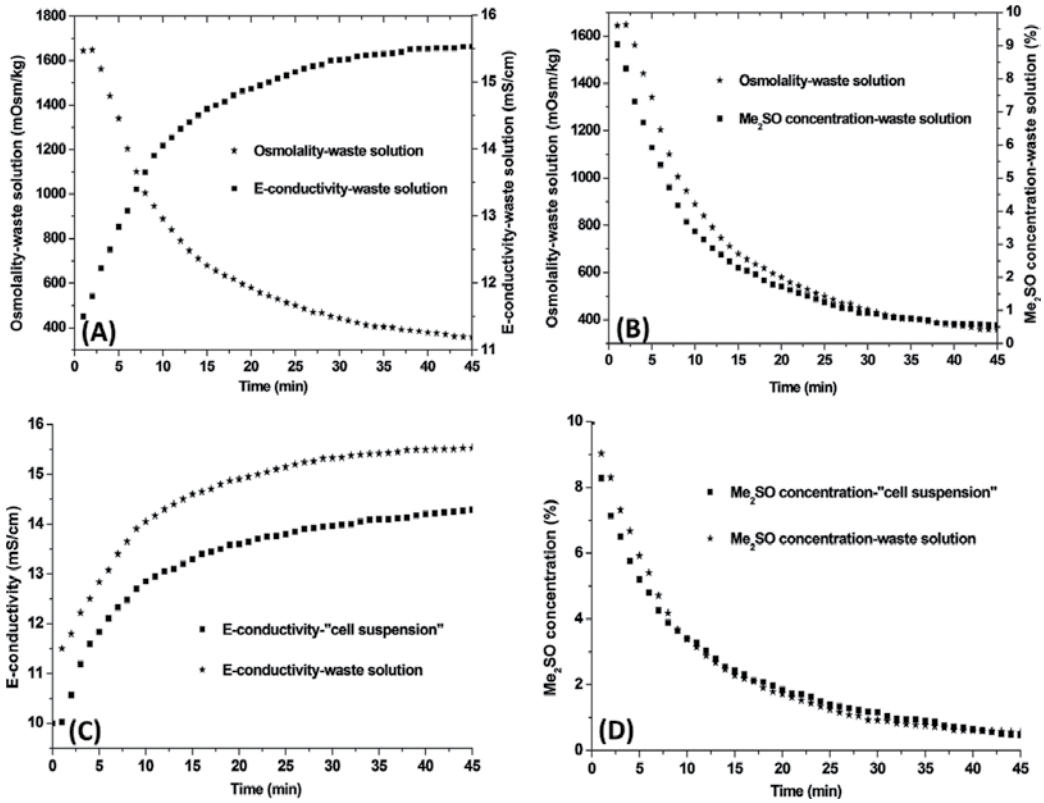

Figure 9. Me_2SO removal from Me_2SO-BSA-NaCl-water quaternary solution by "dilution-filtration." (A) Conductivity and osmolality of waste solution; (B) Me_2SO concentration and osmolality of waste solution; (C) conductivity of "cell suspension" and waste solution; and (D) Me_2SO concentration of "cell suspension" and waste solution.

BSA in "cell suspension." After certain time of processing (~10 min), the difference of Me_2SO concentration between "cell suspension" and waste solution was very small, which implies that measurements of waste solution can be applied to monitor the status of "cell suspension."

4. Discussion

Since the EC of a solution is determined by the solution composition, this fact can be applied to assess the solute concentration. In this chapter, an application of EC measurement in biomedical engineering is presented. In cryopreservation, CPA is needed to eliminate the cryoinjury to cells, which should be added before cooling and removed after thawing. EC measurement of the solution can be used to assess the CPA concentration during CPA addition and removal.

In order to evaluate the CPA concentration (Me_2SO, glycerol, and ethylene glycol), the standard curves of "CPA concentration-EC of the CPA solutions" were obtained experimentally first. For

http://dx.doi.org/10.5772/67747

CPA-NaCl-water ternary solutions, EC can be well represented by exponential equation: $EC = A \cdot \exp(B \cdot C)$. Interestingly, A is determined only by salt concentration, and B is constant for any salt concentrations (B = −0.036, −0.036 and −0.045 for Me_2SO, glycerol and ethylene glycol, respectively. Concentration unit: %, v/v). A similar effect of albumin on the EC of albumin-NaCl-water ternary solutions was also found with an exponential constant of −0.011. This indicates that the effects of CPA, albumin and salt on the EC values are not coupled. This might be due to the fact that CPA, albumin, and salt cannot combine or interact in the solutions.

To demonstrate the application of EC measurement for CPA concentration assessment, a "dilution-filtration" system was successfully applied to remove Me_2SO from solutions efficiently. Compared to the traditional centrifugation method of CPA removal, the "dilution-filtration" can decrease labor and time consumption, eliminate mechanical injury due to centrifugation, avoid cell packing and clumping, and prevent contamination. The volume of diluent solution needed for CPA removal is also decreased dramatically in the "dilution-filtration" method. Compared to the method of dialysis using hollow fibers, the "dilution-filtration" method also has many other advantages: (1) in the beginning of the dialysis process, the cell suspension has to be exposed to diluent in the dialyzer. This process is generally hard to control, and severe osmotic injury can happen. In order to decrease the osmotic shock to cells, sometimes hyperosmotic non-permeable solutions are applied to prime the dialyzer first. This can improve cell recovery but cause complexity, and this non-permeable material eventually needs to be removed. In "dilution-filtration" method, the mixing of cell suspension and diluent can be well controlled in the "dilution" step (adjust the m value). (2) In dialysis method, CPA clearance is due to the passive diffusion transport across the fiber membranes caused by the CPA concentration gradient, while in "dilution-filtration" method, CPA is removed by active filtration. So the CPA removal efficiency can be improved dramatically. (3) In dialysis method, the CPA gradient across the membranes is not uniform along the fibers. So mass transport is not uniform and cells experience different osmotic stresses along the fibers. This increases complexity and thus makes it harder to achieve optimal conditions. (4) It is much easier to control and manipulate the final cell suspension volume and cell concentration with the "dilution-filtration" method.

EC measurement can be a very good method to assess CPA concentration. Compared to direct osmolality measurement by osmometer, its advantages include low cost, ease of operation, real-time and online monitoring, and broad working range (CPA concentration).

For the CPA-salt-water ternary solution, once the salt concentration is fixed, the CPA concentration can be determined by its EC. This is generally the case of CPA removal after cell cryopreservation with fixed salt concentration. The hollow fibers selected in this work can block macromolecules from crossing the fiber membranes, such that the waste solution is CPA-NaCl-water ternary solution. Meanwhile, salt concentrations in cell suspension and diluent are isotonic, and this leads to the fact that salt concentration everywhere, including in waste solution, is isotonic. Accordingly, EC change of the waste solution is determined only by the CPA concentration change. In order to further evaluate the validity of predicting CPA concentration in cell suspension with the data of waste solution, the measurements of "cell suspension" were conducted and compared with those of waste solution. The results show that after a short period

of priming solution removal, the EC, CPA concentration, and osmolality of "cell suspension" and waste solution were almost identical to each other. This proves that assessment of waste solution is a good measure of the real-time state of the cell suspension. Measuring the waste solution, instead of cell suspension, has at least two advantages: First, waste solution is generally simpler than cell suspension without effect of proteins, cell debris, etc. Second, this can prevent direct contact of the EC probe with the cell suspension, keep the cell loop closed, and reduce the risk of contamination. A probe can be mounted in the waste solution loop to achieve real-time, online monitoring of CPA concentration during CPA removal.

5. Conclusion

A simple approach based on electrical conductivity measurements was developed for the quantification and monitoring of the CPA concentration in cryopreservation. Standard data of a few CPAs solutions (Me_2SO, glycerol, ethylene glycol) were obtained. Coupled with the "dilution-filtration" system, this method can be used to measure the EC of waste solution and predict the real situation in cell suspension. This way can help to prevent contamination and achieve on-site and real-time monitoring of the CPA concentration effectively.

Acknowledgements

This work was supported by the Bill & Melinda Gates Foundation (OPP1032522), U.S. National Institutes of Health (NIH) (UM1AI068618), and a Supplement to R33AI094412 funded by National Institute of Allergy and Infectious Diseases (NIAID).

Author details

Zhiquan Shu[1,2]*, Hsiu-Hung Chen[3], Xiaoming Zhou[4] and Dayong Gao[1]

*Address all correspondence to: zqshu@u.washington.edu

1 Department of Mechanical Engineering, University of Washington, Seattle, WA, USA

2 School of Mechanical and Materials Engineering, Washington State University, Everett, WA, USA

3 Department of Mechanical and Aerospace Engineering, University of Missouri, Columbia, MO, USA

4 School of Mechatronics Engineering, University of Electronic Science and Technology, Chengdu, Sichuan, China

http://dx.doi.org/10.5772/67747

References

[1] Polge C, Smith AU, Parkes AS: Revival of spermatozoa after vitrification and dehydration at low temperatures. *Nature* 1949, 164(4172):666.

[2] Okamoto Y, Takaue Y, Saito S, Shimizu T, Suzue T, Abe T, Sato J, Hirao A, Watanabe T, Kawano Y et al: Toxicities associated with cryopreserved and thawed peripheral-blood stem-cell autografts in children with active cancer. *Transfusion* 1993, 33(7):578–581.

[3] Davis JM, Rowley SD, Braine HG, Piantadosi S, Santos GW: Clinical toxicity of cryopreserved bone-marrow graft infusion. *Blood* 1990, 75(3):781–786.

[4] Shu Z, Heimfeld S, Gao D: Hematopoietic SCT with cryopreserved grafts: adverse reactions after transplantation and cryoprotectant removal before infusion. *Bone Marrow Transpl* 2014, 49(4):469–476.

[5] Stroncek DF, Fautsch SK, Lasky LC, Hurd DD, Ramsay NKC, Mccullough J: Adverse reactions in patients transfused with cryopreserved marrow. *Transfusion* 1991, 31(6):521–526.

[6] Gao DY, Liu J, Liu C, Mcgann LE, Watson PF, Kleinhans FW, Mazur P, Critser ES, Critser JK: Prevention of osmotic injury to human spermatozoa during addition and removal of glycerol. *Hum Reprod* 1995, 10(5):1109–1122.

[7] Calmels B, Houze P, Hengesse JC, Ducrot T, Malenfant C, Chabannon C: Preclinical evaluation of an automated closed fluid management device: Cytomate (TM), for washing out DMSO from hematopoietic stem cell grafts after thawing. *Bone Marrow Transpl* 2003, 31(9):823–828.

[8] Rodriguez L, Azqueta C, Azzalin S, Garcia J, Querol S: Washing of cord blood grafts after thawing: high cell recovery using an automated and closed system. *Vox Sang* 2004, 87 (3):165–172.

[9] Perotti CG, Del Fante C, Viarengo G, Papa P, Rocchi L: A new automated cell washer device for thawed cord blood units. *Transfusion* 2004, 44(6):900–906.

[10] Chen HH, Zhou XM, Shu ZQ, Woods EJ, Gao D: Electrical conductivity measurements for the ternary systems of glycerol/sodium chloride/water and ethylene glycol/sodium chloride/water and their applications in cryopreservation. *Biopreserv Biobank* 2009, 7 (1):13–17.

[11] Shu Z, Fang C, Zhou X, Gao D: Cryoprotective agent (CPA) removal with dilution-filtration method and CPA concentration monitoring with electrical conductivity measurements. In: *ASME 2014 International Mechanical Engineering Congress and Exposition: November 14–20, 2014; Montreal, Quebec, Canada*. ASME 2014.

[12] Valeri CR, Ragno G, Pivacek L, O'Neill EM: In vivo survival of apheresis RBCs, frozen with 40-percent (wt/vol) glycerol, deglycerolized in the ACP 215, and stored at 4 degrees C in AS-3 for up to 21 days. *Transfusion* 2001, 41(7):928–932.

[13] Valeri CR: Simplification of methods for adding and removing glycerol during freeze-preservation of human red blood-cells with high or low glycerol methods — biochemical modification prior to freezing. *Transfusion* 1975, 15(3):195–218.

[14] Rowe AW, Eyster E, Kellner A: Liquid nitrogen preservation of red blood cells for transfusion — a low glycerol-rapid freeze procedure. *Cryobiology* 1968, 5(2):119–&.

[15] Meryman HT, Hornblower M: Simplified procedure for deglycerolizing red blood-cells frozen in a high glycerol concentration. *Transfusion* 1977, 17(5):438–442.

[16] Meryman HT, Hornblower M: Method for freezing and washing red blood-cells using a high glycerol concentration. *Transfusion* 1972, 12(3):145.

[17] Ding WP, Zhou XM, Heimfeld S, Reems JA, Gao DY: A steady-state mass transfer model of removing CPAs from cryopreserved blood with hollow fiber modules. *J Biomech Eng-T* Asme 2010, 132(1):011002.

[18] Ding WP, Yu JP, Woods E, Heimfeld S, Gao DY: Simulation of removing permeable cryoprotective agents from cryopreserved blood with hollow fiber modules. *J Membr*ane *Sci* 2007, 288(1–2):85–93.

[19] Castino F, Wickramasinghe SR: Washing frozen red blood cell concentrates using hollow fibres. *J Membr*ane *Sci* 1996, 110(2):169–180.

[20] Arnaud F, Kapnik E, Meryman HT: Use of hollow fiber membrane filtration for the removal of DMSO from platelet concentrates. *Platelets* 2003, 14(3):131–137.

[21] Mata C, Longmire EK, McKenna DH, Glass KK, Hubel A: Experimental study of diffusion-based extraction from a cell suspension. *Microfluid Nanofluid* 2008, 5(4):529–540.

[22] Glass KKF, Longmire EK, Hubel A: Optimization of a microfluidic device for diffusion-based extraction of DMSO from a cell suspension. *Int J Heat Mass Transfer* 2008, 51(23–24): 5749–5757.

[23] Zhou XM, Liu Z, Shu ZQ, Ding WP, Du PA, Chung J, Liu C, Heimfeld S, Gao DY: A dilution-filtration system for removing cryoprotective agents. *J Biomech Eng-T Asme* 2011, 133(2):021007.

[24] Shu Z: Development of optimal biopreservation methods and technology for cellular therapy and clinical diagnosis [Thesis]. Seattle, WA, USA: University of Washington; 2013.

Edited by Adel El Shahat

Motivated by the importance of electrical resistivity and conductivity, important experts in this field grasp most recent researches in this book. It addresses recent advances in electrical resistivity and conductivity modelling, measurement, estimation and sensing methods and implications. This book introduces innovative case studies for "Electrical Resistivity Sensing Methods and Implications", "Resistivity Model of Frozen Soil and High-Density Resistivity Method for Exploration of Discontinuous Permafrost", "Measurement of Electrical Resistivity for Unconventional Structures", "Estimation of Hydrological Parameters from Geoelectric Measurements" and "Assessment of Cryoprotectant Concentration by Electrical Conductivity Measurement and Its Applications in Cryopreservation". These recent advances are well prepared and presented in six chapters. These chapters are carefully selected to reflect current variable techniques, new concepts and methods related to the book's topic from different perspectives.

ISBN 978-953-51-4815-9

IntechOpen